UNIVERSITÀ DEGLI STUDI DI PADOVA

DIPARTIMENTO DI FISICA E ASTRONOMIA "G. GALILEI"

CORSO DI LAUREA IN ASTRONOMIA

TESI DI LAUREA MAGISTRALE

STUDY OF RECURRING SLOPE LINEAE ON THE MARTIAN SURFACE

Relatore: Prof.ssa MONICA LAZZARIN
Co-relatori: Dr. GABRIELE CREMONESE
Dr. MAURIZIO PAJOLA

Laureando: GIOVANNI MUNARETTO
Matricola: 1155202

ANNO ACCADEMICO 2017/2018

Contents

Abstract

Recurring Slope Lineae (RSL) are a candidate source of liquid water possibly located on the shallow subsurface of Mars. Their study is important as these features, if really due to water, would have important implications for potential biologic processes, for resources on the Martian surface, for the climatic history of Mars, for its future human exploration and habitability and for the Planetary Protection issue, which currently forbids surface mission to land on RSL-bearing sites. Moreover, they are a poorly understood phenomenon over which the scientific community is currently debating and for which accurate modelling and interpretation do not exist yet.

In this thesis we will perform a statistical analysis of RSL on the Martian surface, which outlines as follows: in the first chapter we will review the relevant background and literature concerning the planet Mars and in the second chapter we will introduce Recurring Slope Lineae. In the third chapter we will perform a global survey and statistical study of all candidate and confirmed RSL sites discovered so far, which is the most updated and complete at the time of writing; in addition, we will conduct a detailed study of RSL present in Raga crater. In the fourth chapter we will present and discuss the results of the analysis of the third chapter. In the fifth chapter we will draw our conclusions and finally, in the sixth chapter we will discuss RSL as a science case to be studied with the Colour and Stereo Surface Imaging System (CASSIS) camera on board the ESA ExoMars Trace Gas Orbiter (TGO) mission, which will provide useful and unique information on their nature.

The aim of this thesis is to characterise all candidate and confirmed RSL through a statistical analysis of properties of the surface in which they form, thus providing a more extensive and complete global description of these features than what is present in literature. In addition we study the dependence of their length on time, slope and terrain orientation, extending and confirming studies performed by other authors.

Sommario

Le Recurring Slope Lineae (RSL) sono candidate sorgenti di acqua liquida probabilmente collocate in prossimità della superficie di Marte. Lo studio delle RSL è importante poiché, se queste fossero legate ad acqua liquida, avrebbero importanti implicazioni per quanto concerne la presenza di potenziali processi biologici, l'utilizzo in-situ delle risorse sulla superficie Marziana, la storia climatica di Marte, la sua esplorazione umana e la questione della Protezione Planetaria, che attualmente impedisce l'atterraggio di missioni spaziali in prossimitdì siti contenenti RSL.

Inoltre le RSL sono un fenomeno ancora poco compreso, correntemente oggetto di studio da parte della comunità scientifica, per il quale non esiste ancora un'interpretazione soddisfacente.

In questa tesi viene effettuato uno studio statistico delle RSL sulla superficie di Marte che si dettaglia come di seguito: nel primo capitolo viene presentata una descrizione generale del pianeta Marte, mentre nel secondo capitolo vengono introdotte le Recurring Slope Lineae. Nel terzo capitolo viene effettuata un'analisi statistica, più completa e aggiornata di quanto presente in letteratura, di tutti i siti candidati e confermati di RSL. Inoltre, verrà effettuato uno studio dettagliato delle RSL collocate nel cratere Raga. Nel quarto capitolo verranno presentati e discussi i risultati del terzo capitolo. Nel quinto capitolo verranno presentate le conclusioni di questo studio. Infine, nel sesto capitolo verranno discusse le RSL come tema scientifico da studiare con la stereo camera CaSSIS, a bordo della missione ESA ExoMars/Trace Gas Orbiter, la quale potrà fornire informazioni fondamentali sulla natura delle RSL.

Lo scopo di questa tesi è caratterizzare tutte le RSL candidate e confermate attraverso un'analisi statistica delle proprietà della superficie dove esse si formano, al fine di darne una descrizione più approfondita e completa di quanto presente in letteratura. Oltre a ciò, viene eseguito uno studio di alcune proprietà fondamentali delle RSL, quali la dipendenza della loro lunghezza dal tempo, dalla stagione, dalla pendenza del terreno e dalla sua orientazione che conferma ed estende quanto presente in letteratura.

Chapter 1

Introduction

In this chapter we will give a brief overview of the most relevant aspects of the planet Mars and discuss evidences of past and present water on the Martian surface and subsurface. The aim of this chapter is to provide a background to frame the topic of this thesis, the so called Recurring Slope Lineae (RSL), which will be discussed in the next chapter.

1.1 The planet Mars

Mars is the fourth planet from the Sun in the Solar System. It is the second smallest planet, after Mercury, having a mass of ≈ 0.1 $M_\oplus$ (Earth Masses, 1 $M_\oplus = 5.97 \cdot 10^{27}$ g) and a radius of ≈ 0.53 $R_\oplus$ (Earth Radius, 1 $R_\oplus = 6.3781 \cdot 10^6$ m), resulting in a gravity acceleration of 3.7 m/s^2, about the 38% of that of the Earth. Mars' rotation period is slightly longer than the Earth's one, resulting in a slightly longer solar day (or *sol*) of 24 hours, 39 minutes and 35.244 seconds. Its orbit has a semi-major axis of approximately 1.52 AU and an eccentricity of 0.09, resulting in a Martian sidereal year of about 686.98 Earth solar days, or 668.5991 sols. Mars orbits approximately 1.52 times as far from the Sun as Earth, hence it receives approximately the 43% of sunlight.Since it has an axial tilt of 25.19°, Mars experiences seasons, which are affected by its relatively large eccentricity.Seasons are indicated with the *Solar Longitude* angle, L_s, which is 0° at the vernal equinox, 90° at summer solstice, 180° at the autumn equinox, and 270° at winter solstice (Clancy et al.,2000).

	Mars	Earth
Radius (m)	3.391 10^6	6.3871 10^6
Mass (g)	6.39 10^{26}	5.97 10^{27}
Gravity (m/s^2)	3.7	9.81
Mean pressure (mbar)	7.3	1013
Mean temperature (K)	210	287
Distance (AU)	1.52	1.0
Revolution period (solar days)	686.98	365.2422
Rotation period (solar days)	1.03	0.99

Table 1.1: Summary of most relevant parameters of the planet Mars, compared to those of the Earth.

Internal structure and topography

The internal structure of Mars is differentiated into a dense metallic core, with an estimated radius of approximately 1794 km and composed primarily of iron and nickel (Rivoldini et al.,2011), surrounded by a silicate mantle. The Martian crust has a basaltic composition of mainly silicon, oxygen and metals such as iron, magnesium, aluminium, calcium and potassium and has an average thickness of 50 km (Wieczorek and Zuber,2004). The crust has a relatively large variation in surface elevation of 29429 m (Carr,2007), as we can see in figure (1.1); the lowest point is located on the floor of the *Hellas* basin, at -8200 m and the highest point is at the summit of *Olympus Mons* at 21229 m (the reference for elevations is the locus of points at which atmospheric pressure is 6.1 mbar Carr, 2007). The most important topographic feature is the so-called *global dichotomy*: the northern hemisphere is dominated by low elevations terrains, while the southern hemisphere is characterized by by high elevation ones. The relative elevation between the two hemispheres ranges from 3 to 6 km. This dichotomy is also evident when considering crater densities, with the southern highlands being heavily cratered and the northern lowlands showing a more smooth topography with few large craters and evident signs of more recent resurfacing. In addition, the *global dichotomy* is expressed in terms of crustal thickness, which reaches a maximum of 58 km in the southern highlands, and a minimum of 32 km in the northern lowlands (Neumann et al.,2004). Other important topographic features are the *Tharsis* bulge, a relatively large volcanic plateau of approximately 5000 km in diameter and 10 km in elevation, which covers up to the 25% of the planets surface. The *Tharsis* bulge contains the largest known volcanoes on the Solar System, namely the *Asia Mons*, *Pavonis Mons* and *Ascreaeus Mons*, collectively called *Tharsis Montes*. Instead At the western edge of the plateau, it is located the tallest volcano on the planet, the *Oympus Mons*. A much smaller bulge is located West of the *Tharsis* region and it is called the *Elysium* volcanic complex. Important negative topographic features are the *Hellas* basin, a depression of approximately 9 km located at (47°S,67°E), and the *Argyre* basin, a $1-2$ km depression located at (50°S,318°E). All these features are depicted in figure (1.1).

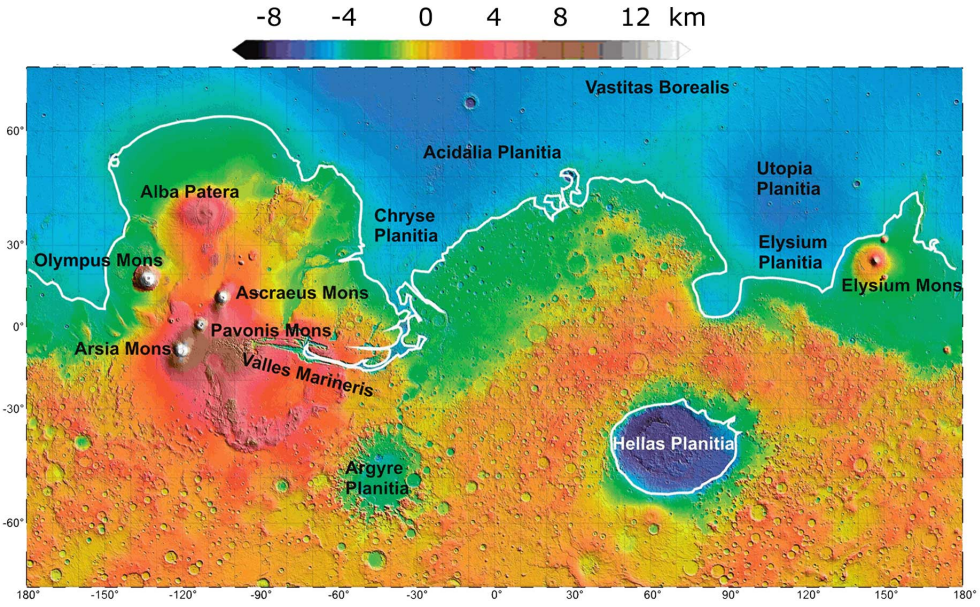

Figure 1.1: The global dichotomy is evident in this colourized elevation map: the northern hemisphere is dominated by smooth lowlands (blue) while the souther hemisphere is dominated by heavily cratered highlands (orange).

Surface features

The Martian surface is characterized by a distinctive reddish colour, due to a fine iron oxide dust cover (Christensen et al.,2003), on which dark and bright areas are present. The latter are in correspondence of polar caps, clouds and the *Hellas*, *Tharsis* and *Arabia Terra* regions, where massive volcanoes lie. Dark areas, instead, represent regions where winds swept dust on the surface, leaving the dark, rocky bedrock exposed. The North an South poles are covered by two $1-3$ km thick polar caps made of water ice, covered by a variable layer of CO_2 ice. Their estimated volume is of approximately one million of km^3 each.

Atmosphere

The atmosphere of Mars is very thin, and composed primarily of CO_2 and small quantities of Nitrogen. Water vapour is present, even though in traces.
During southern spring and summer, when temperatures are at their maximum values, dust storm tend to occur at low latitudes. These dust storms may be local or grow to global scales encircling the whole planet for several weeks. During dust storms the optical depth can rise from 0.5 up to 5, obscuring the surface. One of the effects of dust storms is a net transfer of dust from the southern hemisphere to the low northern latitudes. However, the amount of dust lifted by storms is small, and is equivalent to a few micrometers spread over the whole planet.

Surface temperatures

The very thin and dry Martian atmosphere absorb little of the radiation emitted by the Sun and Mars itself. As a consequence, surface temperatures are mostly given by the balance between the solar radiation absorbed by the surface, the emitted radiation in the infrared and the net energy flux conducted by the ground. Mean diurnal temperatures range from 150 K at the poles to 240K in the warmest regions of the southern hemisphere (Kieffer et al.,1977) and peak temperatures can reach up to 300K during summer in the southern latitudes.

1.2 Water on Mars

The presence and stability of liquid water on Mars is a very important topic because its implications on potential biologic processes and human exploration. There are compelling evidences of the presence of liquid water in the past geologic history of Mars. On the contrary, even though its presence has been recently detected on the subsurface (Orosei et al.,2018), its detection on the surface is still an open question. In this section we will discuss the stability of liquid water on the Martian surface and describe all evidences and hypotheses about its presence in both past and present Martian conditions.

1.2.1 Stability of water on Mars

Liquid water is stable only for temperatures above 273K and partial pressures above 6.1 mbar, and would otherwise boil or directly sublimate. These conditions are very unlikely on the surface, as the pressure exerted by the atmosphere is less than 6.1 mbar for most of the planet, and temperatures rise over 273K only during southern summer for a limited time of the day. In low elevation areas, where pressure is higher, and in correspondence of low permeability and ice rich soils, water could transiently form when temperatures rise over 273 K. Moreover, if the soil has enough salts, these could lower the freezing point of ice which would melt to form the so called liquid *brines* (i.e. salty water). However, these conditions would occur only near noon and in the uppermost centimetres of the soil.

1.2.2 Evidences of past liquid water

Although liquid water can exist only transiently on the surface in present Martian conditions, there are evidences that the planet may have been much wetter and warmer in the ancient past (Pollack et al.,1987) and water may have flown across its surface. Evidences of past water come from observations of classical geomorphic features attributed to water, like lakes, river valleys and deltas, from the detection of its alteration on minerals composing the basaltic Martian surface and from the analysis of Martian meteorites.

Geomorphic evidences of water

Analysis of images of the Martian surface showed the extensive presence of dendritic *valley* networks, like the one depicted in figure (1.2B), which were formed by the eroding action of a sustained flow of liquid water. Imaging and altimetry of these features showed that they are common on most of the oldest Martian surface and indicate that precipitation, surface runoff (i.e flooding) and seepage of groundwater occurred as well, at least episodically, in the early Martian history (Carr,2007).

Many depressions are observed to have *inlet* and *outlet* valleys. Moreover, when *inlet* valleys enter the depression, deltas and alluvial fans are commonly observed. These geomorphic features are characteristic of terrestrial lakes and have been interpreted as the presence of *paleolakes* in the Martian past history. An example is given in figure (1.2 A).

Other signs of past flowing water are *outflow channels*, which appear as large, long, isolated channels lacking a dendritic network of branches which characterizes the *valleys* discussed above. An example is depicted in figure (1.2C). Most of *outflow channels* are thought to be formed by the rapid release of large volumes of water.

Other features are *inverted reliefs*, occurring in correspondence of river beds. When sediments are deposited on the floor of a river they undergo cementation and become relatively resistant to erosion. If later the area is buried, erosion removes the less resistant covering layers until the inner, cemented layer of sediments is exposed. The latter is resistant to erosion and will show the "*negative*" of the river bed. An example is shown in figure (1.2 D).

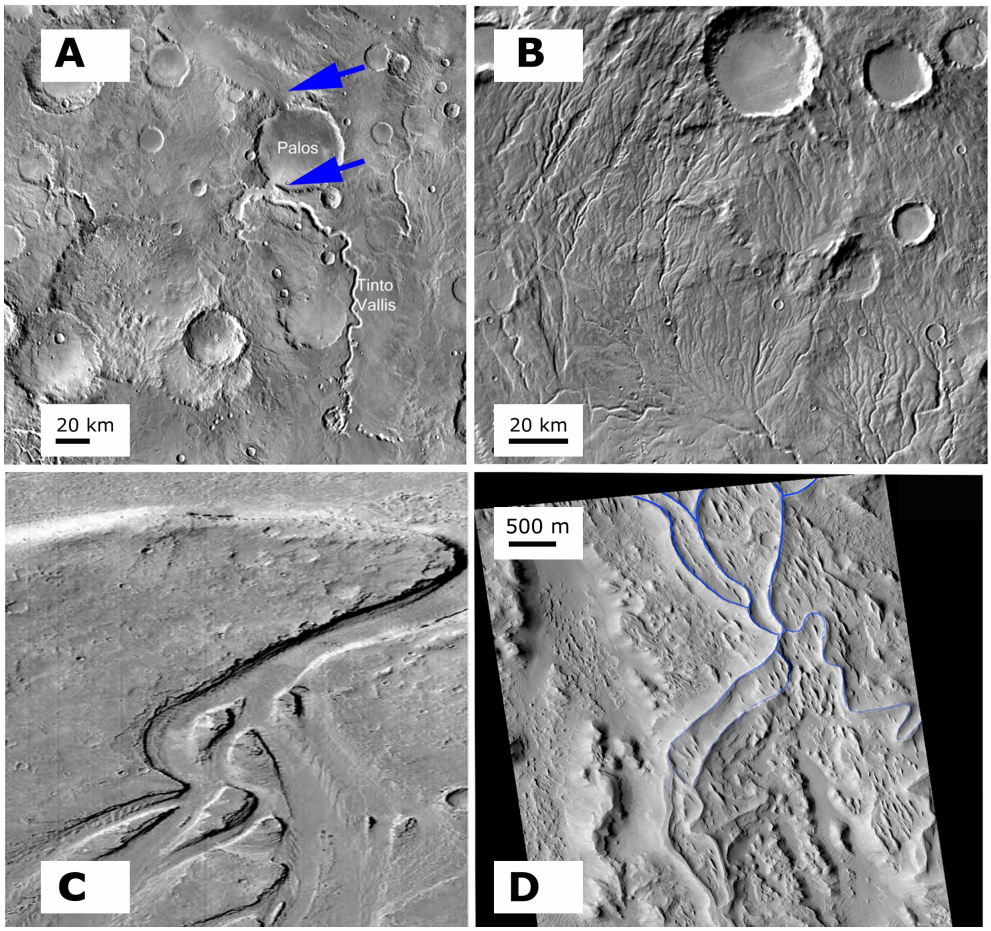

Figure 1.2: Geomorphic evidences of water; A) blue arrows indicate the *inlet* and *outlet* valleys which breach the crater rim, suggesting that water flew into the crater from Tinto Vallis in the bottom part of the figure and flew out from the breach in the crater in the top of the figure. Adapted from Carr (2007). B) A dense drainage network, adapted from Carr (2007). C) Example of an *outflow channel*. D) Example of a *inverted relief*, indicated in blue.

Evidences from alterations of surface minerals

The Martian surface is predominantly basaltic and mostly composed of igneous minerals, like olivine, pyroxene and plagioclase feldspar, which react with water to form hydrated minerals like goethite, evaporites, phyllosilicates. The detection of all these hydrated minerals is an evidence of the presence and activity of past liquid water on the Martian surface.

Another kind of alteration is due to the upward migration of subsurface hydrothermal fluids, heated by the residual heat produced by large impacts (Abramov and Kring,2005). In particular, when water migrates through the basaltic lithosphere, its interaction results in the formation of a particular rock called *serpentinite*, which has been observed on Mars (Ehlmann et al.,2010).

Evidence from meteorites

Evidence of the presence of water in the past Martian history comes also from the chemical analysis of Martian meteorites, which shows the alteration of olivine by water (Treiman,2005).

1.2.3 Contemporary water

As anticipated, the low average temperature and pressure of the Martian surface prevent the formation of stable liquid water, which can form only in transient anomalous conditions. On the contrary, stable liquid water has been detected below the surface using the MARSIS (Mars Advanced Radar for Subsurface and Ionosphere sounding) instrument by Orosei et al. (2018) in a 1.5 km deep, 20 km wide subglacial lake located in the region of *Planum Australe* (193°E, 81°S).

Additionally, frozen water exists in the polar caps and is abundant and widespread below the uppermost meters of Martian soil, as indicated by detection of hydrogen with the Mars Odyssey Gamma Ray Spectrometer and Neutron Spectrometer (Boynton et al.,2002;Boynton et al.2007;Wilson et al.,2018). These observation revealed that buried water ice is highly abundant poleward of $\pm 50^\circ$ but it also is present, though in lower concentrations, in several low latitude locations, like the slopes of *Tharsis Montes*, *Elysium Mons* and at the *Medusae Fossae* formation (Feldman et al., 2004,Wilson et al.,2018). Moreover, $>$ 100 m thick exposed water ice sheets have been imaged poleward of $\pm 50^\circ$ by Dundas et al. (2018).

Chapter 2

Recurring Slope Lineae

Recurring Slope Lineae (RSL) are narrow (0.25-5 m) dark markings found on warm ($T \geq 250K$) steep ($\geq 28°$) slopes with exposed bedrock outcrops. They were first discovered by McEwen et al. (2011) using the High Resolution Imaging Science Experiment (HiRISE) camera on board the Mars Reconnaissance Orbiter (MRO) mission (McEwen et al., 2007). Since then, they have been found only in five geographic regions of the Martian surface and named accordingly: across a southern mid-latitudes band from 30° S to 60° S (SML RSL), in the equatorial highlands (EQ RSL), in Chryse and Acidalia Planitiae in the northern hemisphere (CAP RSL) and finally in Valles Marineris (VM RSL), where they are mostly concentrated (McEwen et al., 2011; McEwen et al., 2013b; Stillman et al., 2014; Ojha et al., 2014; Chojnacki et al., 2016; Stillman et al., 2016; Stillman et al., 2017a). Their geographical distribution is depicted in figure (2.1). The most intriguing aspect of RSL is their activity, which starts with the appearance of dark streaks departing from bedrock outcrops when surface temperature rises above 250 - 270 K, in local early spring or late summer, and continues with a phase of incremental lengthening where the lineae elongate following the topographic gradient. Once they reach the maximum extent, they remain dark for a prolonged period of time and eventually fade in cold seasons, as temperatures drop below 250 - 270 K. This sequence repeats every year in the same locations. An example of RSL is given in figure (2.2).

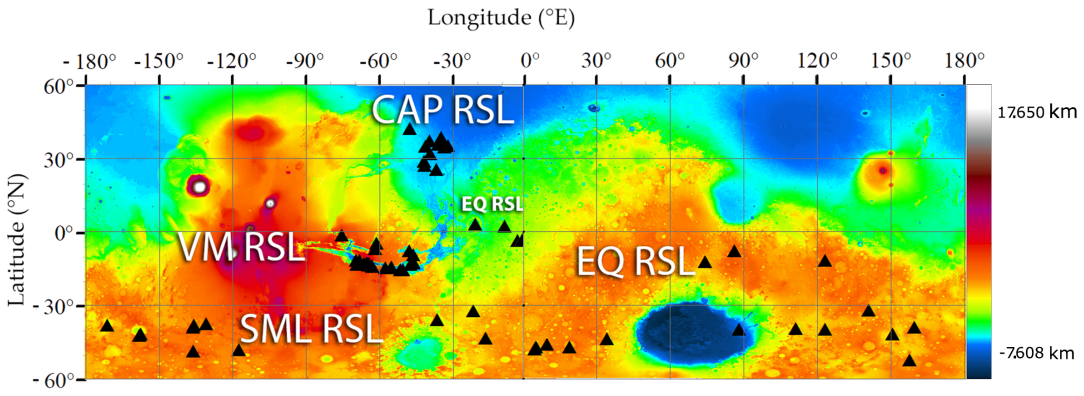

Figure 2.1: Geographical distribution of confirmed RSL overlaid on the Mars Orbiter Laser Altimeter (MOLA) colorized elevation map. SML RSL are defined as those located southern than $-30°$N, CAP RSL are those inside the Chryse and Acidalia Planitiae, in the northern hemisphere. VM RSL are located in Valles Marineris and EQ RSL are those on the equatorial highlands, from $\approx -30°$ N to $\approx 30°$ N.

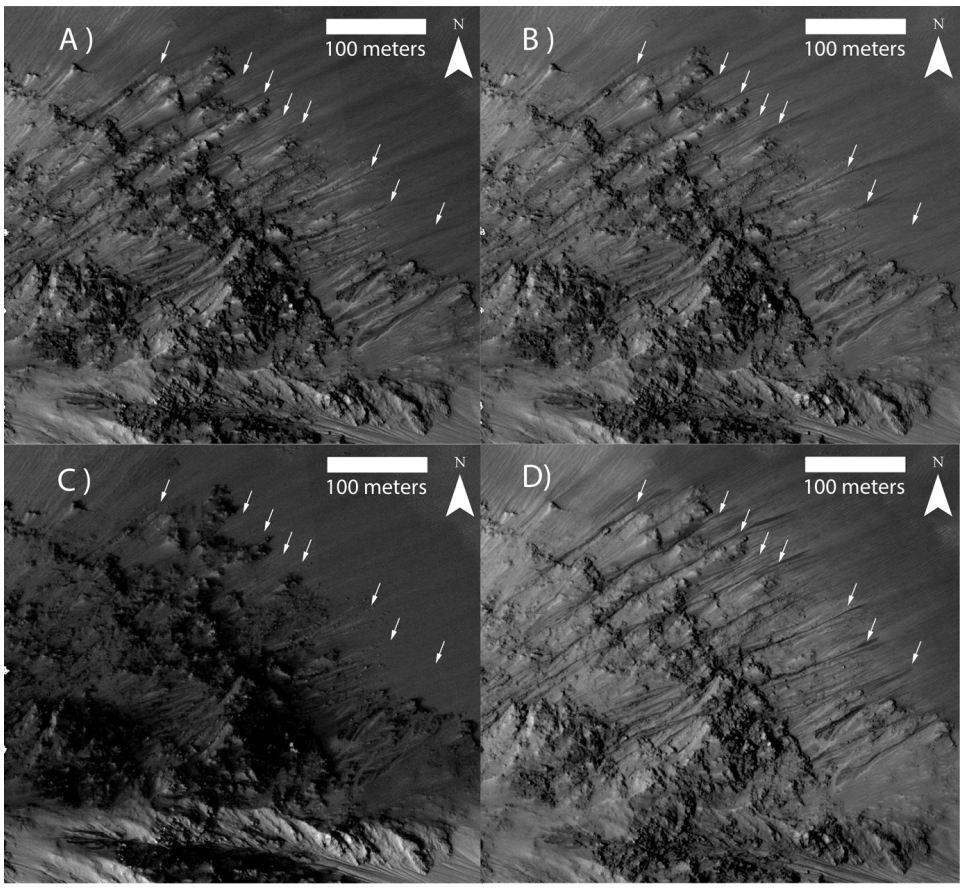

Figure 2.2: Example of RSL, indicated by white arrows, on the slopes of Juventae Chasma (-4.691 °N, 298.577 °E). This temporal sequence (from A to D) of images highlights their incremental lengthening, fading and recurrence. In panel A), obtained from HiRISE image ESP_032074_1755, RSL appear as dark markings. In panel B), obtained from HiRISE image ESP_032219_1755, the same RSL appear longer except one which faded (this behavior is peculiar of VM RSL). In panel C), obtained from HiRISE image ESP_039195_1755, RSL are absent while in panel D), obtained from HiRISE image ESP_041318_1755 they re-appear on the same locations of panel A).

2.1 Observations

RSL sites have been mainly studied with four instruments: the HiRISE camera on board the MRO mission, which provides images at a spatial scale up to 0.25 cm/px in the near infrared, red and blue part of the electromagnetic spectrum; the Compact Reconnaissance Imaging Spectrometer (CRISM, Murchie et al., 2007) on board the MRO mission, which provides spectral cubes with 544 channels from 0.4 μm to 3.92 μm at a spatial scale of 18 m/px; the Thermal Emission Imaging system (THEMIS, Christensen et al., 2004) on board the Mars Odyssey mission, which observes in the visible wavelengths from 0.42 μm to 0.86 μm at a resolution of 18 m/px and in the infrared wavelengths from 6.8 μm to 14.9 μm with 9 spectral bands at a resolution of 100 m/px; finally the Thermal Emission Spectrometer (TES, Christensen et al., 2001), on board the Mars Global Surveyor mission (MGS), which observes in the infrared wavelengths from 5.5 μm to 100 μm and in the visible/near infrared wavelengths from 0.3 μm to 2.9 μm at a spatial resolution of 3 km/px. THEMIS and TES are particularly useful to derive surface temperatures. In the following paragraphs we will review the most important results obtained with these instruments.

HiRISE observations

Due to their small spatial scale (< 5 m), the only instrument with enough spatial resolution to sample RSL at the Nyquist level is the HiRISE camera, which can resolve objects down to ≈ 80 cm in size. Repeated observation with this instrument allowed to detect 93 confirmed RSL sites and 462 candidates, for which further observations and investigation are necessary. Analyzing HiRISE images and digital terrain models (DTM), different studies suggested that most RSL are relatively more numerous on the most illuminated slopes (McEwen et al., 2013b; Stillman et al., 2014; Ojha et al., 2014; Chojnacki et al., 2016; Stillman et al., 2016; Stillman et al., 2017a; Stillman and Grimm, 2018). According to these studies, SML RSL activity starts in southern spring and occurs mainly on North, North-West and West facing slopes for SML RSL, which are the most illuminated and receive the most downward infrared flux from the afternoon atmosphere; this behavior is shared also for VM and EQ RSL, which are located near the equator, but here RSL activity occurs mainly on South facing slopes during southern spring and summer and then steps to North facing slopes during the northern summer, matching the seasonality of the most illuminated, and in turn most heated, slopes. On the contrary, CAP RSL are more problematic, as they appear preferentially appear on South-West and West facing slopes but they do not form on South facing slopes, which are the most illuminated. However, it must be noted that to date, only 8 confirmed CAP RSL have been identified, therefore a wide statistics is still far to be accomplished. The picture is, however, more complicate as not all RSL follows these trends, like those in Juventae Chasma (McEwen et al., 2013b; Chojnacki et al., 2016; Stillman et al., 2017a). Moreover, RSL located in different geographic regions exhibit different unique features: high cadence HiRISE imaging shows that SML RSL have two pulses of activity during their active season and

completely fade between them, even though the insolation is at his maximum (Stillman and Grimm, 2018). VM RSL activity is peculiar since RSL both fade and lengthen at the same time in the same slope orientations; moreover, RSL are longer and active for a slightly longer period of time with respect to SML RSL (Stillman et al., 2017). CAP RSL do not show any of the above mentioned peculiarities, but are active for a longer period of time (Stillman et al., 2016).

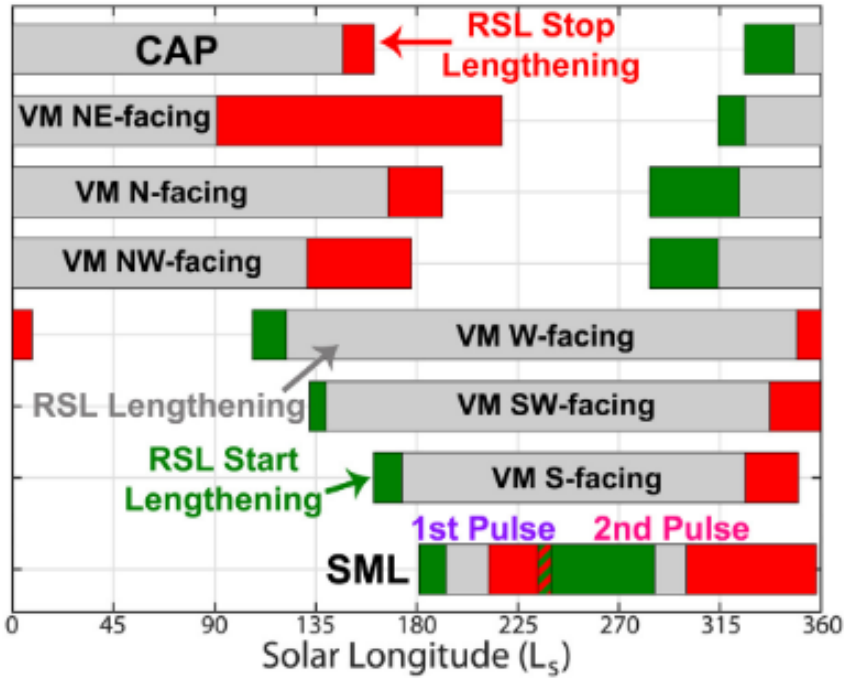

Figure 2.3: RSL activity as a function of the solar longitude from Stillman and Grimm (2018). The solar longitude L_s is the angle between Mars and the Sun, measured from the Northern hemisphere spring equinox where $L_s = 0$.

CRISM observations

In principle, CRISM spectra can be useful to understand the composition of the Martian surface characterised by the occurrence of RSL. Both liquid water and hydrated salts have absorption bands at $\approx$ 1.4 μm, $\approx$ 1.9 μm and $\approx$ 3.0 μm, within the spectral range of CRISM. Laboratory experiments on the dehydration of soils shows that these spectral features quickly disappear, the $\approx$ 1.4 μm in particular, as the soil dehydrates, while the darker albedo is retained for longer (Massé et al., 2014) because minimal quantities of water are necessary to darken the regolith. This makes the *spectral* detection of liquid water very challenging, because it must be observed as soon as it wets the soil, while they are more easily identified by imaging, since they are dark even when their spectral firm is not detectable. To complicate the matter, RSL have a smaller spatial scale than a CRISM pixel (0.25 cm - 5 m against 18 m) and thus they are not resolved. For best sites, where there are several lineae on the same slope, the RSL can fill up to almost one CRISM pixel (Ojha et al., 2015). The analysis of CRISM spectra conducted on 4 sites by Ojha et al. (2015) showed absorption features at $\approx$ 1.48 μm, $\approx$ 1.9 μm

and ≈ 3.0 μm correlated with RSL-dense pixels, while only the ≈ 1.9 μm and ≈ 3.0 μm absorptions were detected on RSL-free pixels. An example of such spectra is shown in figure (2.4). Since these detection are only from images with wide RSL, they have been attributed to their areally extensive presence. This suggested that RSL-dense pixels are more hydrated than RSL-free pixels, hence meaning that either hydrated material is transported by RSL or RSL hydrates the soil themselves. These hydration features, however, are too narrow to be attributed to surficial liquid water but they are consistent with a mixture of Martian soil and hydrated salts, namely Magnesium perchlorate, Magnesium chlorate and Sodium perchlorate. This detection is of critical importance because it suggests the contemporary presence of water and hydration of salts on the surface of Mars (Ojha et al., 2015).

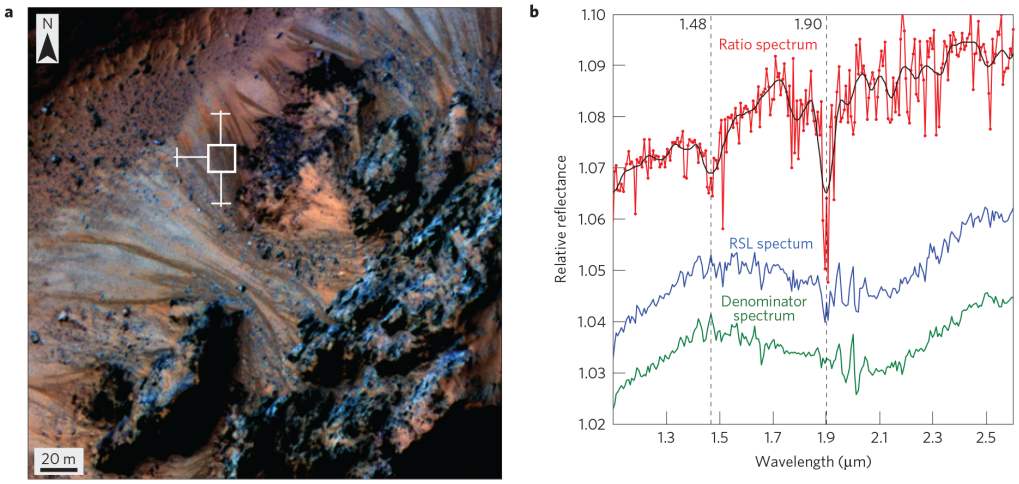

Figure 2.4: Figure (3) of Ojha et al. (2015); *a*) RSL on the central peak of Hale crater, from HiRISE image ESP_032416_1440 (IRB channel). The white box represents the location of CRISM pixels, with errors. *b*) IR spectrum of the RSL inside the CRISM pixel of panel a) (blue), spectrum of a RSL-free region (green) and their ratio (red). Absorptions at 1.48 and 1.90 μm are evident.

THEMIS and TES

The THEMIS and TES instruments are particularly useful to study the RSL because they provide the IR observations. Despite their pixel scale of 100 m/px and 3km/px prevents the study of single lineae, they have been used to assess their thermal behavior and their water content.

Thermal behavior

A thermal analysis of RSL-bearing slopes can be performed using THEMIS and TES data, but it must be noted that the contribution of all slopes inside each pixel are averaged, and thus the real surface temperature can be higher or lower than what is estimated, depending on the slope azimuth. Another caveat is that since THEMIS observes from 2:00 to 4:00 PM, NW-facing slopes will have a near-peak temperature while other slopes already reached their peak temperature earlier in the day and will thus exhibit a systematically lower temperature. Instead, TES observations are conducted from 1:00-2:00 PM and are more indicative of the peak temperatures, although averaged over 3 km. Moreover, THEMIS and TES observations are not synchronized with HiRISE ones, so the surface temperature of RSL-bearing slopes observed with HiRISE must be interpolated from THEMIS measurements. Considering this caveats, thermal analysis of RSL-bearing slopes showed that RSL lengthen only when mid-afternoon surface temperatures rises over 250-270 K, and they stop and fade when surface temperatures drop below these limits. (McEwen et al.,2013b; Stillman et al.,2014; Ojha et al.,2014). The temperature dependence for SML RSL is depicted from figure (2.5).

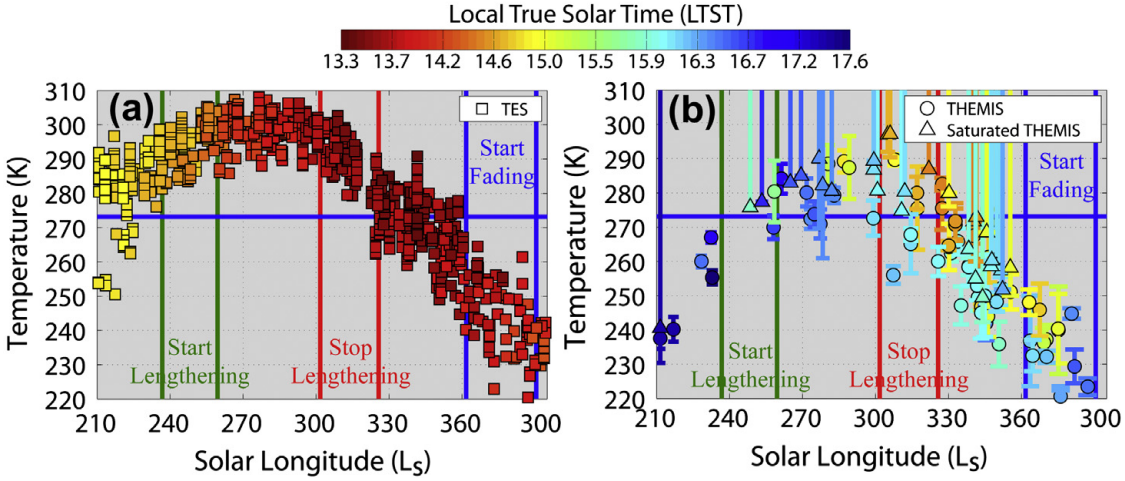

Figure 2.5: Temperature dependence for SML RSL, obtained from Figure (3) of Stillman et al. (2014), as a function of season (L_s) and Local True Solar Time (LTST). The blue horizontal line represents the melting point of pure water at $T = 273$ K. All RSL start lengthening above 273K and stop lengthening and eventually fade below this value.

Water content

THEMIS data have been used by Edwards and Piqueux (2016), in conjunction with a thermal model and a wet regolith model, to assess the water content of RSL. Water, filling the space between grains in the regolith, creates a continuous medium in which the heat can flow, increasing the regolith's thermal conductivity and inertia and, ultimately, affecting the temperature. With a thermal model it is possible to link the observed surface temperature to the regolith thermal inertia and then, with a wet regolith model, the associated water content can be inferred. Estimates conducted at Garni crater revealed that RSL are probably dry, having a water content consistent with that of slopes without RSL. However, it must be noted that this method is insensitive to water contained in hydrated salts, as that detected by Ojha et al. (2015). However, other authors showed how these results were obtained using THEMIS pixels without a significant coverage of RSL (Stillman et al.,2017a), thus criticizing the conclusions that RSL-bearing slopes have the same water content of RSL-free slopes.

2.2 Formation mechanisms

The observational facts outlined in the previous sections allow us to define RSL as features which exhibit the following traits:

- Darker albedo with respect to their surroundings;
- Annual recurrence in the same places;
- Incremental lengthening followed by a dark, static, phase and subsequent fading;
- Occur when mid-afternoon temperature are greater than $250 - 270$K.

According to this definition, RSL are distinct from other processes that appear as dark features, which can misinterpreted as RSL:

- Rock falls, which appear as dark lineae like RSL but occur on a much shorter timescale, without showing incremental lengthening and annual recurrence (McEwen et al.,2011);
- Dark slope streaks, a phenomenon associated with the removal of dust which exposes the underlying darker regolith. This results in dark streaks, very similar to RSL dark markings. The removal of dust associated with dark slope streaks can be produced by winds or by the downfall of dust itself on over-steepened slopes. (Hansen et al.,2011) Although they resemble RSL, they are a distinct phenomenon as they are found in places with a high dust content where no RSL are observed. They are much bigger than RSL and do not show annual recurrence: an example is depicted in figure (2.6A);
- Gullies, which are a widespread phenomenon on the Martian surface, and are generally due to the downslope transport of sediments

triggered by the defrost of CO_2 ice (Malin and Edgett,2000; Hansen et al.,2011). They can have different forms, as depicted in figures (2.6B, C) and are traditionally divided in *classic Gullies*, which have an alcove-channel-apron shape and *linear Gullies*, which resemble RSL as they appear as dark markings. Together with RSL, Gullies are the main active process occurring on the present Martian surface. What distinguishes linear gullies from RSL is their fading timescale, which is greater than 1 year, at least.

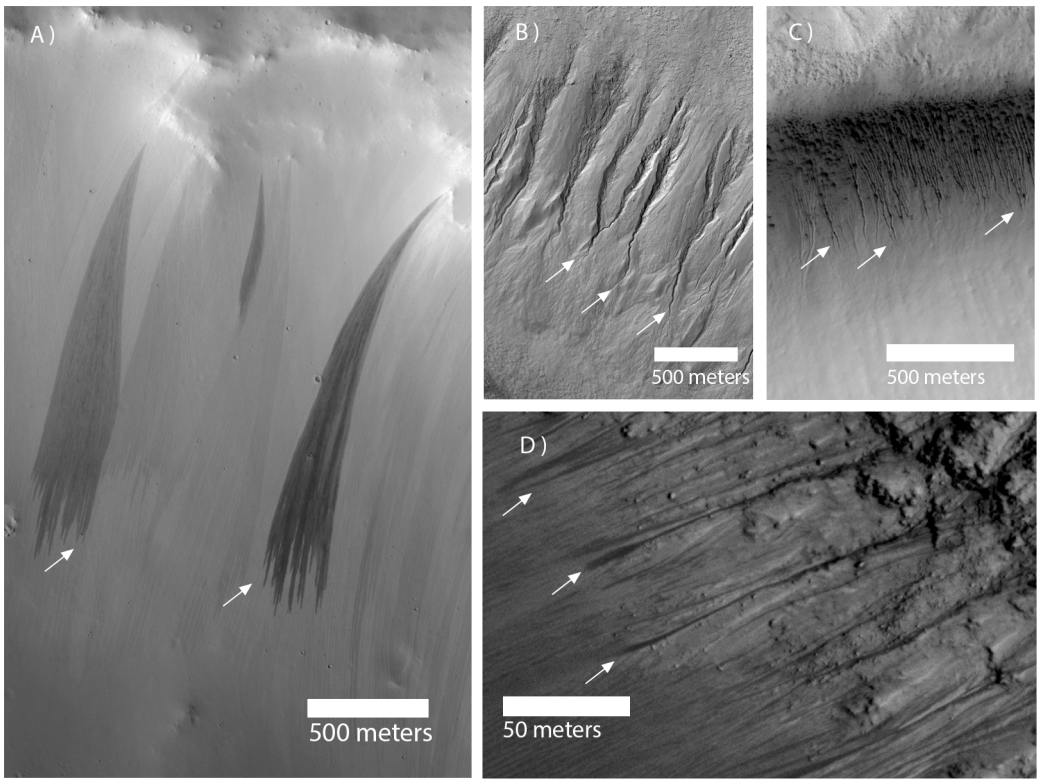

Figure 2.6: White arrows points to: A) Dark slope streaks in Arabia Terra (3.680°N, 26.069E) from HiRISE image ESP_012410_1835. B) Classic gullies on the walls of a southern crater located in (−40.304°N, 196.831°E) from HiRISE image PSP_005930_1395. C) Linear gullies in Hellas Planitia (−48.329°N, 73.703°E) from HiRISE image ESP_037014_1315. D) Recurring Slope Lineae in Juventae Chasma (−4.691°N, 298.577°E). For A), B) and C) North is up; for D) North is down. All images are publicly available at `https://www.uahirise.org/`.

Several hypotheses have been put forward to explain the nature of RSL. We will here divide them in two classes: *"wet models"*, which invoke liquid water, and *"dry models"* which are essentially dry flows of debris or granular material that envision a very limited role for any volatile.

Wet models

According to *"wet models"* RSL are due to liquid water, with eventually a salt component (in this case, we speak of *"brines"*), which has a different origin depending on the model. Activity starts in hot seasons, as soon as temperatures rise over the freezing point of water or brines. This water would darken the regolith and eventually evaporate, resulting in the fading of RSL in cold seasons, as soon as temperatures drop. Activity

starts with a incremental lengthening phase, as observations shows, in which the water input from the source is greater than the evaporative losses. However, as temperature rises and RSL area increases, the latter becomes greater and greater until it balances the input from the water source, resulting in an *"equilibrium phase"*; in this phase RSL no longer lengthen but remain dark. Eventually evaporation dominates when temperatures drop, freezing all the water and quenching the input; at this stage the dark lineae fade away quickly. *Wet models* differ in the role of water and its origin; in the following paragraphs we will describe all the relevant hypotheses which have been put forward up to now.

Deliquescence of water vapour by hygroscopic salts

Deliquescence is the absorption of *atmospheric* water vapour is by hygroscopic salts. According to the scenario, this absorbed water vapour is released to form RSL (McEwen et al.,2011; McEwen et al.,2013a; McEwen et al.,2015). Deliquescence would work very well in polar and high latitude regions, where the relative humidity is high, but has been proven to unlikely explain RSL because their activity do not correlate with peak water vapour concentration and the quantity of trapped water would be very low in the present Martian atmosphere.

Wet debris flows

In this case RSL would be originated from a surface flow or seep of wet debris triggered by the melting of a frozen aquifer during hot seasons (McEwen et al., 2011). Darkening here is not due to wetting of the surface, because water would rapidly evaporate, but to the change in grain size and roughness operated by the debris flow. Despite seasonality, recurrence and darkening of RSL would be explained, the fading would be problematic as it would require an opposite change in grain size, for which a viable mechanism has not been identified yet.

Briny surface flows

In this case RSL would be originated from surface flows or seeps of liquid briny water, resulting from the seasonal melting of a frozen aquifer (McEwen et al., 2011). Briny water is more stable on the Martian surface since salts can lower significantly (up to ten times) the evaporation of brines (Altheide et al.,2009), hence darkening here can be explained by both grain size sorting and wetting; fading would then be explained via evaporation and consequent dehydration of the regolith. However, even tough brines are more stable than water on the Martian surface, they can last only some hours.

Briny flows in the shallow subsurface

Unlike previous cases the flow occurs in a thin layer in the shallow (< 50 cm) subsurface; the flow is powered by the melting of a frozen ice source, and it is subject to evaporative losses. Darkening is explained by mois-

turizing of the regolith by water, and fading is due to evaporation, which dominates as soon as the water input is quenched by the freezing of the ice source. (Grimm et al.,2014). This conceptual model is shown in figure (2.7).

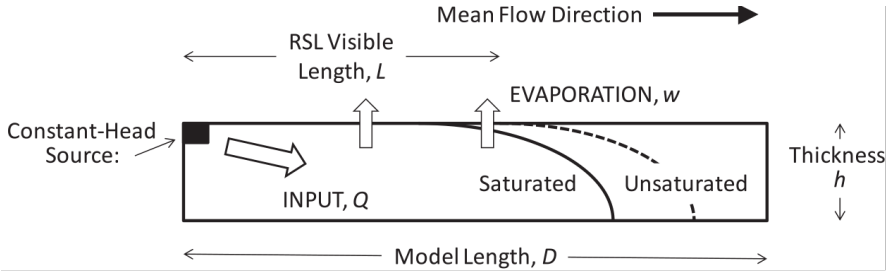

Figure 2.7: Conceptual model for wet-dominated RSL, from figure (2) of Grimm et al. (2014). RSL flows in a thin layer and are subject to a water input and evaporation. The flow causes the soil to saturate, which results in its darkening.

Among these *"wet models"*, the *briny subsurface flow* is the most likely as it better explains observations: in particular, it gives the best explanation for fading. Recurrence, instead, is accomplished by assuming the presence of a briny ice source. Numerical modeling by Chevrier and Rivera-Valentin (2012) showed that brines can melt in the top centimeters of the subsurface at time and places when RSL are active, and remain stable against evaporation during all the the duration of RSL. Brines are thought to have formed by the interaction between the Martian hydrosphere with its reactive basaltic lithosphere, froze during the end of the warm period at the late Noachian, and are expected to be preserved in the subsurface (Knauth and Burt, 2002). Droplets of brines have been detected on Mars on the struts of the Phoenix Mars Lander (Renno et al.,2009) and spectral analysis performed with CRISM, as detailed in section (2.1), detected the presence of hydrated salts in correspondence of RSL activity, which strongly support the presence brines at RSL sites.

Despite these facts, *"wet models"* share the common problem of lacking a plausible water source, which is currently investigated: Grimm et al. (2014) estimates a water budget of $2 - 10$ m^3 per m of RSL, resulting in a water volume of 10^4 to 10^6 m^3 of fluid for RSL in Coprates and Melas Chasma, two particularly RSL-rich regions in Valles Marineris (Chojnacki et al., 2016). However, these estimates assume a thickness of the wet layer which is not proven. Such water budgets are at least one order of magnitude greater than those provided by ice in the shallow subsurface ($<$ 400 m), and this ice would not survive in equilibrium with the atmosphere since temperatures are too high; out-of-equilibrium ice, instead, would be rapidly depleted near the surface (Mellon et al.,1997). Another option is the presence of regional groundwater basins (Stillman et al., 2014; Grimm et al., 2014); however, as some VM RSL occurs on local 100 m high topographic highs where the presence of an underlying aquifer capable of sourcing from 10^4 to 10^6 m^3 of water is problematic, this option was deemed unlikely (Chojnacki et al., 2016). Stillman et al. (2016) instead suggested that CAP RSL could be powered by a either a shallow or deep liquid briny aquifer which is connected to the surface via fractures or faults. During cold seasons these fractures freeze cre-

ating and ice dam. As temperatures rise this ice dam is breached and the aquifer discharges to the surface, forming RSL. At this stage they incrementally lengthen since the discharge rate is greater than evaporation. As temperatures rises, evaporation matches the discharge rate and the lengthening slows and eventually stops. Finally, when temperatures decrease, the ice dam forms again, quenching the water input, and RSL rapidly fade. According to Chojnacki et al. (2016) this mechanism could work also in Valles Marineris, provided that viable pathways to the subsurface exists. Fractures and faults may be plausible pathways, since many bedrock outcrops from which numerous RSL are sourced are highly fractured (Watkins et al., 2014).

Dry flow models

These models envision a limited role for volatiles, like water or brines, and explain RSL as essentially water-free process. The main hypothesis, advanced by Dundas et al. (2017), is that RSL are caused by the downslope movement of fine granular material which would appear dark because of particle size and roughness effects. This hypothesis is supported by the fact that RSL have been observed to propagate only until the slope is near 30° (Dundas et al., 2017) which is the angle of repose of granular flows. These idea is intriguing, because it implies a limited role for water and does not pose the problem of finding a plausible water source. However, it does not explain seasonality, recurrence, fading and the detection of hydrated salts at RSL sites (Ojha et al.,2015). The fading is still unexplained, while to address seasonality and recurrence, two mechanism have been proposed: the first involves the displacement of grains caused by boiling water (Massé et al.,2016) and the second involves the displacement of grains triggered by intra-grain pressure gradients (Schmidt et al., 2017).

Wet-triggered debris flow

Laboratory experiments by Massé et al. (2016) showed that freshwater at 293 K at the top of 1 mm of regolith boils, displacing grains to form a mm-high ridge. This ridge increases the local slope angle above the angle of repose of granular material, which flows downslope. Water then flows downhill, repeating this process and producing the observed incremental lengthening. The presence of a thin film of freshwater would explain the decrease in albedo (Massé et al., 2014) and the lack of water spectral features, as they would be under the threshold of current orbital instruments (Massé et al., 2016). These model is intriguing, as it requires a very limited quantity of water, but it requires both freshwater and high temperatures for boiling. The last condition is not met for SML RSL, as their *"first pulse"* is observed to be active during early spring, when temperatures are colder than 273 K.

Rarefied gas-triggered debris flow

Schmidt et al. (2017) introduced a granular flow to explain RSL in Garni crater, a well-documented confirmed site in Valles Marineris (11.5°S,

290.3°E). They invoke a Knudsen pump (Knudsen, 1910) to seasonally reduce the angle of repose of grains and trigger a dry granular flow. A Knudsen pump is a process in which, under low pressure conditions, temperature gradient are able to move particles from the hot end to the cold end. This process occurs in the top $100 - 200$ μm of the Martian soil and despite having been advocated to explain dust-lifting processes (Wurm et al., 2008), is generally too weak to uplift grains. Instead, this process is enhanced by shadows casted by boulders, which generate strong temperature gradients close to the surface. In this case the pump is said to be *"enhanced"*, as it exerts a greater uplifting force which opposes to gravity. This is equivalent to a situation with reduced gravity, that for granular flow translates in a reduced angle of repose (in presence of reduced gravity, the same flow can be obtained with lower slopes). According to Schmidt et al. (2017), shadows casted by boulders at Garni crater create enhanced temperature gradients which results in *enhanced* pumps, that lower the angle of repose below the observed slope angle and triggers the flow. This phenomenon is also seasonal, as temperature gradients will be greater in hot seasons and lower in cold seasons. In this scenario, the relative darker albedo would be due to the sorting of the grains during the flows, while fading would be due to the aeolian deposition of the finer grains from the atmosphere. Despite the predicted decrease of the angle of repose by the Knudsen pump matches RSL activity on Garni crater (Schmidt et al.,2017), it predicts the presence of RSL also on slopes where they are not observed. Moreover, since this mechanism occurs only in correspondence of shadows, it is not clear if it can displace material incrementally over all the length of RSL, hundreds of meters downslope. Another flaw is that it does not explain the *"first pulse"* of SML RSL, which occurs at lower temperatures. Finally, the proposed mechanism to explain the fading by grains deposition would not work for most RSL as no visual evidence of aeolian features deposing material has been detected at the HiRISE resolution (Stillman and Grimm, 2018).

In summary, dry granular flows are interesting because they involve zero or very limited quantities of water, which can be provided by ice in the shallow subsurface. Moreover, they can explain why RSL terminate on slopes $\approx 30^\circ$, i.e. near the angle of repose of granular flow, while water-based flow are expected to propagate further (Dundas et al.,2017). Stillman and Grimm (2018) argued that after the MY 28 global encircling dust storm RSL lengthened more, as a consequence of the heating induced by the storm. According to these authors, this behavior means that RSL activity, and in turn their length, is limited more by temperature than by the slope angle, even though temperature is not the only variable affecting RSL activity. This aspect is more indicative of a wet-dominated process originating RSL. Moreover, dry granular flow are criticized because they do not explain some other behaviors of RSL such as their ability to propagate over bedrock and to disappear and reappear some meters downhill, which would instead be explained by differences in capillarity by wet dominated models (2018,Stillman and Grimm).

To conclude, the scientific community is still debating on which phenomenon might drive Recurring Slope Lineae. Two leading theories are being evaluated, one concerning dry flows of granular material and the other wet-dominated flows of briny water. To date, each model can explain some observations, but has unresolved issues. A precise evaluation of both theories on a common experimental dataset is still missing and would prove useful in establishing which model is more likely

Chapter 3

Data Analysis

The study of Recurring Slope Lineae that we will perform in this thesis is organized in two parts: the first is detailed in section (3.1) and it is a global survey of all candidate and confirmed sites where RSL have been identified. The main aim of this part is to create the most complete catalogue of RSL to date. For all sites in the catalogue we study the global properties of the Martian surface, i.e. their elevation, slope, thermal inertia, rock abundance, dust cover index, albedo and water equivalent hydrogen. Such catalogue enables us to perform a statistical characterization of the global properties of RSL sites, which is the most extensive and update one at the time of writing and it will be used to find new potential RSL sites.

The second part is detailed in section (3.2) and presents a specific case study of RSL in Raga crater, a well observed confirmed site, where we measure key properties of individual RSL such as their length as a function of time, slope and terrain orientation.

3.1 Survey of Recurring Slope Lineae and their global properties

To date RSL have been mainly identified with the HiRISE camera, i.e. the only instrument capable of resolving such small features. RSL are defined as *confirmed* if they meet the definition given in (2.2) i.e. if they appear a) darker than the surroundings, b) they incrementally lengthen and c) fade and re-occur in the same places. In some cases, only a subset of these conditions is met; for example, the lack of repeated images can prevent the observation of the lengthening and fading phases and the annual re-occurrence; in such cases RSL are defined as *candidates*, as more observations are needed to discern between RSL or other features, like rockfalls or dark slope streaks.
To create a catalogue of RSL, we identified and merged all sites studied in literature (McEwen et al.,2011; Stillman et al.,Stillman et al.; McEwen et al.,2013b; Stillman et al.,2016; Chojnacki et al.,2016; Stillman et al.,2017; 2018,Stillman and Grimm). This allowed us to catalog a total of 555 sites, out of which 462 are candidates and 93 are confirmed RSL. The majority of them lies within Valles Marineris (203 candidate and 40 confirmed), followed by those in the southern mid latitudes (167 candidate

and 40 confirmed); 84 sites are in the equatorial highlands, where 79 are candidate and 5 confirmed; finally 24 sites are in Chryse and Acidalia Planitiae, of which 16 are candidate and 8 confirmed. The geographical distribution of confirmed sites is shown in figure (2.1).

In order to have a general picture of RSL properties, we compute elevation, slope angle, thermal intertia, rock abundance, global albedo, dust cover index and the water equivalent hydrogen of RSL sites. All these quantities are here described.

Elevation and Slope angle

Elevation has been computed at RSL sites from the Mars Orbiter Laser Altimeter (MOLA,Smith et al., 2001) digital elevation model (DEM), which samples the elevation of all the Martian surface at spatial resolution of 463 m and an uncertainty of 3 m. From this DEM we computed the slope angle, at the same spatial scale, using the implementation of the Burrough and McDonnell (1999) algorithm provided by the ArcMap® software. The elevation map is shown in figure (1.1).

Thermal Inertia

Thermal inertia represents the ability of a material in storing and conduct its internal energy. It is defined as:

$$I = \sqrt{k\rho c} \tag{3.1}$$

where k is the thermal conductivity, with units ($\mathrm{Wm^{-1}K^{-1}}$), ρ is the density (with units $\mathrm{kg\,m^{-3}}$), c is the specific heat capacity, with units ($\mathrm{J\,Kg^{-1}K^{-1}}$). Thermal inertia is measured in ($\mathrm{J\,m^{-2}K^{-1}s^{-\frac{1}{2}}}$) which are often referred as "TIU" (Thermal Inertia Units, 1 TIU $= 1\ \mathrm{J\,m^{-2}K^{-1}s^{-\frac{1}{2}}}$ Putzig and Mellon, 2007).

In the context of planetary surfaces, thermal inertia measures the ability of the surface to store heat during the day and release it during the night. It depends on the properties of the surface, such as particle size, rock abundance and exposure, and it affects the surface temperature. As an example, sands have low thermal inertia, and thus can store and release heat quickly; on the contrary rocks have a high thermal inertia, so they store and release thermal energy on a longer timescale.

Thermal inertia can be derived from infrared observations; in such a case we distinguish between daytime thermal inertia, computed from observations performed during the local day, and night-time thermal inertia, computed from observations performed during the local night. The latter are usually preferred as they are less affected by temperature variations induced by the topography, which instead affect daytime observations as the most illuminated slopes are systematically hotter (Edwards and Piqueux, 2016). For each RSL site, we computed both its daytime and night-time thermal inertia from the global maps of Putzig and Mellon (2007), which have a spatial resolution of 3 km, derived from MGS-TES

brightness temperatures. Such maps are depicted in figures (3.1) and (3.2).

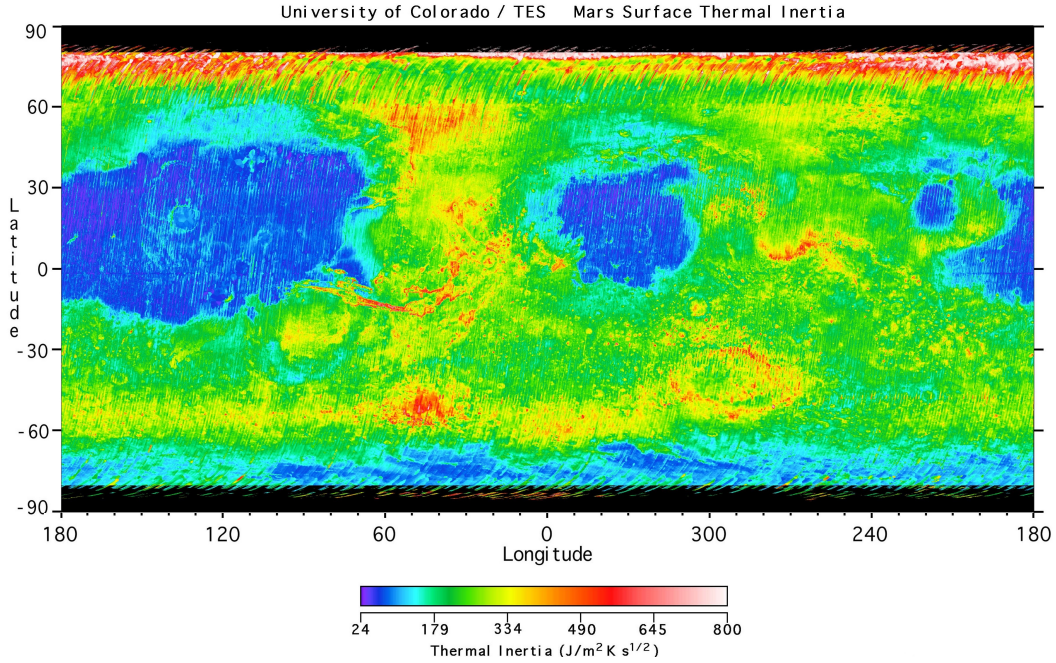

Figure 3.1: Daytime thermal inertia map from Putzig and Mellon, 2007)

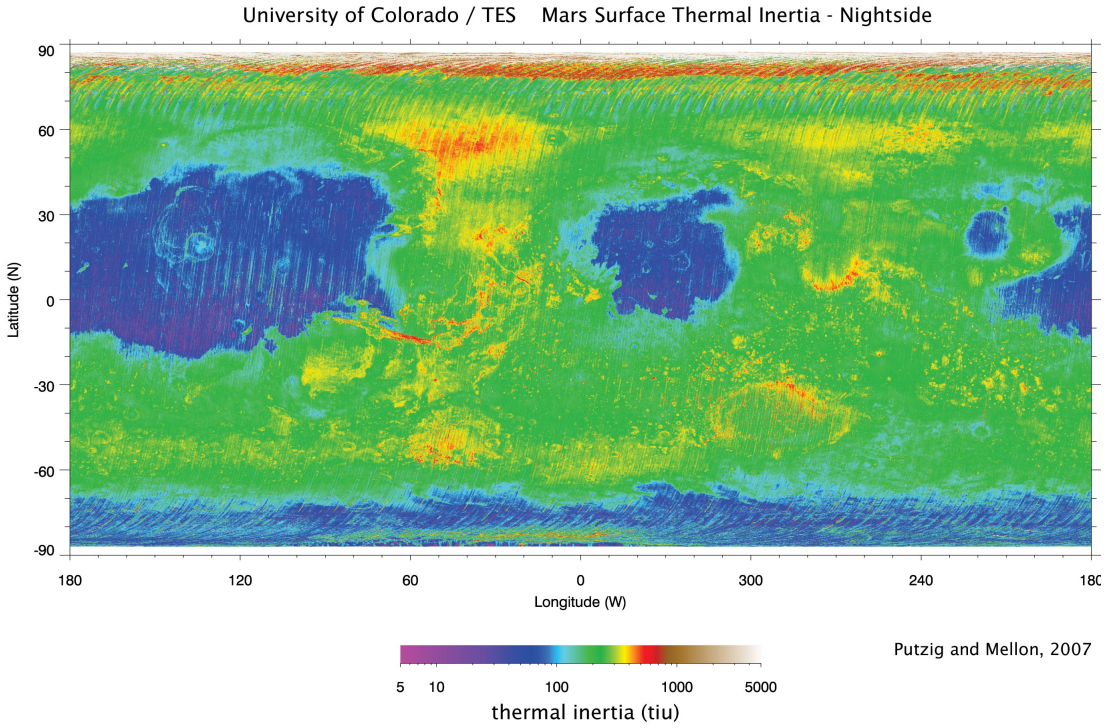

Figure 3.2: Night-time thermal inertia map from Putzig and Mellon, 2007)

Rock abundance

The rock abundance (K) is the areal density of rocks. Wwe compute K from the map of Christensen (1986), shown in figure (3.3). Such map has a resolution of 60 km and it is derived from Viking Infrared Thermal Mapper (IRTM, Kieffer et al.,1972) observations. A value of $K = 40\%$

means that the corresponding 60 km by 60 km pixel is covered for the 40% by rocks.

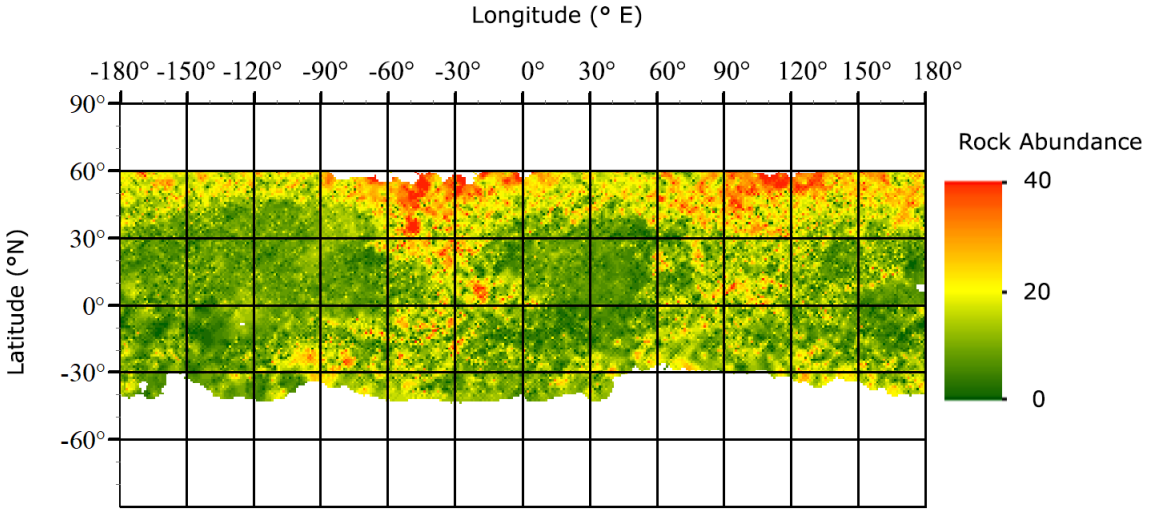

Figure 3.3: Viking IRTM rock abundance map from Christensen (1986)

Global albedo

The Lambert albedo of RSL sites, which is the ratio between the emitted and incident energy fluxes, was derived from the TES albedo maps (Christensen et al., 2001), where it is computed as:

$$A_L = \frac{RD^2}{S\cos(i)} \tag{3.2}$$

where R is the calibrated radiance, representing the energy emitted by the surface, D is the Sun-Mars distance, S is the Solar radiance integrated over the TES bolometer spectral response, representing the incident energy, and i the incidence angle (Christensen et al., 2001). Such map has a resolution of 7.5 km and is depicted in figure (3.4).

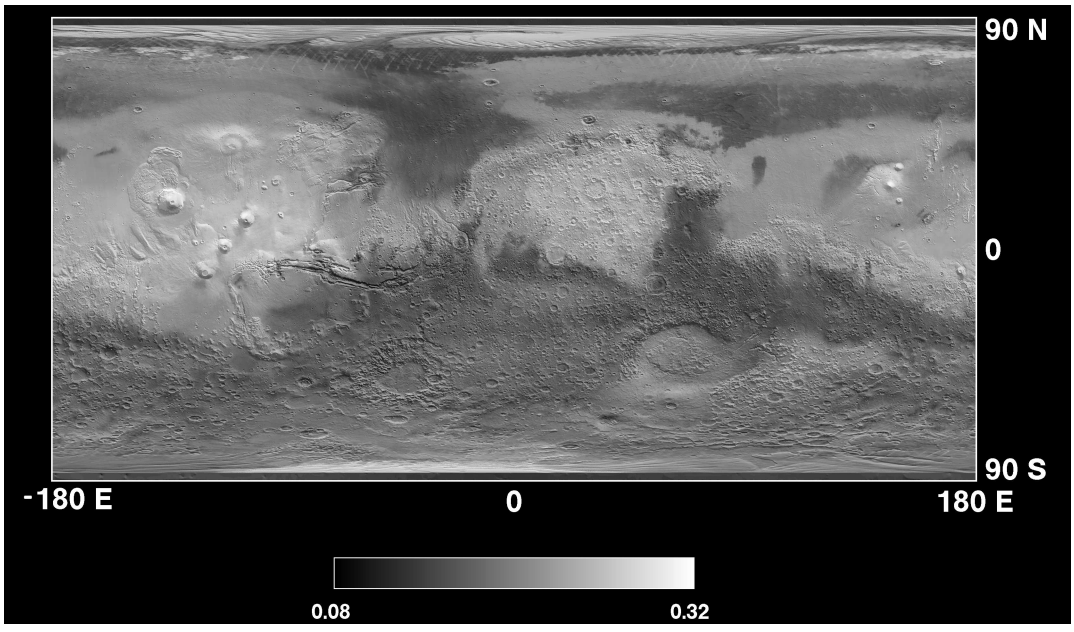

Figure 3.4: TES albedo map from Christensen et al. (2001).

Dust Cover Index

The content of dust above the Martian surface is measured by the *Dust Cover Index* (DCI), developed by Ruff and Christensen (2002) from TES observations. Typical "dusty" areas have a DCI ≈ 0.931 while "dust free" areas have a DCI ≈ 0.97. We extracted the DCI of all RSL sites from the map of Ruff and Christensen (2002), at a resolution of 3.5 km.

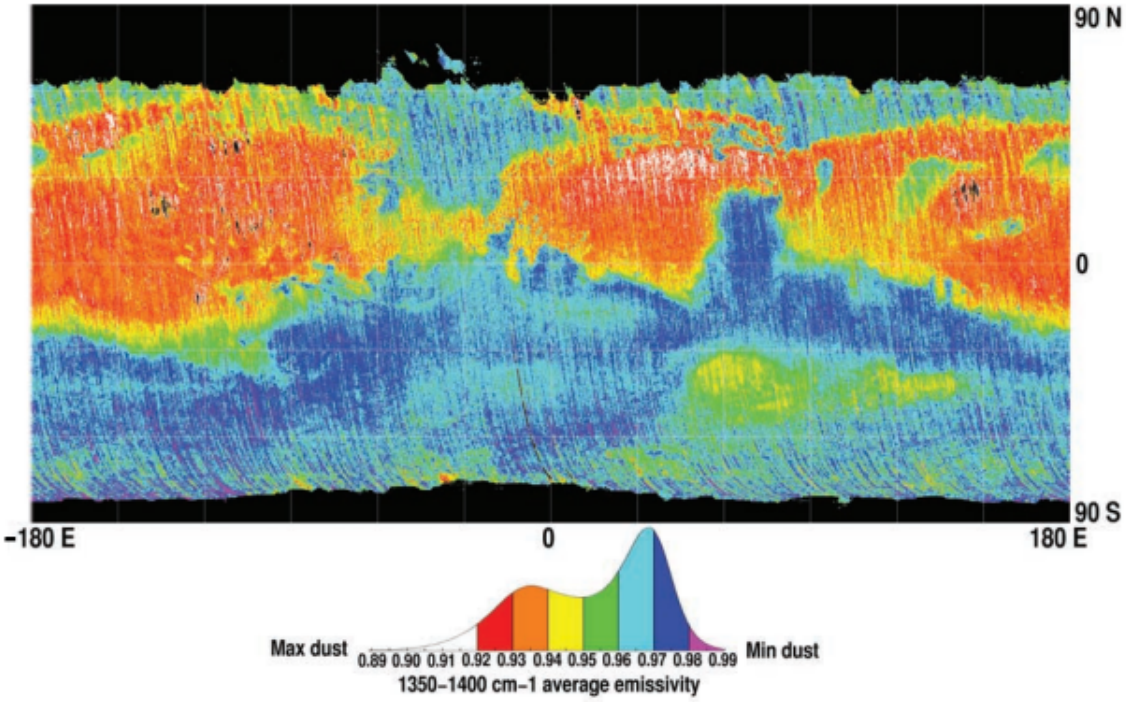

Figure 3.5: Dust Cover Index map from figure (14) of Ruff and Christensen (2002). Orange, red, and white colours indicate dust covered areas, while blue and magenta areas are dust-free. Spatial resolution is 3.5 km.

Water equivalent Hydrogen

Water equivalent hydrogen is the mass fraction of H_2O corresponding to a certain Hydrogen mass fraction (Feldman et al., 2004). Neutrons and gamma rays are emitted as a result of collisions between cosmic rays and atoms on the surface. When cosmic rays interact with atoms they generate neutrons at energies lower than 0.4 eV (*thermal* neutrons), between 0.4 eV and 0.7 MeV (*epithermal* neutrons) and from 0.7 to 1.6 MeV (*fast neutrons*) (Feldman et al., 2004). These neutrons may scatter with surrounding nuclei, exciting them and producing gamma rays, or escape, reaching the surface and being detected by orbital detectors. Some elements in the soil can instead *capture* neutrons, resulting in a decrease of the number of neutron reaching the surface. Hydrogen is particularly effective in this process, and its presence produces both a decrease of *epithermal* and *thermal* neutrons and a spectral line at 2223 KeV. Both these effect were measured by the Mars Odyssey Gamma Rays Spectrometer and Neutron Spectrometer, and related to the water content of the Martian surface in terms of its water equivalent hydrogen (Boynton et al.,

2002; Feldman et al., 2004; Wilson et al., 2018). In particular, we use the values computed by J. Wilson (Wilson et al., 2018, private communication) for all RSL sites in our catalogue. These values are indicative of the water content in the uppermost meter of the surface, at resolution of approximately 300 km.

3.1.1 RSL catalogue and global properties

We here summarize our catalogue, while all rows are included in appendix A. Every row refers to a single RSL site and columns represents:

- LAT: North-positive latitude of the site, in decimal degrees;
- LON: East-positive longitude of the site, in decimal degrees
- STATUS: either "1" for *confirmed* sites or "0" for candidate sites;
- TYPE: either "SML" for southern mid latitudes RSL, "EQ" for Equatorial RSL, "CAP" for RSL located in Chryse and Acidalia Planitia and "VM" for RSL located in Valles Marineris;
- H: MOLA elevation in metres. All values have an uncertainty of 3 m. (Smith et al., 2001).
- S: MOLA slope, in decimal degrees;
- TI_d: daytime thermal inertia, in TIU. Values have a relative uncertainty of 0.06 (Putzig and Mellon, 2007).
- TI_n: night-time thermal inertia in TIU. Values have a relative uncertainty of 0.06 (Putzig and Mellon, 2007).
- K: rock abundance. Values have a relative uncertainty of 0.2 (Christensen, 1986).
- A: global albedo;
- DCI: dust cover index;
- WEH: water equivalent hydrogen in units of H_2O mass fraction (% wt);

Region	Status	Lat	Lon	H	S	TI_d	TI_n	K	DCI	A	WEH
VM	1	-15.49	308.53	-3327	22	268±16	472±28	11±2	0.141	0.9704	5
VM	1	-15.40	309.54	-1333	23	192±11	402±24	19±3	0.123	0.9702	5
VM	1	-14.70	304.30	-3622	20	52±3	345±20	6±1	0.115	0.9607	5
VM	1	-14.60	302.40	-1924	25	325±19	427±25	1±1	0.121	0.9704	5
VM	1	-14.40	304.60	-1487	28	469±28	365±21	6±1	0.112	0.9704	5

Table 3.1: First rows of the catalogue, which is reported in Appendix A.

To summarize our catalogue, we plot the distributions of themost important variables, which will be discussed in the next section. Since distributions are far from gaussian, we compute the median to express their central tendencies. Instead their variability is expressed through the width of the central 50% of the distribution, defined by values of the 25-th and 75-th percentiles. All these values are reported in table (4.1).

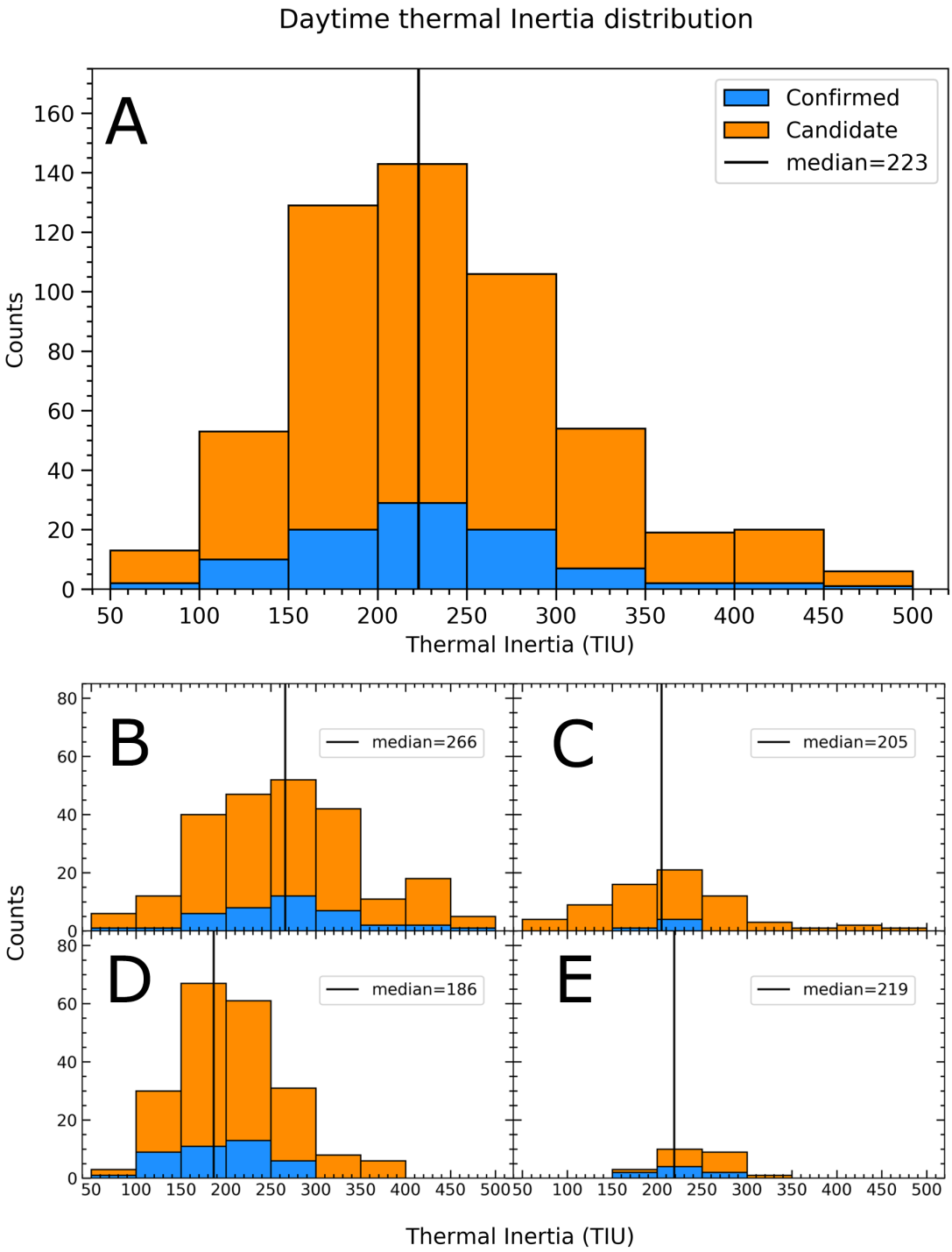

Figure 3.6: Distributions of daytime thermal inertia for (A) all candidate and confirmed RSL sites, (B) VM RSL, (C) EQ RSL, (D) SML RSL, (E) CAP RSL. Black lines represent median values for confirmed RSL.

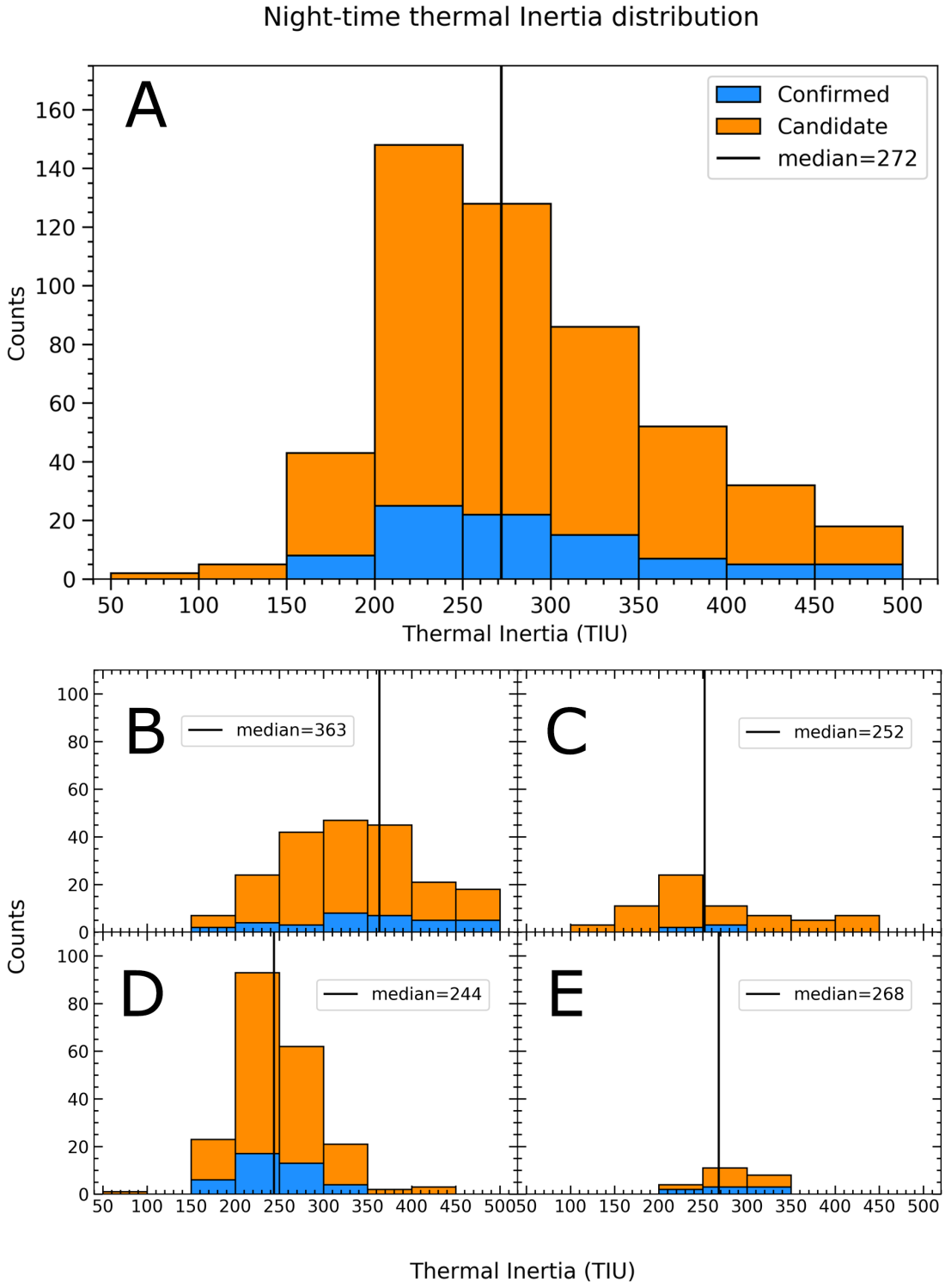

Figure 3.7: Distributions of night-time thermal inertia for (A) all candidate and confirmed RSL sites, (B) VM RSL, (C) EQ RSL, (D) SML RSL, (E) CAP RSL. Black lines represent median values for confirmed RSL.

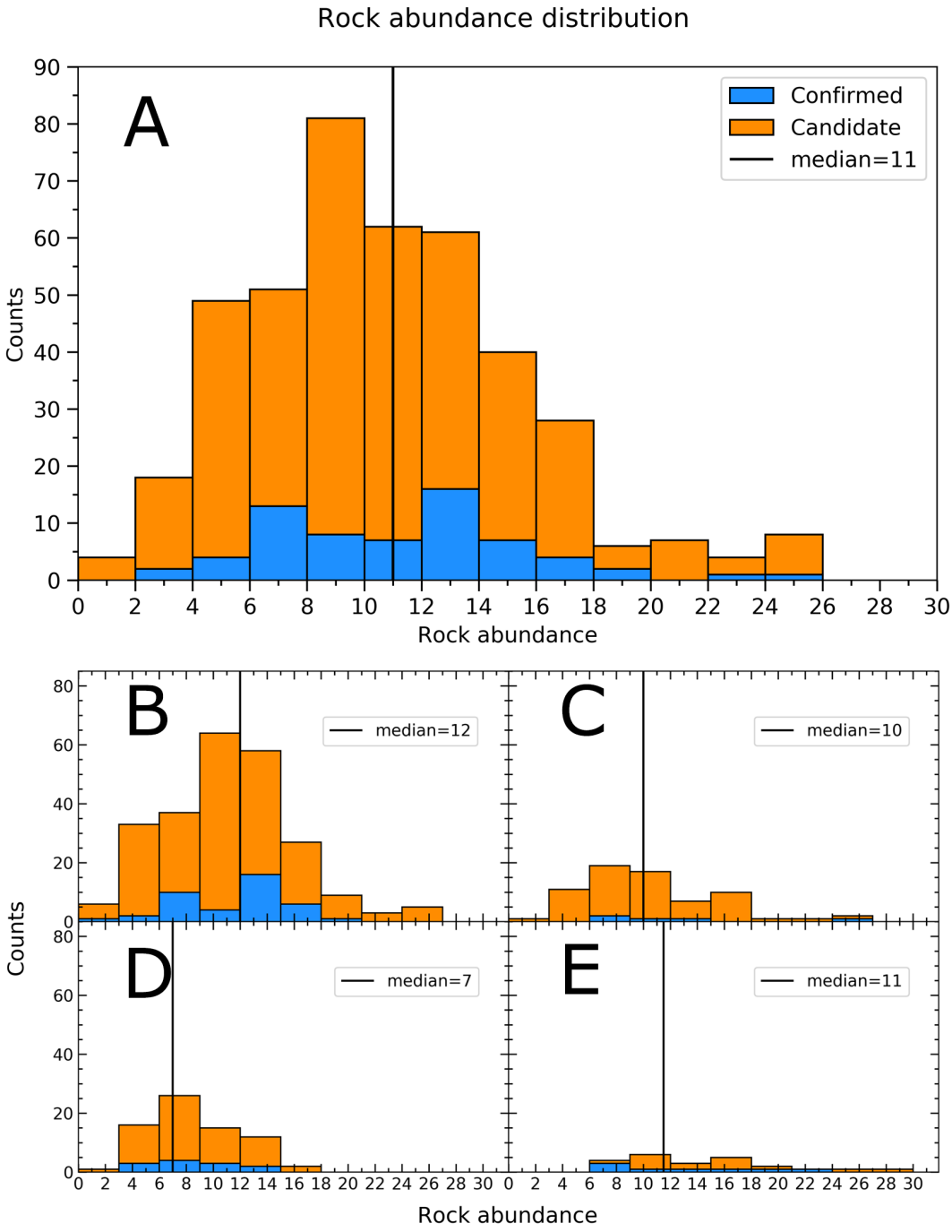

Figure 3.8: Distributions of rock abundance for (A) all candidate and confirmed RSL sites, (B) VM RSL, (C) EQ RSL, (D) SML RSL, (E) CAP RSL. Black lines represent median values for confirmed RSL.

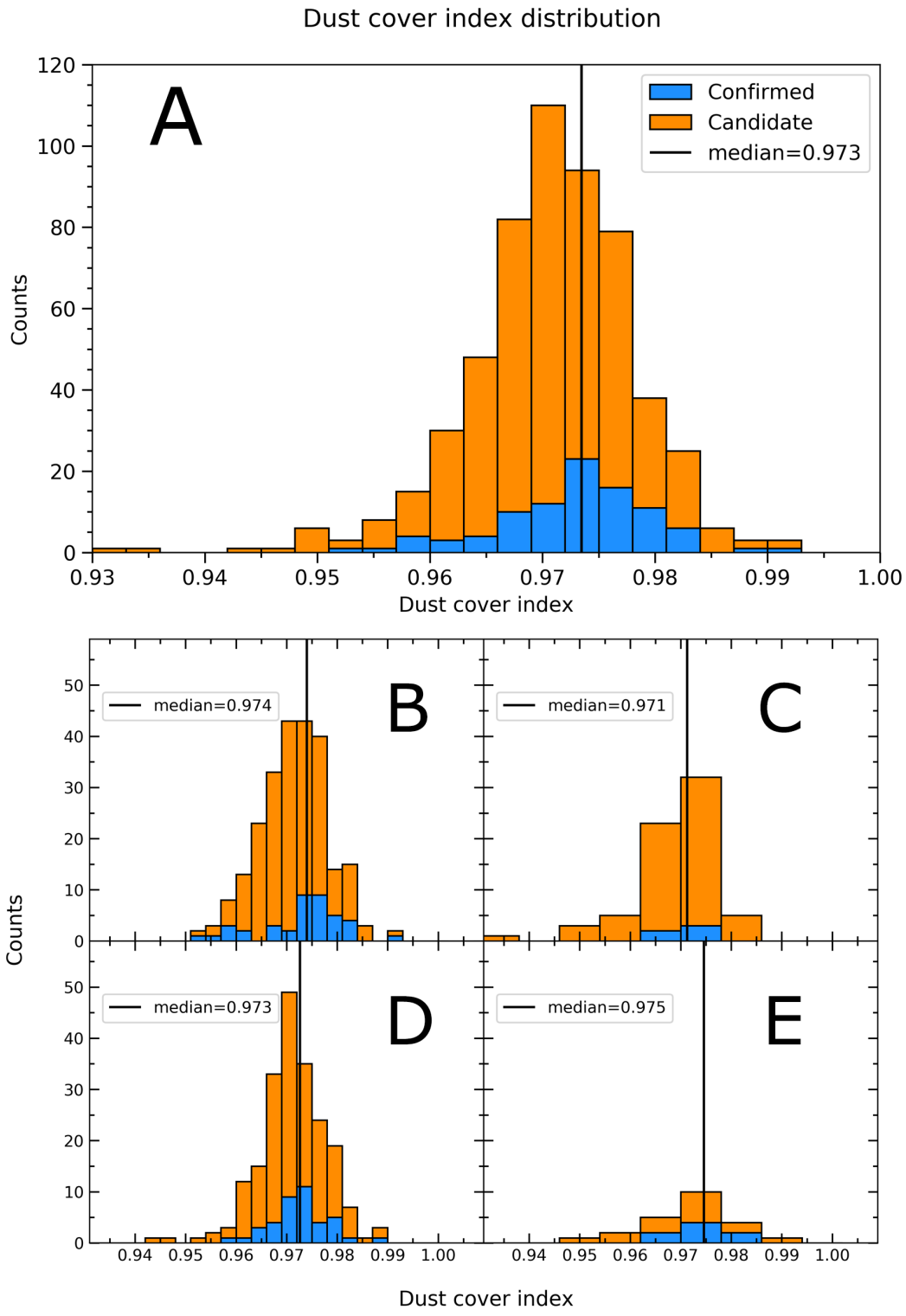

Figure 3.9: Distributions of dust cover index for (A) all candidate and confirmed RSL sites, (B) VM RSL, (C) EQ RSL, (D) SML RSL, (E) CAP RSL. Black lines represent median values for confirmed RSL.

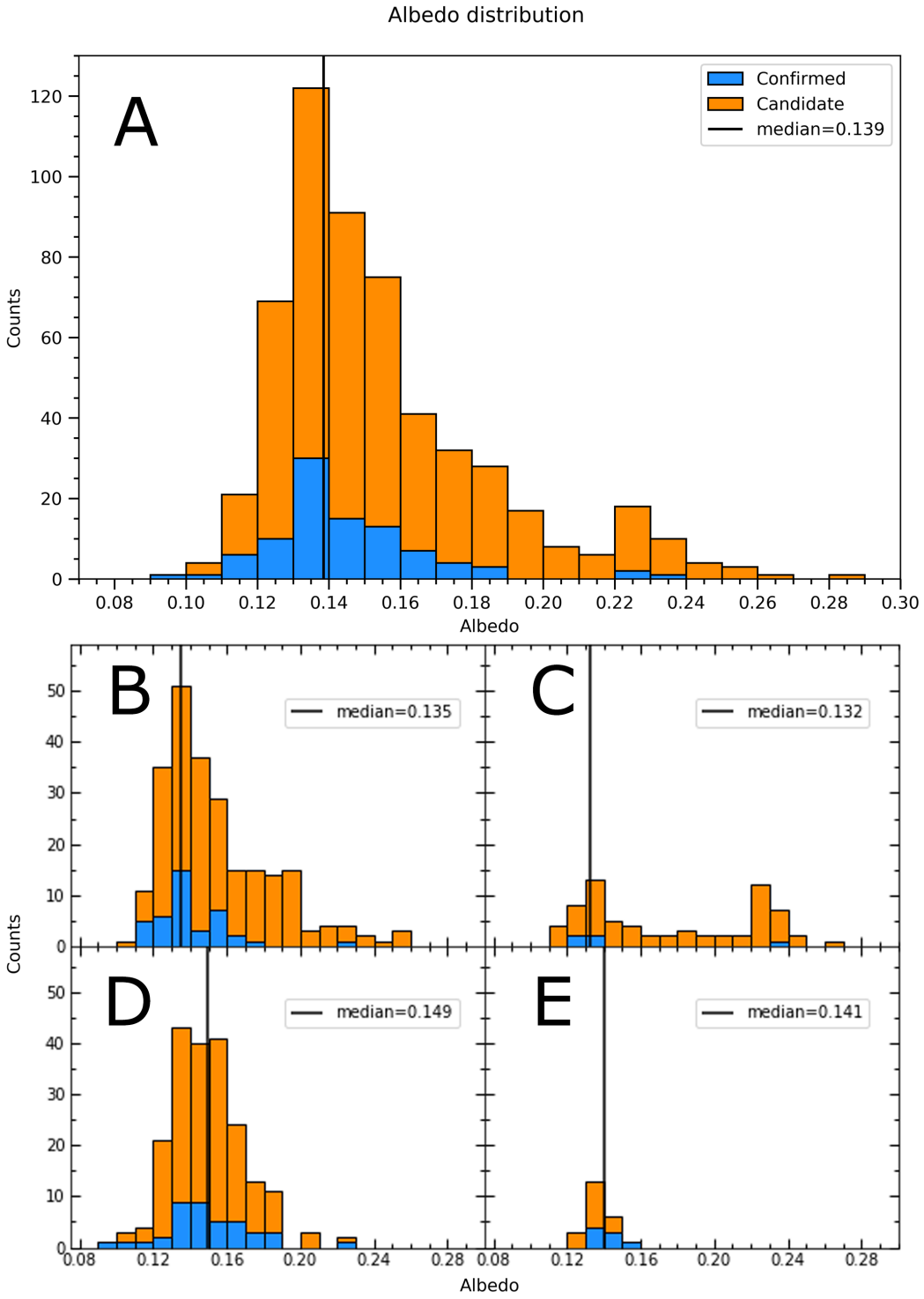

Figure 3.10: Distributions of albedo for (A) all candidate and confirmed RSL sites, (B) VM RSL, (C) EQ RSL, (D) SML RSL, (E) CAP RSL. Black lines represent median values for confirmed RSL.

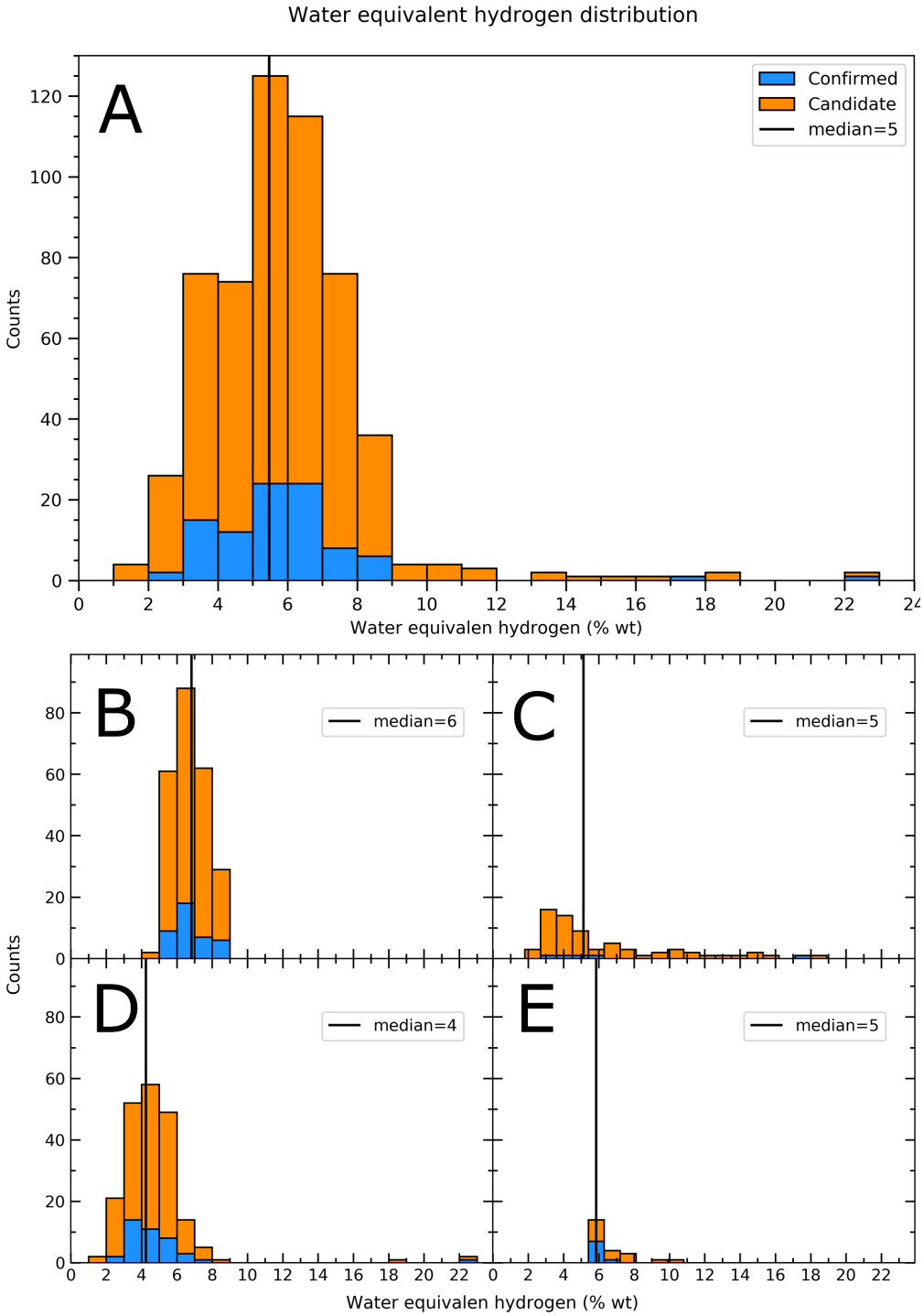

Figure 3.11: Distributions of water equivalent hydrogen for (A) all candidate and confirmed RSL sites, (B) VM RSL, (C) EQ RSL, (D) SML RSL, (E) CAP RSL. Black lines represent median values for confirmed RSL.

3.1.2 Potential RSL sites

The catalogue of RSL enabled us to identify all regions of the Martian surface having the same surface properties of our sample, which can thus be considered as potential targets to be searched for RSL. To do so we computed the ranges of all variables defined in section (3.1) for all *confirmed* RSL and queried all the relative maps within these ranges. Such regions are depicted in figure (3.12).

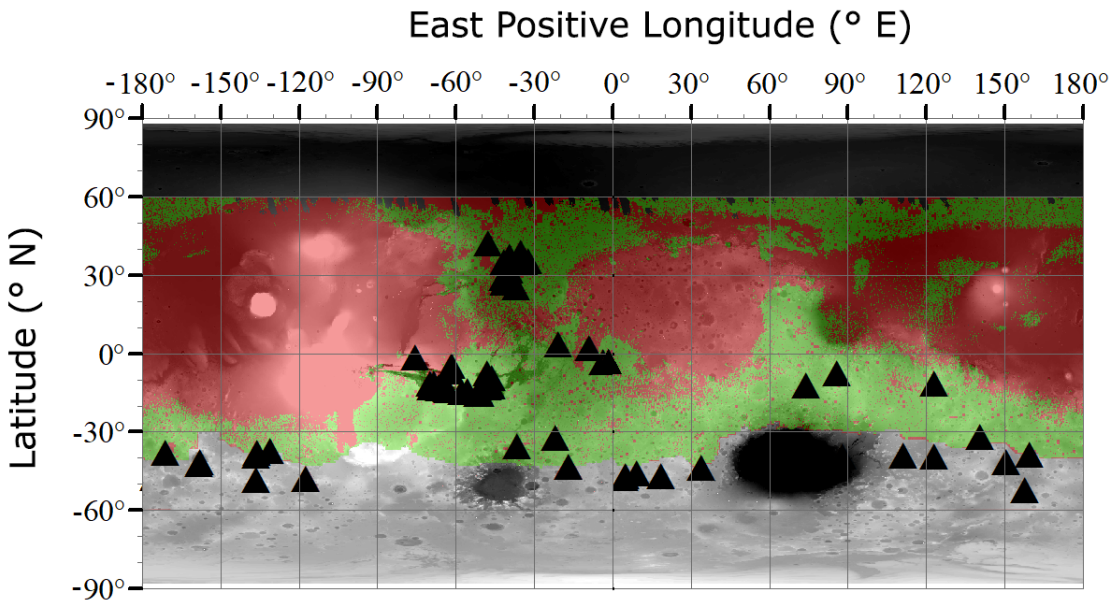

Figure 3.12: In green, regions of the surface having surface properties within the ranges of those of all confirmed RSL sites. In red, regions with surface properties outside the ranges of those of all confirmed RSL sites. In the background, a greyscale MOLA elevation map. Regions that are not either red or green are not mapped in one or more global maps. Black triangles represent the locations of all confirmed RSL sites.

3.2 Study of RSL in Raga crater

In this section we describe the analysis of single RSL in Raga crater, a well observed confirmed site located in (−48.1N, −117.56E). Its geographical position and a HiRISE image are shown in figures (3.13A) and (3.13D). This site was selected because it is a good compromise between extensive imagery, a large number of well visible RSL, the presence of a *digital terrain model* (DTM) and several *orthorectified* images. A DTM of a region is a dataset of elevation measurements of the region. A HiRSE DTM is derived from two images of the same region, called *stereo pairs*, and samples its elevation with a spatial resolution of 1 m and an uncertainty of 30 cm (Kirk et al.,2008). *Orthorectified* images are derived from original images, when a DTM is used to convert these in *nadir* pointing images. Their usefullness is that orthorectified images have the same viewing geometry, and thus they are not affected by parallattic distortions. All these aspects, described and motivated in section (3.2.1), are essential to measure RSL key properties such as their length as function of terrain

elevation, slope and aspect (i.e. the angle between the normal of the slope and the direction of the North, measured Eastwards).

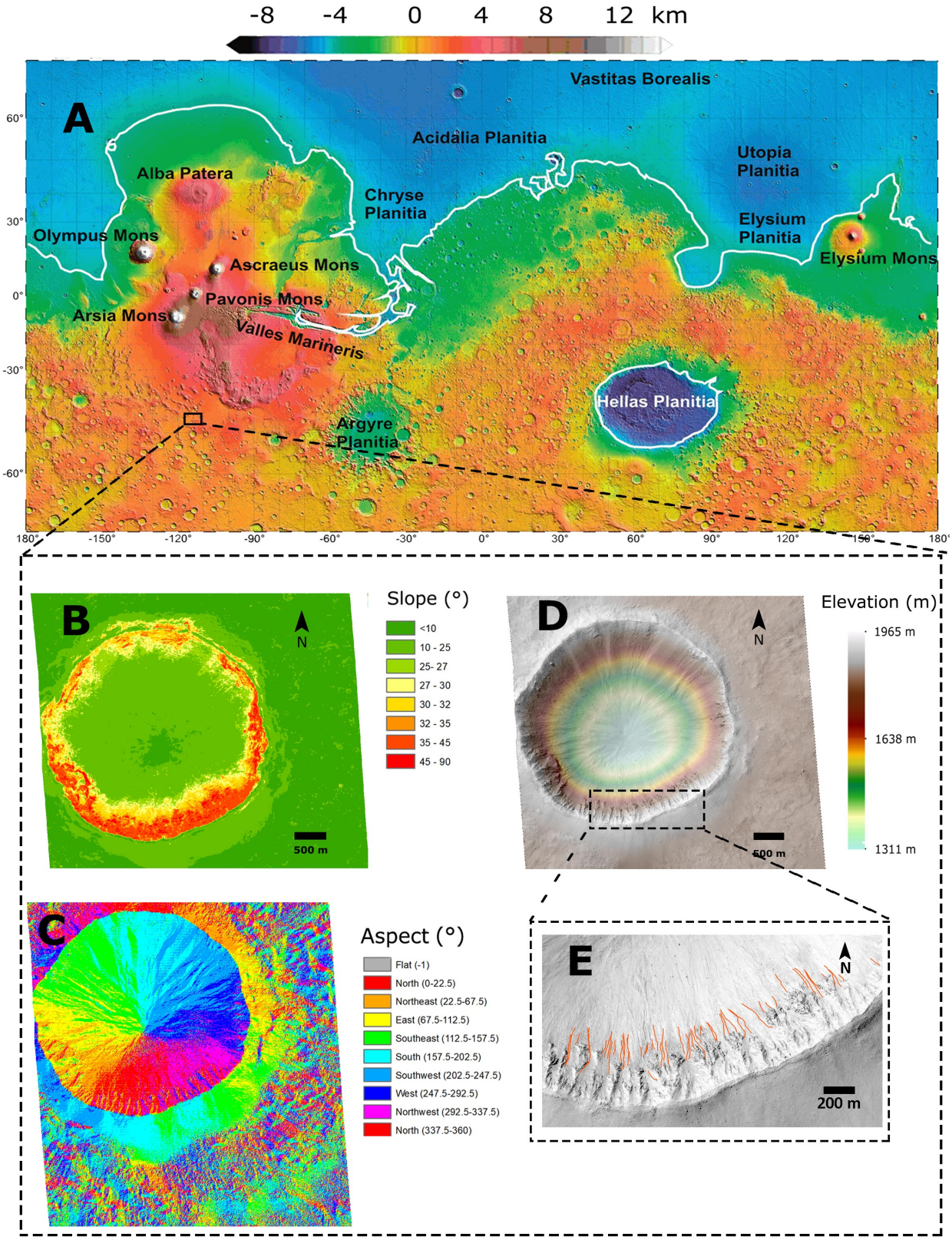

Figure 3.13: A) Colorized MOLA elevation map showing the location of Raga crater (rectangle). B) Slope map. C) Aspect map. D) HiRISE image ESP_023215_1315 of Raga crater overlaid on colorized elevation map from HiRISE DTM DTEEC_014011_1315_014288_1315_A01. E) Zoomed view of dashed rectangle of panel D) with RSL represented by orange lines.

3.2.1 Dataset

Due to the small scale of RSL (0.25-5 m wide and $\approx$ 100 m long) the only useful dataset available to date is the HiRISE catalog (`https://www.uahirise.org/`), in which all HiRISE images and data products are stored. For our investigation, we use repeated images of Raga crater acquired between Mars Year [1] 29 and 31 in the visible wavelengths. Although colour images in the infrared, red and blue part of the electromagnetic spectrum are available, they are not useful for our study since they are restricted only to the central part of the image and do not contain all RSL which we want to analyse. However, different images are acquired with different observational parameters, namely incidence, illumination and phase; as a consequence, the same region is viewed from a different perspective for each image. This problem must be addressed when performing topographic measurements and slope analyses, as in our case, using *orthorectified* images. In such a case, the only factor affecting distance measurements is the cosine of the slope angle. Being this angle invariant between images, measurements made on different orthorectified images are consistent between themselves. In addition to orthorectified imagery, a digital terrain model (DTM) is necessary to measure true distances. A DTM is a dataset which provides the elevation for every point of an image. With HiRISE DTMs it is possible to sample elevation with a spatial scale of 1 m and an uncertainty of approximately 30 cm (Kirk et al., 2008). Moreover, from a DTM it is possible to compute both slope angle and aspect and convert apparent distances in true distances. In our case, all these operations are performed through the the ArcMap® software. In our analysis, we used the following data products:

Product ID	Pixel size (m)	Ls (°)	MY
ESP_014011_1315_RED_A01_ORTHO.JP2	0.25	308.3	29
ESP_014288_1315_RED_A01_ORTHO.JP2	0.25	320.8	29
ESP_020947_1315_RED_A01_ORTHO.JP2	0.25	217.3	30
ESP_021514_1315_RED_A01_ORTHO.JP2	0.25	245.0	30
ESP_021870_1315_RED_A01_ORTHO.JP2	0.25	262.6	30
ESP_022226_1315_RED_A01_ORTHO.JP2	0.25	280.0	30
ESP_022437_1315_RED_A01_ORTHO.JP2	0.25	290.1	30
ESP_023004_1315_RED_A01_ORTHO.JP2	0.25	316.3	30
ESP_023215_1315_RED_A01_ORTHO.JP2	0.25	325.6	30
ESP_023782_1315_RED_A01_ORTHO.JP2	0.25	349.3	30
ESP_023993_1315_RED_A01_ORTHO.JP2	0.25	357.7	30
ESP_024204_1315_RED_A01_ORTHO.JP2	0.25	5.9	31
ESP_029149_1315_RED_A01_ORTHO.JP2	0.25	188.6	31
ESP_030428_1315_RED_A01_ORTHO.JP2	0.25	249.8	31
DTEEC_014011_1315_014288_1315_A01.IMG	1		

Table 3.2: List of orthorectified images used for the analysis. Last row is the DTM we used, which has a pixel size of 1 m. All data products are publicly available at `https://www.uahirise.org/`. MY is the Martian Year.

[1] The Mars Year (MY) is the number of years from the northern Spring equinox of Aprill 11, 1955 (Clancy et al.,2000).

3.2.2 Measurement methods

We here describe how we performed measurements. First, from the DTM we computed slope and aspect of every pixel using the algorithms implemented in the ArcMap® software (Burrough and McDonnell, 1999). These data are shown in figures (3.13B and C). Next, we selected a sample of 50 RSL where we could accurately determine origin, terminus and course. They are shown with orange lines in figure (3.13 E). For each image in table (3.2) we measured the true length (i.e. length draped on the DTM, thus corrected for slope) of all RSL. In particular, lengths were measured by drawing a polygonal chain (or polyline) over each RSL for every image. The built-in function "`Add Surface Information`" was then used to compute the true length of our polylines.

On the contrary, starting and ending elevation, starting and ending slope, and starting aspect of all 50 RSL were measured only on images where RSL achieved their maximum extent using tools provided by the ArcMap® software. This choice is motivated by the facts that a) the starting elevation, slope and aspect of RSL do not change over time and b) the ending elevation and slope are meaningful only when RSL are at their maximum lengths. In particular, from each polyline we obtained its starting and ending vertices using the "`Feature vertices to points`" built-in function. We then use the "`Add surface Information`" tool to extract values of elevation, slope and aspect at locations defined by starting and ending vertices of RSL polylines.

Concerning uncertainties, we assumed an error of 30 cm in elevation given by the uncertainty in the elevation of the DTM and no error in the aspect, as we are interested only in the direction (i.e. North or North-West facing) that the slope is facing and not in the precise azimuth. Regarding lengths, instead, we measured single RSLs multiple times and considered the biggest value between the pixel size, 0.25 m, and the variance of the measurements. For images with completely faded RSL, we assume a length of 0 m and error of 0.25 m. We report our elevation, slope and aspect measurement in table (3.3) and true length measurements in table (3.4); in the latter, we indicate with "L(L_s)" the true length at solar longitude L_s, in meters, and with "MY" the Martian year. A discussion of these measurements is provided in Chapter (4). We show an example of lengths measurements for a RSL of table (3.4) in figures (3.14) and (3.15), and the starting and ending slope distributions in figure (3.16).

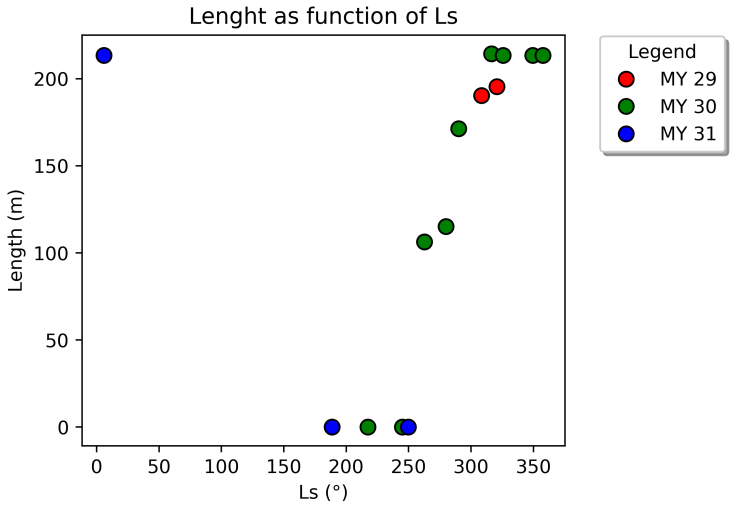

Figure 3.14: Length as a function of L_s of RSL 30 table (3.4).

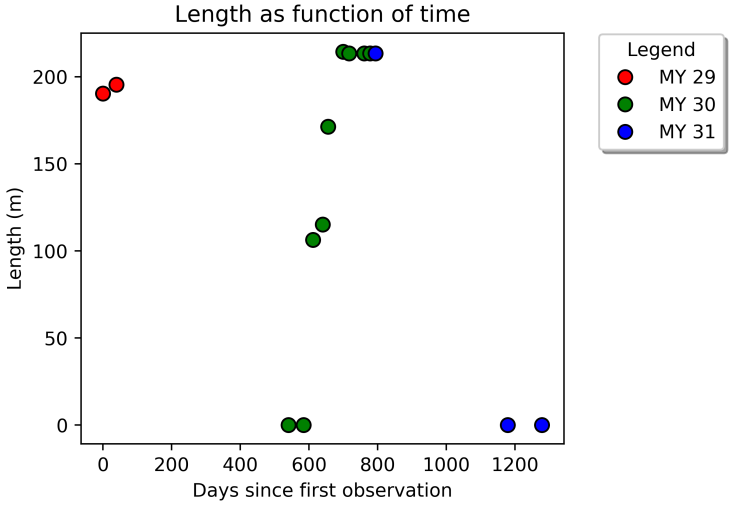

Figure 3.15: Length as a function of time of RSL 30 from table (3.4).

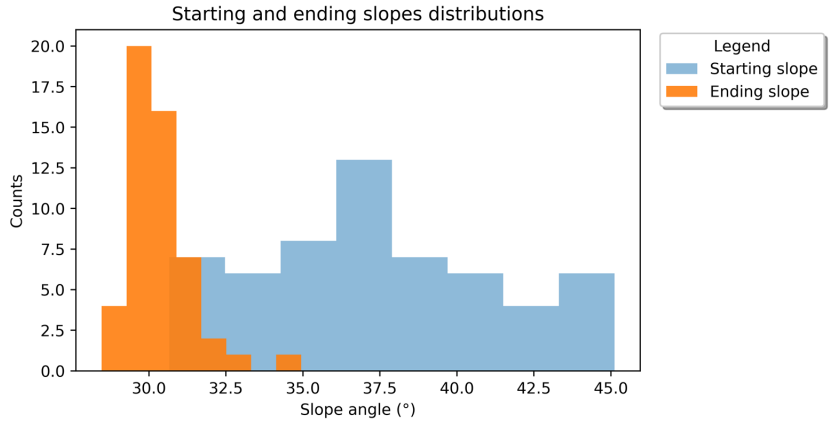

Figure 3.16: Starting and ending slope distributions from table (3.3).

RSL ID	Maximum length (m)	Starting elevation (m)	Ending elevation (m)	Starting slope (°)	Final slope (°)	Aspect (°)
0	216.47±1.97	1739.04±0.30	1630.18±0.30	44.4	30.6	23.4
1	320.27±2.45	1763.66±0.30	1599.98±0.30	37.5	29.4	40.9
3	105.65±1.45	1665.74±0.30	1614.92±0.30	37.9	31.2	22.2
5	285.30±2.29	1753.97±0.30	1608.78±0.30	36.1	31.1	45.9
6	199.82±1.89	1686.16±0.30	1583.13±0.30	33.3	30.9	26.8
7	113.84±1.49	1684.90±0.30	1628.63±0.30	36.5	30.4	39.4
8	262.41±2.18	1770.05±0.30	1632.28±0.30	40.6	29.4	7.9
9	176.76±1.78	1698.27±0.30	1611.70±0.30	32.1	30.7	9.3
10	217.19±1.97	1700.79±0.30	1591.88±0.30	32.0	29.5	17.7
11	174.95±1.77	1714.51±0.30	1624.40±0.30	36.8	29.4	340.1
12	179.68±1.80	1717.25±0.30	1626.62±0.30	37.8	30.7	11.2
13	280.88±2.27	1746.96±0.30	1606.73±0.30	37.2	30.0	29.0
14	299.85±2.36	1750.61±0.30	1597.29±0.30	33.3	29.0	180.5
15	194.05±1.86	1701.06±0.30	1604.42±0.30	36.0	28.5	12.8
16	218.93±1.98	1732.52±0.30	1619.48±0.30	36.4	30.0	28.5
17	77.17±1.32	1694.52±0.30	1656.35±0.30	32.7	31.5	294.4
18	63.25±1.26	1683.10±0.30	1652.75±0.30	31.1	29.6	10.0
19	57.71±1.23	1675.32±0.30	1647.65±0.30	31.0	30.1	326.1
20	57.66±1.23	1663.76±0.30	1636.15±0.30	32.2	29.7	355.5
21	38.80±1.14	1666.06±0.30	1646.12±0.30	35.3	29.5	321.5
22	81.24±1.34	1665.88±0.30	1627.04±0.30	36.4	30.2	326.0
24	212.90±1.95	1680.10±0.30	1573.61±0.30	32.4	29.6	309.7
25	210.70±1.94	1762.24±0.30	1648.31±0.30	38.1	31.7	339.8
26	266.40±2.20	1730.46±0.30	1593.62±0.30	35.3	29.7	340.5
27	209.41±1.94	1756.87±0.30	1643.03±0.30	42.3	32.2	345.2
28	231.11±2.04	1710.83±0.30	1595.70±0.30	34.4	30.0	325.5
29	221.52±1.99	1742.49±0.30	1632.40±0.30	34.1	30.8	339.9
30	213.46±1.95	1735.41±0.30	1628.16±0.30	32.9	30.2	1.8
31	168.99±1.75	1699.62±0.30	1614.20±0.30	41.5	28.7	327.9
33	159.06±1.70	1686.54±0.30	1605.42±0.30	39.7	29.9	303.9
34	75.93±1.31	1653.88±0.30	1609.34±0.30	44.5	31.2	219.7
35	35.76±1.13	1622.91±0.30	1604.31±0.30	39.6	29.0	350.6
36	192.70±1.86	1697.23±0.30	1604.92±0.30	34.6	30.6	17.9
37	194.20±1.86	1690.94±0.30	1601.81±0.30	34.6	32.9	261.5
38	175.51±1.78	1678.15±0.30	1590.71±0.30	36.0	30.2	256.6
39	250.47±2.13	1692.50±0.30	1576.12±0.30	37.4	30.5	341.0
40	192.18±1.85	1685.46±0.30	1587.80±0.30	45.0	29.7	309.3
41	309.58±2.40	1735.09±0.30	1591.61±0.30	37.7	29.9	340.9
42	300.98±2.36	1729.86±0.30	1598.53±0.30	43.5	31.3	303.6
43	378.56±2.72	1763.51±0.30	1601.18±0.30	36.0	30.8	282.4
45	65.44±1.27	1673.80±0.30	1644.15±0.30	38.4	30.2	332.9
46	94.73±1.40	1682.72±0.30	1637.61±0.30	43.8	29.9	16.9
47	194.13±1.86	1663.37±0.30	1568.68±0.30	33.8	30.4	324.0
48	226.60±2.01	1595.12±0.30	1700.75±0.30	30.7	34.9	322.6
49	318.40±2.44	1746.45±0.30	1597.61±0.30	40.9	30.9	346.6
50	294.17±2.33	1768.55±0.30	1628.63±0.30	39.8	30.0	327.0
52	36.32±1.13	1689.26±0.30	1672.98±0.30	45.1	29.6	326.7
53	183.26±1.81	1772.01±0.30	1683.92±0.30	38.4	30.1	312.9
54	209.67±1.94	1757.98±0.30	1657.87±0.30	36.2	30.0	356.5
55	72.68±1.30	1755.30±0.30	1722.66±0.30	39.1	31.0	335.1
56	214.22±107.66	1805.70±0.30	1706.49±0.30	40.3	30.5	345.4

Table 3.3: Measurements of Maximum length, starting and ending elevation, starting and ending slope and aspect.

RSL	L(308.3)	L(320.8)	L(217.3)	L(245.0)	L(262.6)	L(280.0)	L(290.1)	L(316.3)	L(325.6)	L(349.3)	L(357.7)	L(5.9)	L(188.6)	L(249.8)
MY	29	29	30	30	30	30	30	30	30	30	30	31	31	31
0	172.05±1.76	198.22±1.88	0.00±0.25	0.00±0.25	0.00±0.25	146.87±1.64	174.95±1.77	217.74±1.97	216.47±1.97	216.47±1.97	216.47±1.97	216.47±1.97	0.00±0.25	0.00±0.25
1						24.62±1.08	38.66±1.14	316.38±2.43	320.27±2.45	320.27±2.45	320.27±2.45	320.27±2.45	0.00±0.25	0.00±0.25
3						41.96±1.16	83.80±1.35	119.02±1.51	105.65±1.45	105.65±1.45	105.65±1.45	105.65±1.45	0.00±0.25	0.00±0.25
5	273.81±2.23	279.61±2.26	0.00±0.25	0.00±0.25	172.97±1.77	266.29±2.20	283.42±2.28	283.42±2.28	285.30±2.29	285.30±2.29	285.30±2.29	285.30±2.29	0.00±0.25	0.00±0.25
6	170.13±1.75	188.85±1.84	0.00±0.25	0.00±0.25	11.25±1.01	41.39±1.15	167.18±1.74	196.62±1.88	199.82±1.89	199.82±1.89	199.82±1.89	199.82±1.89	0.00±0.25	0.00±0.25
7			0.00±0.25	±	10.54±1.01	87.06±1.37	96.83±1.41	114.87±1.50	113.84±1.49	113.84±1.49	113.84±1.49	113.84±1.49	0.00±0.25	0.00±0.25
8	180.40±1.80	186.18±1.83	0.00±0.25	0.00±0.25	0.00±0.25	38.70±1.14	196.70±1.88	268.22±2.21	262.41±2.18	262.41±2.18	262.41±2.18	262.41±2.18	0.00±0.25	0.00±0.25
9	57.13±1.23	120.31±1.52	0.00±0.25	41.98±1.16	69.71±1.29	120.94±1.52	159.81±1.70	173.55±1.77	176.76±1.78	176.76±1.78	176.76±1.78	176.76±1.78	0.00±0.25	0.00±0.25
10	194.37±1.87	217.19±1.97	0.00±0.25	85.69±1.36	114.45±1.49	174.31±1.77	194.24±1.86	217.45±1.97	217.19±1.97	217.19±1.97	217.19±1.97	217.19±1.97	0.00±0.25	0.00±0.25
11			0.00±0.25	0.00±0.25	0.00±0.25	53.86±1.21	69.95±1.29	119.67±1.52	174.95±1.77	120.28±1.52	120.28±1.52	120.28±1.52	0.00±0.25	0.00±0.25
12	66.95±1.27	138.04±1.60	0.00±0.25	0.00±0.25	40.23±1.15	48.86±1.19	81.10±1.34	181.80±1.81	179.68±1.80	179.68±1.80	179.68±1.80	179.68±1.80	0.00±0.25	0.00±0.25
13	274.64±2.24	274.64±2.24	0.00±0.25	112.63±1.49	187.91±1.84	258.98±2.17	270.49±2.22	281.92±2.27	280.88±2.27	280.88±2.27	280.88±2.27	280.88±2.27	0.00±0.25	0.00±0.25
14	289.57±2.31	298.92±2.35	0.00±0.25	112.57±1.48	153.66±1.68	205.92±1.92	265.47±2.20	299.45±2.35	299.85±2.36	299.85±2.36	299.85±2.36	299.85±2.36	0.00±0.25	0.00±0.25
15	153.58±1.68	172.18±1.76	0.00±0.25	61.67±1.25	76.71±1.32	96.58±1.41	130.97±1.57	193.68±1.86	194.05±1.86	194.05±1.86	194.05±1.86	194.05±1.86	0.00±0.25	0.00±0.25
16	209.46±1.94	217.51±1.97	0.00±0.25	0.00±0.25	104.78±1.45	151.67±1.67	186.73±1.83	221.91±1.99	218.93±1.98	218.93±1.98	218.93±1.98	218.93±1.98	0.00±0.25	0.00±0.25
17						41.73±1.16	53.11±1.21	76.88±1.32	77.17±1.32	77.17±1.32	77.17±1.32	77.17±1.32	0.00±0.25	0.00±0.25
18	24.94±1.08	29.23±1.10	0.00±0.25	0.00±0.25	0.00±0.25	16.11±1.04	21.84±1.06	63.43±1.26	63.25±1.26	63.25±1.26	63.25±1.26	63.25±1.26	0.00±0.25	0.00±0.25
19	75.31±1.31	74.83±1.31	0.00±0.25	0.00±0.25	35.33±1.13	47.92±1.18	53.77±1.21	73.39±1.30	57.71±1.23	57.71±1.23	57.71±1.23	57.71±1.23	0.00±0.25	0.00±0.25
20	37.34±1.14	45.55±1.17	0.00±0.25	0.00±0.25	6.48±0.99	14.64±1.03	20.59±1.06	52.39±1.21	57.66±1.23	57.66±1.23	57.66±1.23	57.66±1.23	0.00±0.25	0.00±0.25
21	38.80±1.14	38.80±1.14	0.00±0.25	0.00±0.25	19.85±1.05	24.51±1.08	34.29±1.12	40.64±1.15	38.80±1.14	38.80±1.14	38.80±1.14	38.80±1.14	0.00±0.25	0.00±0.25
22	36.99±1.13	42.60±1.16	0.00±0.25	0.00±0.25	22.76±1.07	29.97±1.10	45.13±1.17	81.00±1.34	81.24±1.34	81.24±1.34	81.24±1.34	81.24±1.34	0.00±0.25	0.00±0.25
24	187.79±1.83	187.79±1.83	0.00±0.25	0.00±0.25	95.59±1.41	156.96±1.69	190.18±1.85	212.87±1.95	212.90±1.95	212.90±1.95	212.90±1.95	212.90±1.95	0.00±0.25	0.00±0.25
25	78.13±1.32	78.13±1.32	0.00±0.25	0.00±0.25	0.00±0.25	103.29±1.44	122.48±1.53	210.62±1.94	210.70±1.94	210.70±1.94	210.70±1.94	210.70±1.94	0.00±0.25	0.00±0.25
26	216.32±1.97	225.36±2.01	0.00±0.25	0.00±0.25	0.00±0.25	181.20±1.80	230.87±2.03	266.40±2.20	266.40±2.20	266.40±2.20	266.40±2.20	266.40±2.20	0.00±0.25	0.00±0.25
27	73.84±1.30	73.84±1.30	0.00±0.25	0.00±0.25	82.76±1.35	103.26±1.44	140.71±1.62	195.56±1.87	209.41±1.94	209.41±1.94	209.41±1.94	209.41±1.94	0.00±0.25	0.00±0.25
28	196.08±1.87	202.98±1.91	0.00±0.25	0.00±0.25	0.00±0.25	117.51±1.51	203.72±1.91	232.55±2.04	231.11±2.04	231.11±2.04	231.11±2.04	231.11±2.04	0.00±0.25	0.00±0.25
29	123.85±1.54	175.60±1.78	0.00±0.25	0.00±0.25	25.47±1.08	75.78±1.31	161.31±1.71	216.92±1.97	221.52±1.99	221.52±1.99	221.52±1.99	221.52±1.99	0.00±0.25	0.00±0.25
30	190.39±1.85	195.49±1.87	0.00±0.25	0.00±0.25	106.41±1.46	115.25±1.50	171.37±1.76	214.30±1.96	213.46±1.95	213.46±1.95	213.46±1.95	213.46±1.95	0.00±0.25	0.00±0.25
31	145.52±1.64	160.42±1.71	0.00±0.25	0.00±0.25	0.00±0.25	40.71±1.15	58.94±1.24	171.54±1.76	168.99±1.75	168.99±1.75	168.99±1.75	168.99±1.75	0.00±0.25	0.00±0.25
33	159.06±1.70	159.06±1.70	0.00±0.25	0.00±0.25	88.90±1.37	120.06±1.52	139.34±1.61	160.41±1.71	159.06±1.70	159.06±1.70	159.06±1.70	159.06±1.70	0.00±0.25	0.00±0.25
34	75.93±1.31	75.93±1.31	0.00±0.25	0.00±0.25	0.00±0.25	69.97±1.29	70.85±1.29	79.11±1.33	75.93±1.31	75.93±1.31	75.93±1.31	75.93±1.31	0.00±0.25	0.00±0.25
35	35.76±1.13	35.76±1.13	0.00±0.25	0.00±0.25	0.00±0.25	22.59±1.07	27.74±1.09	39.23±1.14	35.76±1.13	35.76±1.13	35.76±1.13	35.76±1.13	0.00±0.25	0.00±0.25
36	159.95±1.71	171.95±1.76	0.00±0.25	0.00±0.25	79.42±1.33	141.07±1.62	169.05±1.75	201.14±1.90	192.70±1.86	192.70±1.86	192.70±1.86	192.70±1.86	0.00±0.25	0.00±0.25
37	156.37±1.69	163.50±1.72	0.00±0.25	68.50±1.28	102.21±1.44	142.84±1.63	163.77±1.72	172.32±1.76	194.20±1.86	175.69±1.78	175.69±1.78	175.69±1.78	0.00±0.25	0.00±0.25
38	172.08±1.76	175.95±1.78	0.00±0.25	72.38±1.30	72.38±1.30	95.36±1.40	117.51±1.51	175.15±1.78	175.51±1.78	175.51±1.78	175.51±1.78	175.51±1.78	0.00±0.25	0.00±0.25
39	250.47±2.13	250.47±2.13	0.00±0.25	0.00±0.25	41.17±1.15	114.00±1.49	187.47±1.83	257.44±2.16	250.47±2.13	250.47±2.13	250.47±2.13	250.47±2.13	0.00±0.25	0.00±0.25
40	192.18±1.85	192.18±1.85	0.00±0.25	95.02±1.40	95.02±1.40	139.87±1.61	172.21±1.76	195.88±1.87	192.18±1.85	192.18±1.85	192.18±1.85	192.18±1.85	0.00±0.25	20.03±1.05
41	309.58±2.40	309.58±2.40	0.00±0.25	230.83±2.03	247.95±2.11	281.79±2.27	301.27±2.36	306.87±2.39	309.58±2.40	309.58±2.40	309.58±2.40	309.58±2.40	0.00±0.25	25.99±1.08
42	279.61±2.26	290.16±2.31	0.00±0.25	124.28±1.54	124.28±1.54	241.24±2.08	296.78±2.34	314.31±2.42	300.98±2.36	300.98±2.36	300.98±2.36	300.98±2.36	0.00±0.25	0.00±0.25
43	337.77±2.53	364.01±2.65	0.00±0.25	254.32±2.14	274.28±2.24	331.04±2.50	339.85±2.54	378.74±2.72	378.56±2.72	378.56±2.72	378.56±2.72	378.56±2.72	0.00±0.25	24.95±1.08
45	81.24±1.34	81.10±1.34	0.00±0.25	0.00±0.25	85.43±1.36	43.28±1.16	70.39±1.29	85.22±1.36	65.44±1.27	83.58±1.35	83.58±1.35	83.58±1.35	0.00±0.25	0.00±0.25
46	65.63±1.27	80.87±1.34	0.00±0.25	42.09±1.16	42.09±1.16	86.77±1.36	92.86±1.39	97.14±1.41	94.73±1.40	94.73±1.40	94.73±1.40	94.73±1.40	0.00±0.25	0.00±0.25
47	36.01±1.13	47.52±1.18	0.00±0.25	0.00±0.25	0.00±0.25	132.17±1.58	154.93±1.68	193.90±1.86	194.13±1.86	194.13±1.86	194.13±1.86	194.13±1.86	0.00±0.25	0.00±0.25
48	159.56±1.70	212.32±1.95	0.00±0.25	52.29±1.20	72.20±1.30	155.05±1.68	220.50±1.99	232.45±2.04	226.60±2.01	226.60±2.01	226.60±2.01	226.60±2.01	0.00±0.25	0.00±0.25
49	299.40±2.35	315.95±2.43	0.00±0.25	179.44±1.80	212.70±1.95	289.07±2.31	316.23±2.43	320.70±2.45	318.40±2.44	318.40±2.44	318.40±2.44	318.40±2.44	0.00±0.25	0.00±0.25
50	244.96±2.10	268.23±2.21	0.00±0.25	213.97±1.96	226.20±2.01	245.82±2.10	267.84±2.21	297.29±2.34	294.17±2.33	294.17±2.33	294.17±2.33	294.17±2.33	0.00±0.25	0.00±0.25
52	33.09±1.12	33.09±1.12	0.00±0.25	0.00±0.25	33.09±1.12	25.29±1.08	25.29±1.08	37.87±1.14	36.32±1.13	36.32±1.13	36.32±1.13	36.32±1.13	0.00±0.25	0.00±0.25
53	93.04±1.39	119.06±1.51	0.00±0.25	92.77±1.39	122.24±1.53	169.73±1.75	182.92±1.81	191.59±1.85	183.26±1.81	183.26±1.81	183.26±1.81	183.26±1.81	0.00±0.25	0.00±0.25
54	103.62±1.44	108.74±1.47	0.00±0.25	151.38±1.67	156.69±1.69	186.77±1.83	198.78±1.89	211.74±1.95	209.67±1.94	209.67±1.94	209.67±1.94	209.67±1.94	0.00±0.25	0.00±0.25
55	58.35±1.23	64.27±1.26	0.00±0.25	25.21±1.08	25.21±1.08	47.67±1.18	70.47±1.29	76.13±1.32	72.68±1.30	72.68±1.30	72.68±1.30	72.68±1.30	0.00±0.25	0.00±0.25
56	53.12±1.21	57.81±1.23	0.00± 0.25	42.42± 1.16	56.45± 1.22	63.63±1.26	74.85±1.31	91.95±1.39	214.22±1.96	107.66±1.46	107.66±1.46	107.66±1.46	0.00±0.25	0.00±0.25

Table 3.4: True length measurements as function of solar longitude, indicated with "L(L_s)", performed on our sample of RSL. All units are meters. Blank spaces indicate that RSL were not visible and were not detected in previous images. From bottom to top, columns are in a temporal sequence.

Chapter 4

Results and discussion

In this Chapter we collect and discuss all results presented in Chapter (3). In the first section, we will discuss the results of our statistical analysis. In the second section we will discuss the measurements of RSL in Raga crater in the light of current proposed hypotheses concerning the nature of RSL.

4.1 Global properties of RSL

In section 3.1 we studied the fundamental properties of the Martian surface at all the identified RSL sites, exploiting our up to date catalogue of both candidate and confirmed RSL. The resulting distributions are presented in figures (3.6, 3.7,3.8,3.9,3.10,3.11) and summarized here in table (4.1):

	H	S	TI_d	TI_n	K	A	DCI	WEH
min	-5002	0.0	52	171	2.0	0.092	0.953	3
25%	-2462	3.9	176	235	7.0	0.133	0.969	4
50%	-126	9.1	223	272	11.0	0.139	0.973	5
75%	861	19.7	268	332	13.0	0.154	0.977	7
max	5088	36.7	469	477	25.0	0.236	0.990	22

Table 4.1: Ranges, central tendencies and variabilities of all global variables present in the catalogue for confirmed RSL. H is the MOLA elevation, in metres, S is the slope, TI_d and TI_n are daytime and nigh-time thermal inertia, respectively, in thermal inertia units (TIU). *K* is the rock abundance. A is the albedo. DCI is the dust cover index. WEH is the water equivalent hydrogen mass fraction (% wt). All variables are defined in section (3.1).

In particular, from figure (3.7 A) we see that confirmed RSL are found in regions with a night-time inertia between 171 and 474 TIU, with a median thermal inertia of 272 TIU for confirmed RSL sites. In particular, most RSL occur on regions with a thermal inertia higher than 150 TIU. Since this values marks the thermophysical limit for dusty surfaces, these regions have a low dust content. Moreover from figures (3.7 B and D) it is clear that thermal inertia distributions for VM RSL and SML RSL are different, as they have a median of 363 and 244 TIU, respectively. This

difference is unlikely due to dust, since from figures (3.9B and D) we do not observe significant differences on the dust cover index, but it probably means that VM RSL form on slightly more "rocky" terrains than SML RSL. Instead, more data are needed to assess the thermophysical properties of EQ and CAP RSL. The same conclusions can be drawn from the analysis of daytime thermal inertia distributions. However, as indicated by Edwards and Piqueux (2016) night-time data is preferable as the effects of topography are reduced .

Analogue results emerge from the analysis of the dust cover index distributions, depicted in figure (3.9). Confirmed RSL have a median DCI of 0.974, meaning that they generally do not occur in dusty surfaces, consistently with what derived from the thermal inertia distributions. Moreover, candidate sites seems to follow the same distribution as confirmed ones. As pointed out above, there are no significant differences in DCI for VM, SML, EQ and CAP RSL. The fact that RSL do not generally occur in dusty surface implies than they appearance is not due to the removal of surficial dust, which leaves exposed the underlying regolith, as for dark slope streaks. In the same way, their fading is probably not due to dust deposition processes, posing a still unresolved problem for granular flow processes.

Concerning rock abundance, whose distributions are shown in figure (3.8), confirmed RSL are located in regions with a median rock abundance of 11%. However, this is most likely due to the high number of VM RSL, which have a median of 12% rock abundance, with respect to the others. Most SML RSL are outside the extent of the Viking IRTM rock abundance map, as we can see see from figure (3.3). Instead, more sites are needed to better characterize the distributions for EQ and CAP RSL. This will likely be possible in the near future, as more HiRISE observation of RSL sites will be performed.

Concerning albedo, from figure (3.10) we can conclude that RSL occur in low albedo regions, even tough a tail at high albedo is present. No significant differences between different RSL are present, although equatorial sites may have a high albedo tail. However, due to the low number of candidate and EQ RSL, more sites need to be discovered in order to assess if it is statistically significant.

To conclude our results on RSL global properties, we discuss their water content, estimated from the large scale distribution of water equivalent hydrogen. Globally, RSL sites have a low 5% median water equivalent hydrogen, which is more consistent with a dry hypothesis as the possible origin of RSL. In fact, if RSL were due to the melting of surficial ice, we would expect them to be more concentrated on high water equivalent hydrogen terrains. However, the distributions of water equivalent hydrogen are indicative only of the presence of ice in the uppermost 1.5 metres of the surface and at a resolution of 300 km, which is three order of magnitudes greater than typical RSL scales. Therefore, they do not rule out a correlation between RSL sites and subsurficial ice either deeper than

1.5 m or distributed on much smaller scale than the resolution. In such cases, a wet-dominated origin is still plausible as the nature of RSL. Such a hypothesis has been suggested by (Stillman et al.,2016).

4.2 RSL in Raga crater

We now discuss the analysis of RSL in Raga crater. Our true length measurements shows that RSL lengths ranges from approximately 30 m to 300 m. By analysing their temporal dependence we find that activity starts not later than $L_s = 262$ with a phase of incremental lengthening that ends no later than $L_s = 325.6$. After that, RSL remain dark until not earlier than $L_s = 5.9$ and fade not later than $L_s = 188.6$. This activity takes place in southern summer, when temperatures can be higher than the freezing point of water and brines and allow their melting. These temporal dependencies are illustrated in figures (3.14) and (3.15). This result suggests that a volatile may be involved in the process, although the assessments of its role is still not clear and deserves further investigation.

On the contrary, the analysis of slope and aspects favours a dry dominated phenomenon. In figure (3.16) we plot the distributions of starting and ending slopes of our sample of RSL. While RSL forms on any slope from 30° to 45°, they end at a very well-constrained median slope of $30.15^\circ\ ^{+0.68}_{-0.47}$, where we computed errors as distances of the mean from the 25-th and 75-th percentile. This value is within the range of slope angles for which granular flows terminate, the so-called *dynamic angle of repose* (Atwood-Stone and McEwen, 2013) and consistent with what measured by (Dundas et al., 2017) in several RSL sites, including Raga crater. However, (Dundas et al.,2017) measured 15 RSL in Raga crater while we analysed 50.

Concerning the dependence of the slope angle from length, our results are consistent with those of Dundas et al. (2018): as emerges from figure (4.1), when the slope is near the *dynamic angle of repose*, all RSL stop regardless of their length. This behaviour is consistent with a dry granular flow origin for RSL, as suggested by Dundas et al. (2017). Instead, for wet-dominated models we would not expect such a well constrained slope distribution; on the contrary, ending slopes would be controlled by the amount of melted ice: as more ice melts, more time is needed for evaporation to balance the water input and RSL can propagate longer downhill to lower slopes (see figure 3.13 D). Instead, where there is less ice, evaporation balances the water input earlier, RSL are shorter and slopes are higher. Finally, wet flows are expected to propagate also on less steep slopes than 30° (Dundas et al.,2017).

The analysis of the dependence of RSL maximum length from aspect, discussed here for the first time, showed no significant trends. As it is clear from figure (4.2), RSL maximum lengths seems not to be significantly influenced by difference in the terrain orientation, which translate in a difference in temperature. However, this site is not optimal for this

kind of study, as RSL forms on only two main aspects. The full orientation dependence is thus precluded here. Further investigations on sites having RSL on different terrain orientations are thus needed to assess if this dependence may be lower than what can be appreciated in this sites but still present, or there is no dependence at all. In the latter case, volatiles would have a very limited role in RSL.

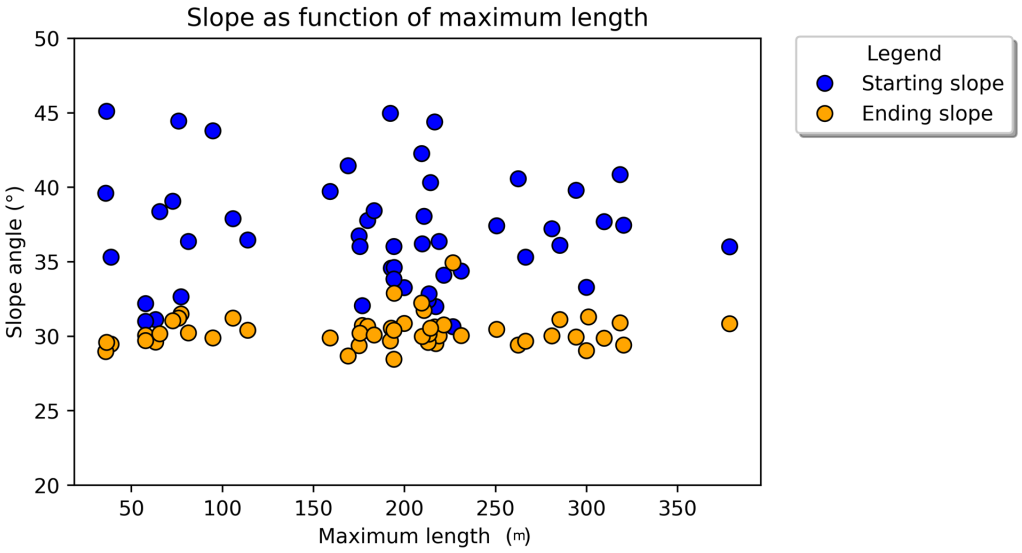

Figure 4.1: Dependency of the slope angle from the maximum RSL length.

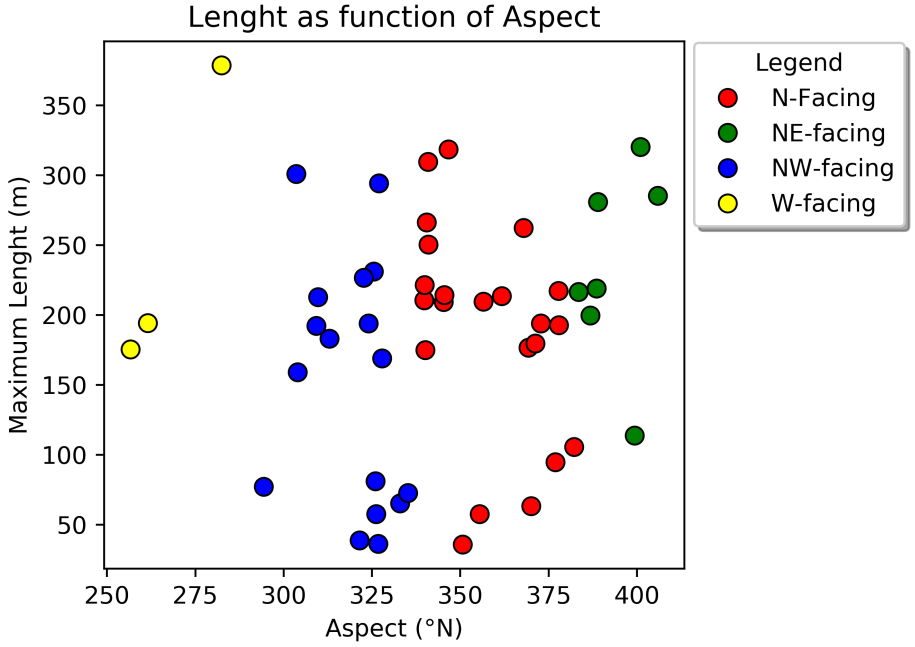

Figure 4.2: Dependency of the maximum length from the aspect. Here we added 360° to aspects from 0 to 40 in order to better illustrate them.

Chapter 5

Conclusions

In this thesis we performed a comprehensive study of recurring slope lineae (RSL) on the Martian surface. This study is composed of two parts: the first is a statistical analysis of properties of the Martian surface at RSL sites, whose aim is to provide a more extensive and complete characterization of RSL than what is present in literature. To do so, we collected all candidate and confirmed RSL sites discovered up to now and produced an update catalogue, which is reported in Appendix (A). In the catalogue, we present values of MOLA elevation, slope, thermal inertia, rock abundance, dust cover index, albedo and water equivalent hydrogen for all candidate and confirmed RSL sites. Their distributions are shown in section (3.1) and allowed us to conclude that: a) RSL do not occur on dusty surfaces and b) the water content of the surface at RSL sites is low. However, the water equivalent hydrogen of RSL sites is sampled at a very large scale of 300 km and it is indicative only of the uppermost 1.5 m of the surface. As a consequence, a wet-dominated origin for RSL is not completely ruled out.

The catalogue allowed us to find regions of the Martian surface having analogue global properties to RSL. These regions are of particular interest since they are potential new RSL sites, to be investigated with present and future missions.

Finally, we performed a detailed study of key properties of RSL in Raga crater. In particular, RSL activity occurs during southern summer, when temperatures rise over the freezing point of water ice or brines. Although this aspect may suggest a role for a volatile in triggering RSL, since no dry granular flow show this type of behaviour, our slope measurements strongly suggest that RSL are consistent with dry granular flows with a limited role for volatiles. In fact, the slope angles of all 50 RSL we measured in Raga crater lies in the range 28°-35°, which is the range of the *dynamical angle of repose* for dry granular flows. In particular, we measure a median slope of $30.15^{\circ}\ ^{+0.68}_{-0.47}$, which is consistent with that measured by Dundas et al. (2017) for several RSL sites, including Raga crater. In addition, we studied for the first time the correlation between RSL maximum length and the slope orientation but we didn't find any trend, which would be expected for wet-dominated processes. As more illuminated slopes have higher temperatures, we would expect longer RSL if they were due to the melting of ice. However it must be noted that a complete

set of orientations was not available at Raga crater, and this could hide a possible weak dependence. Further investigation are needed to draw more definitive conclusions.

Chapter 6

Future prospects

The work performed in this thesis can be extended by further exploring the dependence between the RSL lengths and the aspect in sites where RSL occur on all orientations.

Useful informations will be provided by the Colour and Stereo Surface Imaging System (CaSSIS, Thomas et al.,2017) on board the ESA's ExoMars Trace Gas Orbiter (TGO) mission. The CaSSIS stereo camera provides images at a spatial scale of 4.6 m/px in four bands from the near infrared to the blue part of the visible electromagnetic spectrum.

The Padova group shares the co-responsibility of the instrument and is responsible for the production and storage of digital terrain models obtained from CaSSIS stereo pairs. In this context we plan to perform observations of RSL with the CaSSIS stereo camera, which may provide extremely useful informations concerning the origin and the development RSL. Despite having a lower resolution than HiRISE, bigger RSL, like those observed in Horowitz crater, can be identified (Tornabene et al.,2018) and their length can be measured, although with a bigger uncertainty than with HiRISE images. In addition, from CaSSIS digital terrain models it is possible to derive both slope and aspect. Moreover, since the MRO is in a sun-synchronous orbit, HiRISE observations can be performed only near 3 PM of local time, i.e. during the afternoon. As a consequence, the temporal variability of RSL can be studied only on timesecales longer than one day. On the contrary, the circular orbit of TGO allows CaSSIS observations to be performed at different local times. As a consequence, RSL can be observed in the morning with CaSSIS and in the afternoon with HiRISE. Such observations will be of crucial importance because they can characterise RSL activity on a diurnal time scale, thus providing pivotal informations directly linked to their formation mechanism. Indeed, if RSL are originated by the melting of either ice or brines, their activity is expected to be more enhanced during midday than during afternoon, due to the hotter temperatures. On the contrary, no changes are expected for dry granular flows.

Appendix A

We here report all our RSL catalogue with global variables defined and described in (3.1). For elevation (H) we assume an error of 3 m (Smith et al.,2001).

Region	Status	Lat	Lon	H	S	TI_d	TI_n	RA	DCI	A	WEH
VM	1	-15.49	308.53	-3327	22	268±16	472±28	11±2	0.141	0.9704	5
VM	1	-15.40	309.54	-1333	23	192±11	402±24	19±3	0.123	0.9702	5
VM	1	-14.70	304.30	-3622	20	52±3	345±20	6±1	0.115	0.9607	5
VM	1	-14.60	302.40	-1924	25	325±19	427±25	1±1	0.121	0.9704	5
VM	1	-14.40	304.60	-1487	28	469±28	365±21	6±1	0.112	0.9704	5
VM	1	-14.30	303.80	-2902	12	379±22	418±25	13±2	0.119	0.9602	5
VM	1	-14.10	269.90	5088	0	180±10	197±11	13±2	0.229	0.953	5
VM	1	-13.17	290.66	40	36	321±19	455±27	13±2	0.136	0.970	8
VM	1	-13.14	312.45	-2462	4	246±14	247±14	12±2	0.127	0.9607	6
VM	1	-13.10	290.90	-904	21	347±20	477±28	13±2	0.139	0.9702	8
VM	1	-13.10	295.20	1942	11	263±15	343±20	15±3	0.134	0.9706	7
VM	1	-13.08	294.40	3404	10	268±16	338±20	12±2	0.134	0.9708	7
VM	1	-13.00	294.50	2001	18	287±17	243±14	12±2	0.134	0.9802	7
VM	1	-13.00	295.40	1125	22	435±26	446±26	15±3	0.131	0.9707	7
VM	1	-12.99	295.28	203	30	281±16	451±27	13±2	0.137	0.980	7
VM	1	-12.99	294.54	1060	17	288±17	304±18	12±2	0.136	0.9801	7
VM	1	-12.90	293.40	470	33	219±13	429±25	16±3	0.136	0.9701	8
VM	1	-12.90	295.50	-1324	19	300±18	382±22	13±2	0.134	0.9803	7
VM	1	-12.68	313.85	-1974	12	175±10	325±19	6±1	0.127	0.9703	7
VM	1	-12.60	294.70	-2081	25	335±20	470±28	12±2	0.135	0.980	7
VM	1	-11.60	284.90	-794	15	286±17	356±21	14±2	0.117	0.9801	7
VM	1	-11.60	285.10	253	19	254±15	305±18	17±3	0.12	0.9706	7
VM	1	-11.50	290.30	-5002	4	192±11	327±19	17±3	0.153	0.959	8
VM	1	-11.50	291.60	-4067	9	223±13	378±22	7±1	0.154	0.9607	8
VM	1	-11.48	291.58	-4039	8	234±14	358±21	7±1	0.157	0.960	8
VM	1	-11.20	284.90	-1209	1	197±11	277±16	14±2	0.141	0.9702	7
VM	1	-10.90	290.20	-4791	3	261±15	376±22	1±1	0.155	0.9702	8
VM	1	-9.32	313.68	-979	24	276±16	362±21	1±1	0.131	0.9706	8
VM	1	-8.80	304.80	898	5	225±13	336±20	14±2	0.129	0.9708	7
VM	1	-7.64	311.89	-2640	16	242±14	294±17	8±1	0.13	0.9703	8
VM	1	-6.80	298.00	-1109	4	306±18	257±15	8±1	0.175	0.991	6
VM	1	-4.70	298.60	-4011	8	109±6	222±13	7±1	0.163	0.956	6
VM	1	-4.67	298.58	-3920	4	160±9	182±10	7±1	0.163	0.959	6
VM	1	-1.44	284.38	-2445	24	229±13	241±14	5±1	0.153	0.9705	6
SML	1	-52.96	234.69	2097	1	228±13	256±15		0.15	0.9704	22
SML	1	-52.34	157.75	646	20	185±11	254±15		0.16	0.9709	5
SML	1	-48.61	223.75	2061	1	224±13	274±16		0.152	0.9604	4
SML	1	-48.12	242.43	1758	0	205±12	237±14		0.143	0.9705	8
SML	1	-47.72	4.61	805	31	245±14	241±14		0.147	0.9605	3
SML	1	-47.42	37.65	375	11	266±15	272±16		0.166	0.970	3
SML	1	-47.05	18.78	1216	6	221±13	324±19		0.109	0.9802	3
SML	1	-46.90	5.10	14	19	210±12	278±16		0.133	0.9701	3
SML	1	-46.00	45.76	-2035	2	262±15	247±14		0.182	0.9607	4
SML	1	-45.94	9.54	1589	9	201±12	224±13		0.164	0.99	3

SML	1	-45.09	269.42	2665	3	172±10	214±12		0.153	0.9705	3
SML	1	-43.82	34.15	-243	13	224±13	271±16		0.093	0.9704	4
SML	1	-43.70	229.07	2354	6	173±10	182±10		0.173	0.9609	4
SML	1	-43.31	343.24	-1085	1	134±8	247±14		0.167	0.9702	3
SML	1	-43.06	232.10	1829	11	128±7	180±10		0.173	0.980	5
SML	1	-42.66	336.18	613	1	281±16	236±14	9±1	0.168	0.9702	3
SML	1	-42.33	201.83	283	24	188±11	311±18		0.15	0.9705	4
SML	1	-42.04	228.03	2249	6	154±9	197±11		0.168	0.9609	4
SML	1	-41.73	150.60	429	4	279±16	249±14		0.149	0.9607	4
SML	1	-41.60	202.30	-52	13	140±8	214±12		0.118	0.9702	4
SML	1	-41.15	187.38	593	2	223±13	208±12		0.139	0.9801	5
SML	1	-40.36	225.84	1671	3	185±11	217±13	9±1	0.147	0.970	4
SML	1	-39.67	123.11	37	4	148±8	171±10		0.187	0.9601	3
SML	1	-39.65	88.09	-4873	10	242±14	273±16		0.172	0.957	7
SML	1	-39.30	111.22	59	1	176±10	230±13		0.228	0.9702	3
SML	1	-39.00	223.70	2052	3	90±5	185±11	7±1	0.15	0.9707	4
SML	1	-38.80	159.50	385	11	260±15	328±19		0.139	0.9703	5
SML	1	-38.22	183.96	495	12	249±14	255±15	11±2	0.127	0.9801	5
SML	1	-38.17	223.99	816	7	133±7	195±11	7±1	0.141	0.9701	4
SML	1	-38.17	188.85	-126	1	178±10	203±12	5±1	0.134	0.9605	5
SML	1	-37.69	192.97	861	8	175±10	311±18	4±1	0.132	0.9706	5
SML	1	-37.40	229.00	2290	8	143±8	201±12	6±1	0.145	0.9703	6
SML	1	-37.16	190.83	29	8	244±14	251±15		0.121	0.9707	5
SML	1	-37.09	192.04	110	16	155±9	206±12	4±1	0.132	0.9702	5
SML	1	-35.68	323.48	-1388	7	163±9	264±15	6±1	0.136	0.9704	4
SML	1	-35.00	300.94	2356	1	216±12	256±15	12±2	0.131	0.9708	5
SML	1	-32.40	41.15	103	14	134±8	296±17		0.188	0.9607	6
SML	1	-32.33	338.21	341	5	138±8	222±13	14±2	0.136	0.9705	6
SML	1	-32.05	140.78	-585	3	106±6	224±13		0.152	0.9705	3
SML	1	-31.44	50.71	-1085	1	288±17	281±16		0.158	0.9609	5
EQ	1	-12.25	74.08	-195	9	205±12	252±15	7±1	0.126	0.9706	6
EQ	1	-11.73	122.97	1777	21	153±9	266±15	1±1	0.134	0.9705	4
EQ	1	-7.80	86.01	1589	5	218±13	233±13	13±2	0.125	0.9605	5
EQ	1	-3.51	356.25	-1594	0	208±12	273±16	8±1	0.132	0.9701	17
EQ	1	2.18	351.02	-2508	5	200±12	227±13	25±5	0.236	0.9608	3
CAP	1	31.67	320.66	-3911	4	267±16	335±20	8±1	0.136	0.9707	6
CAP	1	34.64	326.42	-4067	0	166±9	268±16	17±3	0.137	0.9707	6
CAP	1	34.81	318.61	-4271	9	293±17	327±19	11±2	0.146	0.9702	5
CAP	1	35.26	327.93	-4192	2	206±12	237±14	8±1	0.137	0.9609	6
CAP	1	35.83	323.89	-3971	3	164±9	251±15	8±1	0.144	0.9803	5
CAP	1	37.21	320.44	-3904	27	210±12	245±14	12±2	0.144	0.9702	6
CAP	1	38.36	324.98	-4106	2	234±14	268±16	19±3	0.136	0.9607	6
CAP	1	42.16	312.21	-4043	8	228±13	310±18	23±4	0.156	0.9709	7
VM	0	-16.95	313.38	-3320	7	196±11	270±16	13±2	0.13	0.9609	5
VM	0	-16.31	310.19	-2491	20	198±11	342±20	6±1	0.135	0.9608	5
VM	0	-16.00	296.00	2906	7	439±26	401±24	1±1	0.15	0.9801	7
VM	0	-15.75	313.19	-2306	17	208±12	243±14	2±1	0.135	0.9703	6
VM	0	-15.58	309.27	-1090	21	239±14	210±12	19±3	0.125	0.970	5
VM	0	-15.46	309.36	-1531	21	475±28	357±21	19±3	0.123	0.9609	5
VM	0	-14.71	309.46	-3771	19	201±12	350±21	11±2	0.129	0.9601	5
VM	0	-14.52	305.83	-1596	35	332±19	484±29	9±1	0.115	0.9706	5
VM	0	-14.43	311.51	-2916	4	211±12	304±18	4±1	0.131	0.9703	6
VM	0	-14.35	304.01	1144	26	411±24	477±28	6±1	0.117	0.970	5
VM	0	-13.93	300.02	-85	31	631±37	327±19	12±2	0.128	0.9702	6
VM	0	-13.90	299.86	-795	24	470±28	397±23	8±1	0.135	0.9606	6
VM	0	-13.83	309.64	-3156	22	168±10	255±15	14±2	0.139	0.9605	6
VM	0	-13.68	315.75	-2747	11	166±9	277±16	9±1	0.142	0.9606	7
VM	0	-13.59	289.76	-1472	15	256±15	395±23	11±2	0.135	0.9707	8
VM	0	-13.54	298.10	26	30	553±33	395±23	16±3	0.119	0.9707	6
VM	0	-13.50	293.30	-829	12	322±19	475±28	2±1	0.142	0.9706	8
VM	0	-13.37	311.44	-1857	13	229±13	271±16	6±1	0.137	0.970	6

VM	0	-13.30	312.55	-761	15	207±12	224±13	12±2	0.131	0.9701	6
VM	0	-13.30	296.10	1794	21	330±19	380±22	13±2	0.131	0.991	7
VM	0	-13.23	314.68	-3213	9	264±15	374±22	6±1	0.127	0.9607	7
VM	0	-13.18	312.18	-2455	20	216±12	386±23	12±2	0.126	0.9703	6
VM	0	-13.15	295.07	2882	23	273±16	401±24	15±3	0.133	0.9703	7
VM	0	-13.06	290.56	-3306	7	208±12	460±27	13±2	0.129	0.9801	8
VM	0	-13.02	289.07	-2465	19	297±17	405±24	11±2	0.122	0.970	8
VM	0	-12.88	310.45	-2712	13	248±14	273±16	1±1	0.143	0.9609	6
VM	0	-12.87	288.83	-1307	3	261±15	294±17	8±1	0.126	0.9806	8
VM	0	-12.84	312.44	-564	14	190±11	298±17	9±1	0.129	0.9704	6
VM	0	-12.80	294.20	-229	15	344±20	369±22	12±2	0.134	0.9701	7
VM	0	-12.74	313.68	-1526	18	248±14	296±17	6±1	0.132	0.9703	7
VM	0	-12.68	313.99	-2015	8	191±11	274±16	6±1	0.129	0.970	7
VM	0	-12.67	312.74	-1574	15	110±6	296±17	9±1	0.145	0.9604	7
VM	0	-12.66	294.85	106	22	406±24	384±23	12±2	0.135	0.9708	7
VM	0	-12.60	312.79	-2706	15	170±10	271±16	9±1	0.126	0.9602	7
VM	0	-12.60	313.73	-2032	21	191±11	269±16	6±1	0.129	0.9706	7
VM	0	-12.54	290.33	-2806	12	343±20	411±24	25±5	0.161	0.9607	8
VM	0	-12.50	290.20	-2948	11	298±17	409±24	25±5	0.161	0.9701	8
VM	0	-12.44	289.54	-1014	12	287±17	337±20	14±2	0.139	0.9603	8
VM	0	-12.44	287.88	-1262	21	290±17	336±20	9±1	0.13	0.9801	8
VM	0	-12.42	289.64	-1198	18	237±14	373±22	14±2	0.144	0.9605	8
VM	0	-12.37	290.88	-2424	15	251±15	252±15	25±5	0.154	0.9609	8
VM	0	-12.20	291.05	-2051	29	99±5	302±18	11±2	0.158	0.9606	8
VM	0	-12.20	291.10	-2524	30	125±7	255±15	11±2	0.158	0.9605	8
VM	0	-12.19	288.26	-165	8	174±10	242±14	8±1	0.132	0.960	8
VM	0	-12.17	287.04	1390	15	206±12	288±17	9±1	0.141	0.9609	8
VM	0	-12.13	292.30	-3263	13	208±12	408±24	25±5	0.146	0.9603	8
VM	0	-12.04	291.59	-2668	24	248±14	452±27	11±2	0.159	0.9701	8
VM	0	-11.74	285.36	191	16	316±18	312±18	17±3	0.133	0.9706	7
VM	0	-11.50	285.40	-1607	2	233±13	327±19	17±3	0.149	0.9703	7
VM	0	-11.40	290.80	-3669	18	515±30	327±19	17±3	0.152	0.952	8
VM	0	-11.26	284.91	-1275	4	226±13	287±17	14±2	0.135	0.9803	7
VM	0	-11.06	289.24	-4068	9	140±8	264±15	9±1	0.162	0.956	9
VM	0	-10.99	290.26	-4819	1	325±19	471±28	1±1	0.157	0.970	8
VM	0	-10.980	284.85	-575	18	245±14	285±17	12±2	0.157	0.9802	7
VM	0	-10.41	285.02	-1414	11	202±12	266±15	13±2	0.173	0.9606	7
VM	0	-10.32	285.01	-1948	14	227±13	255±15	13±2	0.18	0.9606	7
VM	0	-10.29	291.15	631	9	263±15	283±16	1±1	0.213	0.9607	8
VM	0	-10.28	286.27	-899	22	402±24	336±20	1±1	0.172	0.9607	8
VM	0	-10.19	285.11	140	18	220±13	228±13	13±2	0.176	0.9806	7
VM	0	-9.80	285.50	-1651	15	164±9	380±22	12±2	0.155	0.9605	8
VM	0	-9.77	284.38	-1273	22	172±10	218±13	11±2	0.137	0.9705	7
VM	0	-9.73	284.11	-780	7	248±14	301±18	11±2	0.144	0.9609	7
VM	0	-9.62	283.75	-1364	21	332±19	331±19	13±2	0.156	0.9705	7
VM	0	-9.53	283.24	-998	2	271±16	300±18	13±2	0.143	0.9605	7
VM	0	-9.41	281.58	3039	36	331±19	342±20	9±1	0.162	0.9703	6
VM	0	-9.39	283.13	360	22	213±12	365±21	13±2	0.157	0.970	7
VM	0	-9.33	282.65	-1038	19	256±15	350±21	11±2	0.166	0.9701	7
VM	0	-9.33	281.90	-1057	9	300±18	390±23	9±1	0.154	0.9802	6
VM	0	-9.28	288.82	-2761	5	221±13	382±22	13±2	0.173	0.970	9
VM	0	-9.09	281.78	-1570	27	190±11	376±22	9±1	0.133	0.9604	6
VM	0	-8.91	294.94	1365	28	294±17	250±15	9±1	0.258	0.9804	6
VM	0	-8.91	314.91	1350	3	270±16	257±15	14±2	0.128	0.9609	8
VM	0	-8.84	281.04	-2466	24	213±12	320±19	1±1	0.16	0.9702	6
VM	0	-8.84	315.03	718	32	308±18	470±28	2±1	0.141	0.9704	8
VM	0	-8.83	280.80	-2057	20	155±9	429±25	13±2	0.167	0.9708	6
VM	0	-8.80	304.90	788	0	275±16	246±14	14±2	0.127	0.9803	7
VM	0	-8.77	275.35	4124	4	189±11	296±17	16±3	0.189	0.9601	5
VM	0	-8.73	294.50	1675	25	233±13	313±18	9±1	0.209	0.9701	6
VM	0	-8.70	295.55	1632	24	156±9	200±12	1±1	0.252	0.9604	6

VM	0	-8.68	315.39	-2560	19	263±15	373±22	2±1	0.149	0.9703	8
VM	0	-8.64	276.23	4192	19	163±9	160±9	15±3	0.188	0.9601	5
VM	0	-8.58	283.36	-3082	2	107±6	161±9	1±1	0.167	0.9601	7
VM	0	-8.58	314.00	-3684	0	263±15	324±19	14±2	0.132	0.9706	8
VM	0	-8.54	294.25	2155	16	243±14	213±12	9±1	0.199	0.956	6
VM	0	-8.35	313.27	-3292	18	330±19	437±26	1±1	0.126	0.9601	8
VM	0	-8.28	277.63	1857	13	184±11	221±13	16±3	0.154	0.9605	5
VM	0	-8.21	276.26	4061	16	246±14	337±20	15±3	0.156	0.9602	5
VM	0	-8.20	294.67	2034	15	238±14	161±9	9±1	0.23	0.9605	6
VM	0	-8.14	278.05	-1701	26	180±10	421±25	12±2	0.158	0.9703	5
VM	0	-8.13	275.21	4247	2	192±11	279±16	16±3	0.15	0.9703	5
VM	0	-8.11	275.31	3888	8	138±8	210±12	16±3	0.145	0.9702	5
VM	0	-8.10	275.01	4265	11	280±16	209±12	16±3	0.145	0.9802	5
VM	0	-7.97	276.76	-339	14	145±8	289±17	13±2	0.178	0.959	5
VM	0	-7.96	282.82	-2802	6	202±12	306±18	12±2	0.124	0.9609	7
VM	0	-7.92	275.89	3836	19	281±16	396±23	15±3	0.141	0.9709	5
VM	0	-7.86	278.26	-2183	22	163±9	423±25	9±1	0.187	0.9701	6
VM	0	-7.85	284.19	-583	19	130±7	357±21	5±1	0.15	0.9703	7
VM	0	-7.85	284.32	-1186	8	208±12	362±21	5±1	0.147	0.9705	7
VM	0	-7.84	295.38	-1535	24	160±9	264±15	1±1	0.302	0.9701	6
VM	0	-7.84	278.03	-2426	23	178±10	486±29	9±1	0.157	0.9701	6
VM	0	-7.82	295.44	-741	25	98±5	244±14	1±1	0.302	0.9606	6
VM	0	-7.70	267.14	169	21	224±13	200±12	1±1	0.119	0.9609	5
VM	0	-7.69	307.65	-984	28	313±18	353±21	16±3	0.129	0.9802	8
VM	0	-7.47	312.86	-3621	8	223±13	297±17	1±1	0.133	0.9703	8
VM	0	-7.41	310.47	-1242	16	288±17	491±29	9±1	0.14	0.9609	8
VM	0	-7.34	277.17	-1226	24	277±16	439±26	11±2	0.192	0.9607	5
VM	0	-7.31	276.90	-2123	27	186±11	318±19	13±2	0.214	0.9604	5
VM	0	-7.25	311.21	-654	25	277±16	467±28	8±1	0.177	0.9706	8
VM	0	-7.21	274.51	831	24	345±20	268±16	15±3	0.127	0.9701	5
VM	0	-7.19	288.82	73	8	268±16	274±16	8±1	0.174	0.958	8
VM	0	-7.19	275.52	-2317	19	258±15	382±22	15±3	0.152	0.9704	5
VM	0	-7.19	267.33	-276	20	234±14	246±14	1±1	0.143	0.9609	5
VM	0	-7.16	311.49	-717	8	420±25	330±19	8±1	0.156	0.9703	8
VM	0	-7.10	274.20	94	18	258±15	345±20	15±3	0.143	0.9706	5
VM	0	-7.03	311.09	49	6	391±23	412±24	8±1	0.182	0.9607	8
VM	0	-6.97	275.08	-1803	14	201±12	344±20	11±2	0.166	0.9607	5
VM	0	-6.85	298.00	-1147	4	266±15	284±17	8±1	0.175	0.9705	6
VM	0	-6.84	298.07	-1297	24	156±9	321±19	8±1	0.18	0.980	6
VM	0	-6.83	283.80	3728	32	180±10	408±24	11±2	0.133	0.9701	7
VM	0	-6.55	284.11	705	14	357±21	390±23	13±2	0.149	0.9702	7
VM	0	-6.52	286.34	977	20	217±13	240±14	23±4	0.192	0.9604	8
VM	0	-6.51	284.02	1068	11	291±17	372±22	13±2	0.149	0.9704	7
VM	0	-6.30	283.43	1119	8	394±23	443±26	11±2	0.194	0.9707	7
VM	0	-6.29	290.72	-4380	23	150±9	330±19	9±1	0.245	0.980	7
VM	0	-6.21	290.74	-3235	21	60±3	331±19	9±1	0.254	0.9702	7
VM	0	-6.15	284.26	1804	6	356±21	361±21	13±2	0.163	0.980	7
VM	0	-6.13	283.89	2030	16	323±19	403±24	11±2	0.166	0.9705	7
VM	0	-5.83	283.95	2592	7	354±21	335±20	8±1	0.198	0.9701	7
VM	0	-5.77	283.49	3143	6	381±22	247±14	8±1	0.193	0.9706	7
VM	0	-5.69	271.02	4646	9	186±11	282±16	11±2	0.134	0.970	5
VM	0	-5.66	283.43	2719	5	378±22	269±16	8±1	0.193	0.9807	7
VM	0	-5.59	284.07	2378	17	402±24	385±23	4±1	0.176	0.9702	7
VM	0	-5.51	271.55	3732	35	48±2	252±15	11±2	0.126	0.9802	5
VM	0	-5.50	270.58	-287	29	243±14	380±22	9±1	0.12	0.9705	5
VM	0	-5.36	283.45	2631	7	413±24	244±14	8±1	0.195	0.9607	7
VM	0	-5.34	284.20	-122	7	288±17	425±25	4±1	0.187	0.9706	7
VM	0	-5.25	280.24	2425	18	42±2	164±9	8±1	0.177	0.958	6
VM	0	-4.98	285.01	-820	15	250±15	317±19	5±1	0.199	0.9609	7
VM	0	-4.96	286.90	1527	15	406±24	362±21	7±1	0.223	0.959	7
VM	0	-4.77	286.76	619	25	278±16	311±18	7±1	0.196	0.970	7

VM	0	-4.75	296.50	2155	32	628±37	500±30	9±1	0.131	0.9707	6
VM	0	-4.68	271.89	-881	10	93±5	221±13	9±1	0.184	0.9608	6
VM	0	-4.55	286.92	-2250	3	447±26	228±13	7±1	0.144	0.9701	7
VM	0	-4.00	297.44	2227	25	142±8	333±19	5±1	0.126	0.9803	6
VM	0	-3.85	298.07	-1813	18	277±16	328±19	3±1	0.126	0.9702	6
VM	0	-3.67	287.22	-3129	19	84±5	159±9	1±1	0.232	0.9606	7
VM	0	-3.60	286.75	-2132	16	329±19	323±19	7±1	0.186	0.9605	7
VM	0	-3.53	298.16	-139	27	207±12	353±21	3±1	0.129	0.9707	6
VM	0	-3.48	298.16	-157	28	201±12	368±22	3±1	0.132	0.9708	7
VM	0	-2.67	298.53	-1152	27	341±20	325±19	13±2	0.189	0.970	7
VM	0	-2.32	298.49	-1625	8	172±10	259±15	13±2	0.214	0.9609	7
VM	0	-1.56	284.79	-2199	22	453±27	365±21	5±1	0.223	0.9704	6
VM	0	-1.38	282.35	275	23	319±19	254±15	4±1	0.136	0.980	6
VM	0	-1.33	283.42	836	25	213±12	357±21	4±1	0.15	0.9706	6
VM	0	-1.31	282.89	1388	24	284±17	252±15	4±1	0.13	0.9706	6
VM	0	-1.26	283.68	1670	33	393±23	363±21	4±1	0.175	0.9607	6
VM	0	-1.25	282.50	486	10	332±19	305±18	4±1	0.158	0.9701	6
VM	0	-1.22	283.07	2226	27	349±20	464±27	4±1	0.141	0.9707	6
VM	0	-1.20	284.12	1665	34	193±11	335±20	5±1	0.191	0.970	6
VM	0	-1.10	283.99	2461	28	533±31	455±27	4±1	0.193	0.9707	6
VM	0	-1.08	284.57	-1724	8	173±10	323±19	5±1	0.176	0.9608	6
VM	0	-1.07	284.07	1551	32	113±6	371±22	5±1	0.194	0.9702	6
VM	0	-1.04	283.86	2341	32	406±24	289±17	4±1	0.202	0.980	6
VM	0	-1.04	284.17	-3	13	348±20	336±20	5±1	0.175	0.9703	6
VM	0	-0.79	282.88	1469	17	297±17	341±20	5±1	0.165	0.9708	6
VM	0	-0.78	283.64	650	19	254±15	356±21	5±1	0.2	0.9703	6
VM	0	-0.75	282.11	-4045	14	354±21	337±20	5±1	0.184	0.9605	6
VM	0	-0.72	283.25	-691	26	258±15	383±22	5±1	0.182	0.9708	6
VM	0	-0.69	282.24	-3495	23	302±18	351±21	5±1	0.197	0.9607	6
VM	0	-0.69	283.05	-774	24	131±7	287±17	5±1	0.18	0.9707	6
SML	0	-72.00	3.81	1347	0	177±10	97±5		0.182	0.959	39
SML	0	-53.14	39.12	592	3	288±17	213±12		0.185	0.9607	4
SML	0	-53.00	234.62	2048	7	223±13	243±14		0.161	0.9607	22
SML	0	-51.79	232.49	1793	4	210±12	250±15		0.145	0.9706	19
SML	0	-50.00	13.77	2050	0	282±16	269±16		0.157	0.9607	2
SML	0	-49.86	3.91	303	12	224±13	260±15		0.15	0.9609	3
SML	0	-49.80	3.82	293	8	316±18	266±15		0.146	0.9701	3
SML	0	-49.80	191.01	528	1	269±16	293±17		0.159	0.9608	2
SML	0	-49.79	355.77	131	17	296±17	253±15		0.159	0.9701	4
SML	0	-49.74	2.69	701	12	264±15	205±12		0.166	0.970	3
SML	0	-49.50	14.33	846	3	275±16	251±15		0.168	0.959	2
SML	0	-49.42	196.15	1088	4	281±16	323±19		0.151	0.970	2
SML	0	-49.35	14.55	1060	15	226±13	256±15		0.139	0.980	2
SML	0	-49.31	4.38	728	12	244±14	269±16		0.153	0.9606	3
SML	0	-49.23	14.36	1079	4	193±11	284±17		0.133	0.9607	2
SML	0	-49.08	268.55	2010	1	192±11	237±14		0.136	0.9706	7
SML	0	-49.00	129.70	1737	1	179±10	158±9		0.181	0.9603	2
SML	0	-48.30	193.77	1039	4	356±21	316±18		0.146	0.9701	2
SML	0	-47.84	335.39	736	4	275±16	186±11		0.176	0.9603	3
SML	0	-47.78	303.80	-791	1	384±23	374±22		0.145	0.9706	8
SML	0	-47.67	182.18	2376	8	230±13	244±14		0.178	0.9601	3
SML	0	-47.66	4.78	510	17	395±23	375±22		0.152	0.9609	3
SML	0	-47.66	5.55	1050	15	226±13	259±15		0.147	0.9609	3
SML	0	-47.65	5.25	48	19	390±23	293±17		0.154	0.9609	3
SML	0	-47.52	151.55	833	0	222±13	198±11		0.157	0.9709	4
SML	0	-47.24	273.78	1843	12	151±9	317±19		0.129	0.980	5
SML	0	-47.10	4.20	464	8	331±19	207±12		0.147	0.9702	3
SML	0	-47.07	190.02	654	0	217±13	293±17		0.131	0.9708	3
SML	0	-47.07	238.60	1850	18	217±13	233±13		0.149	0.9809	6
SML	0	-46.99	5.93	1099	2	195±11	217±13		0.151	0.9609	3
SML	0	-46.98	4.21	433	17	339±20	222±13		0.151	0.9607	3

SML	0	-46.92	4.89	484	2	234±14	289±17		0.128	0.9606	3
SML	0	-46.92	5.72	210	28	235±14	251±15		0.146	0.9701	3
SML	0	-46.86	4.30	674	6	158±9	236±14		0.154	0.9701	3
SML	0	-46.80	5.70	97	12	216±12	239±14		0.146	0.9609	3
SML	0	-46.66	239.88	1831	14	178±10	200±12		0.143	0.9608	6
SML	0	-46.21	18.69	944	1	250±15	250±15		0.123	0.9707	3
SML	0	-46.20	18.94	734	11	232±13	300±18		0.12	0.9608	3
SML	0	-45.66	247.99	1911	18	359±21	297±17		0.151	0.9806	7
SML	0	-45.46	27.98	1059	3	264±15	292±17		0.153	0.9609	4
SML	0	-45.06	225.25	206	4	142±8	205±12		0.165	0.9701	3
SML	0	-44.12	212.82	756	4	237±14	303±18		0.143	0.9705	3
SML	0	-43.90	222.64	2090	9	243±14	189±11		0.167	0.9706	3
SML	0	-43.86	35.10	-545	6	248±14	242±14		0.151	0.9708	4
SML	0	-43.82	13.11	874	9	153±9	236±14		0.163	0.9605	4
SML	0	-43.58	258.56	2262	3	199±11	250±15		0.146	0.9704	4
SML	0	-43.53	159.51	1207	0	208±12	276±16		0.177	0.9701	4
SML	0	-43.50	35.00	-582	5	242±14	304±18		0.154	0.9801	4
SML	0	-43.46	239.49	2255	0	203±12	163±9		0.174	0.9609	4
SML	0	-43.40	34.91	-858	4	165±9	264±15		0.154	0.980	4
SML	0	-43.20	190.03	1367	12	307±18	243±14		0.169	0.944	5
SML	0	-43.00	173.09	2031	2	170±10	214±12		0.183	0.954	5
SML	0	-43.00	145.30	1493	7	238±14	198±11		0.18	0.9609	3
SML	0	-42.82	198.26	1438	6	319±19	256±15		0.164	0.9605	4
SML	0	-42.78	214.99	1993	11	185±11	207±12		0.177	0.946	3
SML	0	-42.69	349.92	1420	1	197±11	225±13	9±1	0.172	0.9608	4
SML	0	-42.31	202.19	280	24	165±9	240±14		0.15	0.9706	4
SML	0	-42.24	237.91	2067	3	175±10	209±12		0.158	0.9707	5
SML	0	-42.00	202.00	16	0	151±9	229±13		0.128	0.980	4
SML	0	-41.25	168.55	1292	0	342±20	293±17		0.166	0.9704	5
SML	0	-41.24	171.26	323	4	219±13	299±17		0.186	0.9604	5
SML	0	-41.16	176.50	949	3	238±14	235±14		0.162	0.970	5
SML	0	-41.15	187.20	334	8	198±11	269±16		0.14	0.9604	5
SML	0	-41.13	53.01	-6943	2	274±16	425±25		0.203	0.9602	5
SML	0	-41.11	53.10	-6830	1	266±15	406±24		0.205	0.9602	5
SML	0	-41.07	189.02	405	17	209±12	248±14		0.139	0.9705	6
SML	0	-41.00	219.73	2234	1	167±10	205±12		0.163	0.9801	4
SML	0	-40.81	160.77	690	2	242±14	241±14		0.16	0.9705	5
SML	0	-40.52	196.58	929	19	196±11	223±13	8±1	0.158	0.9607	5
SML	0	-40.39	319.65	-1738	3	269±16	329±19	1±1	0.164	0.970	6
SML	0	-40.17	196.75	801	3	162±9	326±19	8±1	0.137	0.9607	5
SML	0	-40.05	286.52	3496	1	174±10	205±12		0.136	0.980	6
SML	0	-40.01	218.84	2022	2	205±12	220±13		0.146	0.9603	4
SML	0	-39.86	91.58	-4553	6	90±5	307±18		0.157	0.951	5
SML	0	-39.81	153.61	344	6	205±12	217±13		0.149	0.9607	4
SML	0	-39.64	173.83	1162	2	165±9	211±12	7±1	0.163	0.9606	6
SML	0	-39.49	234.30	2448	6	143±8	184±11	7±1	0.164	0.9703	8
SML	0	-39.47	205.13	2000	2	162±9	181±10		0.149	0.9607	6
SML	0	-39.44	5.09	954	6	162±9	273±16	4±1	0.15	0.9705	5
SML	0	-39.40	202.70	-446	20	155±9	249±14		0.127	0.9703	5
SML	0	-39.38	154.35	660	6	275±16	307±18		0.134	0.9702	4
SML	0	-39.35	217.78	1141	2	101±6	250±15		0.135	0.9708	4
SML	0	-39.34	181.75	11	10	222±13	236±14	11±2	0.178	0.9602	4
SML	0	-39.12	196.06	2192	8	237±14	208±12	8±1	0.16	0.9703	5
SML	0	-39.00	217.28	1046	7	227±13	267±16		0.118	0.970	4
SML	0	-38.97	228.17	717	2	308±18	210±12	5±1	0.151	0.9705	5
SML	0	-38.95	353.46	1003	0	187±11	214±12	7±1	0.157	0.9706	5
SML	0	-38.94	196.31	1441	1	170±10	221±13	7±1	0.155	0.9701	5
SML	0	-38.92	160.24	263	13	204±12	247±14		0.148	0.9701	5
SML	0	-38.86	195.93	1069	16	131±7	243±14	7±1	0.139	0.9708	5
SML	0	-38.71	190.04	237	0	248±14	300±18		0.136	0.9701	6
SML	0	-38.65	177.14	536	4	154±9	190±11	1±1	0.154	0.9609	5

SML	0	-38.62	163.98	950	5	229±13	272±16	14±2	0.155	0.9608	5
SML	0	-38.59	159.33	450	3	247±14	248±14		0.142	0.9608	5
SML	0	-38.52	194.49	804	0	190±11	317±19	6±1	0.123	0.9708	5
SML	0	-38.48	190.28	178	0	203±12	266±15		0.144	0.9702	5
SML	0	-38.36	157.82	910	4	366±21	421±25		0.141	0.9802	5
SML	0	-38.32	188.31	345	2	253±15	271±16	5±1	0.147	0.9702	5
SML	0	-38.29	136.74	1390	13	114±6	207±12		0.21	0.9603	3
SML	0	-38.24	88.30	-5069	6	288±17	240±14		0.166	0.9608	7
SML	0	-38.17	224.09	720	4	141±8	217±13	7±1	0.144	0.9608	4
SML	0	-38.15	190.53	196	1	300±18	279±16		0.142	0.9703	5
SML	0	-38.14	184.76	498	0	286±17	255±15	12±2	0.109	0.9702	5
SML	0	-38.10	171.26	512	14	140±8	267±16	9±1	0.136	0.9802	6
SML	0	-38.00	197.70	2319	3	172±10	208±12	6±1	0.151	0.9708	5
SML	0	-37.81	184.74	500	0	221±13	270±16	14±2	0.105	0.9704	5
SML	0	-37.71	126.05	859	0	169±10	188±11		0.176	0.970	4
SML	0	-37.63	351.82	1459	16	155±9	184±11	5±1	0.163	0.9606	5
SML	0	-37.62	329.21	-769	11	162±9	252±15	4±1	0.133	0.9701	5
SML	0	-37.62	329.36	-254	16	172±10	233±13	4±1	0.14	0.9704	5
SML	0	-37.55	184.44	456	1	104±6	278±16	14±2	0.116	0.9706	5
SML	0	-37.54	189.82	56	1	135±8	215±12	6±1	0.125	0.9608	5
SML	0	-37.28	176.34	348	15	178±10	226±13	1±1	0.146	0.9601	6
SML	0	-37.27	188.33	-147	0	199±11	264±15	8±1	0.139	0.9605	5
SML	0	-37.15	190.65	-131	20	215±12	295±17		0.121	0.970	5
SML	0	-37.13	191.01	52	6	187±11	243±14		0.131	0.980	5
SML	0	-37.10	192.00	-231	8	175±10	205±12	4±1	0.133	0.9702	5
SML	0	-37.09	189.44	-165	1	192±11	231±13	6±1	0.127	0.9702	5
SML	0	-37.08	210.71	1174	3	168±10	221±13		0.122	0.9702	6
SML	0	-37.04	343.40	1145	0	156±9	197±11	8±1	0.162	0.970	4
SML	0	-37.00	188.29	-314	1	267±16	264±15	9±1	0.144	0.9608	5
SML	0	-37.00	130.60	1089	0	172±10	237±14	1±1	0.176	0.9705	4
SML	0	-36.95	185.74	849	10	60±3	220±13	12±2	0.139	0.970	5
SML	0	-36.78	149.23	1231	10	201±12	228±13		0.154	0.9607	3
SML	0	-36.77	222.88	1440	3	233±13	244±14	7±1	0.126	0.9708	5
SML	0	-36.76	192.54	797	0	148±8	198±11	5±1	0.131	0.9605	5
SML	0	-36.62	193.27	931	0	232±13	270±16	5±1	0.13	0.9706	5
SML	0	-36.59	190.61	146	4	199±11	229±13		0.122	0.970	5
SML	0	-36.52	178.71	180	7	199±11	242±14	16±3	0.125	0.9702	6
SML	0	-36.43	178.79	-89	6	156±9	231±13	16±3	0.122	0.9703	6
SML	0	-36.01	194.42	1456	1	151±9	247±14	5±1	0.132	0.9708	5
SML	0	-36.00	330.84	377	0	146±8	181±10	6±1	0.146	0.9604	5
SML	0	-36.00	129.40	972	0	221±13	262±15		0.157	0.9607	4
SML	0	-35.85	129.51	1374	14	268±16	258±15	1±1	0.158	0.970	4
SML	0	-35.82	129.34	1405	14	253±15	246±14	1±1	0.157	0.9704	4
SML	0	-35.73	172.49	87	1	197±11	249±14	13±2	0.123	0.9702	7
SML	0	-35.66	169.64	779	17	257±15	275±16	8±1	0.126	0.9707	7
SML	0	-35.54	323.54	-1545	10	133±7	230±13	6±1	0.133	0.980	4
SML	0	-35.50	139.00	583	16	138±8	319±19		0.165	0.9609	5
SML	0	-35.45	201.72	2936	1	127±7	162±9		0.15	0.9702	6
SML	0	-35.28	324.77	264	11	137±8	203±12	5±1	0.139	0.9703	4
SML	0	-35.28	120.19	541	4	201±12	241±14		0.16	0.9609	3
SML	0	-35.25	323.52	-1246	6	115±6	234±14	6±1	0.13	0.9705	4
SML	0	-35.04	173.91	-131	1	210±12	227±13	14±2	0.123	0.9702	7
SML	0	-35.01	144.24	971	14	202±12	325±19		0.146	0.9802	4
SML	0	-34.51	174.04	-3	1	228±13	247±14	6±1	0.131	0.9609	7
SML	0	-34.39	201.78	2761	0	134±8	173±10		0.137	0.9605	6
SML	0	-34.07	134.57	2143	18	185±11	234±14	12±2	0.131	0.9609	3
SML	0	-33.83	235.72	2903	1	152±9	190±11	9±1	0.221	0.9605	7
SML	0	-33.79	80.73	-5530	1	280±16	346±20		0.133	0.9608	5
SML	0	-33.66	134.76	2240	2	193±11	265±15	14±2	0.134	0.9707	3
SML	0	-33.59	94.09	-2368	8	135±8	251±15		0.159	0.9609	5
SML	0	-33.47	94.31	-2089	8	193±11	236±14		0.154	0.956	5

SML	0	-33.31	322.96	1236	2	271±16	239±14	3±1	0.137	0.9801	3
SML	0	-32.87	223.12	1708	12	243±14	285±17	5±1	0.186	0.9704	5
SML	0	-32.80	93.90	-3197	23	202±12	213±12		0.159	0.9701	4
SML	0	-32.72	120.13	999	16	195±11	259±15	7±1	0.129	0.9609	3
SML	0	-32.26	118.56	1096	10	132±7	243±14		0.149	0.9703	3
SML	0	-32.13	116.23	1158	2	107±6	228±13		0.153	0.9703	3
SML	0	-32.00	41.20	180	1	152±9	239±14		0.18	0.9802	6
SML	0	-31.71	143.08	1022	21	295±17	323±19	14±2	0.132	0.9706	4
SML	0	-31.60	137.10	1752	11	268±16	347±20	9±1	0.13	0.9706	2
SML	0	-31.10	95.40	-2599	7	192±11	249±14		0.137	0.9602	4
SML	0	-31.05	49.26	-1650	9	113±6	235±14		0.161	0.9708	5
SML	0	-30.44	313.30	-1092	1	184±11	283±16	1±1	0.114	0.9808	5
EQ	0	-25.96	326.04	-1533	16	174±10	236±14	11±2	0.126	0.9605	5
EQ	0	-19.75	356.66	-362	4	179±10	213±12	11±2	0.153	0.9703	10
EQ	0	-19.31	348.77	-770	5	257±15	274±16	1±1	0.14	0.9703	10
EQ	0	-18.82	113.51	1203	9	179±10	228±13	6±1	0.136	0.9701	3
EQ	0	-18.20	41.50	1413	6	202±12	228±13	8±1	0.143	0.9705	7
EQ	0	-16.35	102.99	1532	15	203±12	234±14	19±3	0.12	0.9708	4
EQ	0	-15.77	71.27	194	8	305±18	270±16	1±1	0.123	0.9706	6
EQ	0	-14.79	54.47	896	7	365±21	400±24	15±3	0.126	0.980	4
EQ	0	-14.33	58.93	909	11	225±13	246±14	11±2	0.13	0.9701	3
EQ	0	-13.59	128.82	1064	14	175±10	227±13	4±1	0.119	0.9608	4
EQ	0	-12.40	121.97	2015	1	232±13	280±16	1±1	0.113	0.9703	5
EQ	0	-12.31	20.13	1100	11	111±6	177±10	4±1	0.148	0.9701	12
EQ	0	-11.30	56.63	1951	16	158±9	196±11	8±1	0.133	0.9709	5
EQ	0	-9.89	6.86	-173	0	90±5	191±11	7±1	0.128	0.9704	10
EQ	0	-9.58	16.47	1968	20	91±5	165±9	2±1	0.14	0.980	15
EQ	0	-9.36	107.86	793	10	148±8	154±9	8±1	0.169	0.970	5
EQ	0	-8.66	86.69	1963	27	248±14	281±16	1±1	0.121	0.9801	5
EQ	0	-8.33	21.10	1227	20	95±5	117±7	3±1	0.133	0.9704	8
EQ	0	-7.69	88.37	2104	9	286±17	307±18	3±1	0.134	0.9707	5
EQ	0	-6.12	356.06	-1105	0	157±9	202±12	5±1	0.113	0.9702	13
EQ	0	-5.71	85.91	2761	10	212±12	239±14	7±1	0.135	0.9607	6
EQ	0	-5.26	355.29	-1391	13	142±8	235±14	11±2	0.113	0.9703	14
EQ	0	-5.07	349.79	-1707	0	155±9	236±14	8±1	0.192	0.9603	10
EQ	0	-5.04	137.21	-3448	9	269±16	236±14	21±4	0.214	0.9701	7
EQ	0	-4.77	137.40	-3759	8	183±10	237±14	1±1	0.226	0.9607	7
EQ	0	-4.40	347.75	-1700	2	187±11	258±15	8±1	0.231	0.948	8
EQ	0	-3.04	357.20	-1461	0	86±5	148±8	9±1	0.135	0.9707	19
EQ	0	-1.90	3.20	-1330	7	174±10	186±11	11±2	0.145	0.9701	14
EQ	0	-0.74	355.50	-1306	0	234±14	228±13	6±1	0.153	0.970	11
EQ	0	-0.42	357.21	-1441	1	137±8	178±10	5±1	0.146	0.9701	12
EQ	0	-0.25	355.63	-1417	3	131±7	122±7	6±1	0.139	0.9604	10
EQ	0	-0.06	1.02	-1279	9	112±6	175±10	15±3	0.177	0.9701	16
EQ	0	1.75	339.36	-2638	3	241±14	286±17	14±2	0.154	0.9706	3
EQ	0	2.13	350.85	-2778	5	254±15	258±15	17±3	0.205	0.9702	3
EQ	0	2.15	350.48	-2655	8	259±15	385±23	17±3	0.147	0.9701	3
EQ	0	2.15	350.95	-2618	11	154±9	220±13	17±3	0.226	0.9606	3
EQ	0	2.16	351.06	-2234	13	212±12	217±13	25±5	0.236	0.9604	3
EQ	0	2.17	350.67	-2765	4	238±14	359±21	17±3	0.181	0.9802	3
EQ	0	2.18	352.49	-2426	6	172±10	218±13	15±3	0.222	0.9606	4
EQ	0	2.20	352.30	-2391	1	235±14	218±13	15±3	0.224	0.970	4
EQ	0	2.92	350.49	-2223	4	234±14	327±19	17±3	0.241	0.9601	3
EQ	0	2.95	350.56	-2288	5	225±13	330±19	17±3	0.238	0.9602	3
EQ	0	4.03	354.70	-2534	1	138±8	246±14	14±2	0.234	0.9603	3
EQ	0	4.14	349.27	-2061	14	176±10	241±14	1±1	0.188	0.9609	4
EQ	0	4.50	349.27	-2635	14	202±12	246±14	1±1	0.2	0.9703	4
EQ	0	4.82	350.09	-2608	6	272±16	429±25	3±1	0.221	0.9605	4
EQ	0	4.97	350.01	-1771	5	263±15	430±25	3±1	0.225	0.9603	4
EQ	0	4.99	350.51	-3105	1	203±12	167±10	3±1	0.226	0.948	4
EQ	0	5.02	350.03	-1841	2	255±15	381±22	9±1	0.214	0.9604	4

EQ	0	5.30	349.74	-2756	9	203±12	402±24	11±2	0.228	0.970	4
EQ	0	6.93	351.27	-2687	9	183±10	256±15	8±1	0.231	0.9606	4
EQ	0	7.50	326.90	-4902	10	416±24	446±26	6±1	0.164	0.959	2
EQ	0	7.73	353.22	-2857	8	122±7	171±10	3±1	0.224	0.9605	3
EQ	0	7.79	352.85	-2577	1	186±11	385±23	7±1	0.227	0.9605	3
EQ	0	7.95	352.68	-2644	2	231±13	425±25	7±1	0.225	0.9609	3
EQ	0	7.97	352.85	-3035	4	266±15	331±19	7±1	0.228	0.970	3
EQ	0	10.00	157.70	-2418	1	262±15	309±18	12±2	0.246	0.958	5
EQ	0	12.87	159.81	-2242	2	257±15	304±18	8±1	0.203	0.9701	5
EQ	0	15.25	171.31	-2771	11	118±7	174±10	3±1	0.263	0.932	7
EQ	0	15.88	161.68	-2256	9	269±16	244±14	11±2	0.235	0.95	6
EQ	0	18.99	77.60	-2012	3	442±26	368±22	14±2	0.17	0.9606	4
EQ	0	20.56	332.39	-3185	0	312±18	341±20	13±2	0.187	0.957	5
EQ	0	22.42	74.37	-824	2	330±19	409±24	8±1	0.154	0.9705	4
EQ	0	-28.00	56.82	-1400	8	272±16	272±16	9±1	0.17	0.9701	6
EQ	0	-18.20	41.50	1413	6	202±12	228±13	8±1	0.143	0.9705	7
EQ	0	-18.00	41.50	2154	2	189±11	228±13	8±1	0.142	0.9702	7
EQ	0	-17.00	331.80	-1990	1	372±22	317±19	8±1	0.133	0.959	8
EQ	0	-11.00	24.60	2003	0	25±1	134±8	5±1	0.128	0.9703	9
EQ	0	-10.80	32.00	2116	1	162±9	178±10	3±1	0.115	0.9807	8
EQ	0	-10.50	24.60	1764	0	112±6	153±9	4±1	0.124	0.9707	8
EQ	0	-3.60	333.75	-3033	9	195±11	237±14	13±2	0.133	0.960	10
EQ	0	3.30	339.00	-2745	17	236±14	409±24	13±2	0.148	0.9608	2
EQ	0	3.88	152.04	-2673	1	39±2	78±4	6±1	0.284	0.951	5
EQ	0	4.39	356.58	-1192	4	236±14	334±20	14±2	0.171	0.9607	2
EQ	0	10.00	157.80	-2741	21	269±16	313±18	12±2	0.246	0.951	5
EQ	0	12.20	291.10	137	0	120±7	120±7	6±1	0.238	0.934	4
EQ	0	18.50	65.00	-316	2	237±14	277±16	15±3	0.118	0.9707	4
CAP	0	26.88	319.96	-3642	3	301±18	320±19	16±3	0.139	0.9707	10
CAP	0	27.06	318.43	-3791	11	267±16	330±19	24±4	0.127	0.9701	9
CAP	0	28.56	318.76	-3908	2	288±17	330±19	9±1	0.135	0.9704	8
CAP	0	28.66	318.10	-3956	0	278±16	281±16	9±1	0.134	0.991	8
CAP	0	33.58	329.68	-4116	3	259±15	262±15	15±3	0.14	0.956	6
CAP	0	33.69	326.63	-4134	1	239±14	273±16	29±5	0.14	0.949	6
CAP	0	34.12	317.04	-3699	4	245±14	312±18	9±1	0.128	0.9703	6
CAP	0	35.25	325.85	-3965	6	210±12	255±15	14±2	0.144	0.9604	6
CAP	0	35.40	330.43	-4208	3	185±11	296±17	2±1	0.13	0.9804	6
CAP	0	35.93	326.80	-4143	1	225±13	233±13	11±2	0.135	0.9706	6
CAP	0	36.51	325.21	-4128	1	212±12	261±15	11±2	0.143	0.9801	6
CAP	0	38.49	322.60	-3983	0	257±15	295±17	16±3	0.137	0.9606	6
CAP	0	39.16	317.99	-3772	1	252±15	316±18	15±3	0.15	0.9608	7
CAP	0	40.11	337.03	-4450	15	250±15	243±14	13±2	0.129	0.955	7

Bibliography

Abramov, O. and Kring, D. A. (2005). Impact-induced hydrothermal activity on early Mars. *Journal of Geophysical Research (Planets)*, 110:E12S09.

Altheide, T., Chevrier, V., Nicholoson, C., and Densonc, J. (2009). Experimental investigation of the stability and evaporation of sulfate and chloride brines on Mars. *Earth and Planetary Science Letters*, 282:69–78.

Atwood-Stone, C. and McEwen, A. S. (2013). Avalanche slope angles in low-gravity environments from active martian sand dunes. *Geophysical Research Letters*, 40(12):2929–2934.

Boynton, W. V., Feldman, W. C., Squyres, S. W., Prettyman, T. H., Brückner, J., Evans, L. G., Reedy, R. C., Starr, R., Arnold, J. R., Drake, D. M., Englert, P. A. J., Metzger, A. E., Mitrofanov, I., Trombka, J. I., d'Uston, C., Wänke, H., Gasnault, O., Hamara, D. K., Janes, D. M., Marcialis, R. L., Maurice, S., Mikheeva, I., Taylor, G. J., Tokar, R., and Shinohara, C. (2002). Distribution of Hydrogen in the Near Surface of Mars: Evidence for Subsurface Ice Deposits. *Science*, 297:81–85.

Boynton, W. V., Taylor, G. J., Evans, L. G., Reedy, R. C., Starr, R., Janes, D. M., Kerry, K. E., Drake, D. M., Kim, K. J., Williams, R. M. S., Crombie, M. K., Dohm, J. M., Baker, V., Metzger, A. E., Karunatillake, S., Keller, J. M., Newsom, H. E., Arnold, J. R., Brückner, J., Englert, P. A. J., Gasnault, O., Sprague, A. L., Mitrofanov, I., Squyres, S. W., Trombka, J. I., d'Uston, L., Wänke, H., and Hamara, D. K. (2007). Concentration of H, Si, Cl, K, Fe, and Th in the low- and mid-latitude regions of Mars. *Journal of Geophysical Research (Planets)*, 112:E12S99.

Burrough, P. A. and McDonnell, R. (1999). *Principles of Geographical Information Systems*. Oxford University Press, New York.

Carr, M. H. (2007). *The Surface of Mars*. Cambridge University Press.

Chevrier, V. and Rivera-Valentin, E. (2012). Formation of recurring slope lineae by liquid brines on present-day Mars. *Geophysical Research Letters*, 39:L21202.

Chojnacki, M., McEwen, A., Dundas, C., Ojha, L., Urso, A., and Sutton, S. (2016). Geologic context of recurring slope lineae in melas and coprates chasmata, mars. *Journal of Geophysical Research: Planets*, 121(7):1204–1231.

Christensen, P. (1986). The spatial distribution of rocks on Mars. *icarus*, 68:217–238.

Christensen, P. R., Bandfield, J. L., Bell III, J. F., Gorelick, N., Hamilton, V. E., Ivanov, A., Jakosky, B. M., Kieffer, H. H., Lane, M. D., Malin, M. C., McConnochie, T., McEwen, A. S., McSween, H. Y., Mehall, G. L., Moersch, J. E., Nealson, K. H., Rice, J. W., Richardson, M. I., Ruff, S. W., Smith, M. D., Titus, T. N., and Wyatt, M. B. (2003). Morphology and Composition of the Surface of Mars: Mars Odyssey THEMIS Results. *Science*, 300(5628):2056–2061.

Christensen, P. R., Bandfield, J. L., Hamilton, V. E., Ruff, S. W., Kieffer, H. H., Titus, T. N., Malin, M. C., Morris, R. V., Lane, M. D., Clark, R. L., Jakosky, B. M., Mellon, M. T., Pearl, J. C., Conrath, B. J., Smith, M. D., Clancy, R. T., Kuzmin, R. O., Roush, T., Mehall, G. L., Gorelick, N., Bender, K., Murray, K., Dason, S., Greene, E., Silverman, S., and Greenfield, M. (2001). Mars Global Surveyor Thermal Emission Spectrometer

experiment: Investigation description and surface science results. *Journal of Geophysical Research: Planets*, 106(E10):23823–23871.

Christensen, P. R., Jakosky, B. M., Kieffer, H. H., Malin, M. C., McSween, H. Y., Nealson, K., Mehall, G. L., Silverman, S. H., Ferry, S., Caplinger, M., and Ravine, M. (2004). The Thermal Emission Imaging System (THEMIS) for the Mars 2001 Odyssey Mission, journal=Space Science Reviews. 110(1):85–130.

Clancy, R. T., Sandor, B. J., Wolff, M. J., Christensen, P. R., Smith, M. D., Pearl, J. C., Conrath, B. J., and Wilson, R. J. (2000). An intercomparison of ground-based millimeter, MGS TES, and Viking atmospheric temperature measurements: Seasonal and interannual variability of temperatures and dust loading in the global Mars atmosphere. *Journal of Geophysical Research*, 105:9553–9572.

Dundas, C. M., Bramson, A. M., Ojha, L., Wray, J. J., Mellon, M. T., Byrne, S., McEwen, A. S., Putzig, N. E., Viola, D., Sutton, S., Clark, E., and Holt, J. W. (2018). Exposed subsurface ice sheets in the Martian mid-latitudes. *Science*, 359:199–201.

Dundas, C. M., McEwen, A. S., Chojnacki, M., Milazzo, M. P., Byrne, S., McElwaine, J. N., and Urso, A. (2017). Granular flows at recurring slope lineae on Mars indicate a limited role for liquid water. *Nature Geoscience*, 10:903–907.

Edwards, C. S. and Piqueux, S. (2016). The water content of recurring slope lineae on Mars. *Geophysical Research Letters*, 43(17):8912–8919.

Ehlmann, B. L., Mustard, J. F., and Murchie, S. L. (2010). Geologic setting of serpentine deposits on Mars. *Geophysical Research Letters*, 37:L06201.

Feldman, W. C., Prettyman, T. H., Maurice, S., Plaut, J. J., Bish, D. L., Vaniman, D. T., Mellon, M. T., Metzger, A. E., Squyres, S. W., Karunatillake, S., Boynton, W. V., Elphic, R. C., Funsten, H. O., Lawrence, D. J., and Tokar, R. L. (2004). Global distribution of near-surface hydrogen on Mars. *Journal of Geophysical Research (Planets)*, 109:E09006.

Grimm, R. E., Harrison, K. P., and Stillman, D. E. (2014). Water budgets of martian recurring slope lineae. *Icarus*, 233:316–327.

Hansen, C. J., Bourke, M., Bridges, N. T., Byrne, S., Colon, C., Diniega, S., Dundas, C., Herkenhoff, K., McEwen, A., Mellon, M., Portyankina, G., and Thomas, N. (2011). Seasonal Erosion and Restoration of Mars Northern Polar Dunes. *Science*, 331:575.

Kieffer, H., Neugebauer, G., Munch, G., Chase, Jr., S., and Miner, E. (1972). Infrared Thermal Mapping Experiment: The Viking Mars Orbiter. *Icarus*, 16:47–56.

Kieffer, H. H., Martin, T. Z., Peterfreund, A. R., Jakosky, B. M., Miner, E. D., and Palluconi, F. D. (1977). Thermal and albedo mapping of Mars during the Viking primary mission. *Jounral of Geophysical Research*, 82:4249–4291.

Kirk, R. L., Howington-Kraus, E., Rosiek, M. R., Anderson, J. A., Archinal, B. A., Becker, K. J., Cook, D. A., Galuszka, D. M., Geissler, P. E., Hare, T. M., Holmberg, I. M., Keszthelyi, L. P., Redding, B. L., Delamere, W. A., Gallagher, D., Chapel, J. D., Eliason, E. M., King, R., and McEwen, A. S. (2008). Ultrahigh resolution topographic mapping of mars with mro hirise stereo images: Meter-scale slopes of candidate phoenix landing sites. *Journal of Geophysical Research: Planets*, 113(E3).

Knauth, L. P. and Burt, D. M. (2002). Eutectic Brines on Mars: Origin and Possible Relation to Young Seepage Features. *Icarus*, 158.

Knudsen, M. (1910). Thermischer Molekulardruck der Gase in Rähren. *Annalen der Physik*, 338(16):1435–1448.

Malin, M. C. and Edgett, K. S. (2000). Evidence for recent groundwater seepage and surface runoff on mars. *Science*, 288(5475):2330–2335.

Massé, M., Beck, P., Schmitt, B., Pommerol, A., McEwen, A., Chevrier, V., Brissaud, O., and Séjourné, A. (2014). Spectroscopy and detectability of liquid brines on Mars. *Planetary and Space Science*, 92.

Massé, M., Conway, S. J., Gargani, J., Patel, M. R., Pasquon, K., McEwen, A., Carpy, S., Chevrier, V., Balme, M. R., Ojha, L., Vincendon, M., Poulet, F., Costard, F., and Jouannic, G. (2016). Transport processes induced by metastable boiling water under Martian surface conditions. *Nature Geoscience*, 9:406–428.

McEwen, A., Chojnacki, M., Dundas, C., Ojha, L., Massé, M., Schaefer, E., and Leung, C. (2015). Recurring Slope Lineae on Mars: Equatorial Origin? *EPSC Abstracts Vol. 10, EPSC2015-786-1, 2015 European Planetary Science Congress 2015*.

McEwen, A., Dundas, C., Mattson, S., Toigo, A., Ojha, L., Murchie, S., Thomas, N., Wray, J., Byrne, S., and Chojnacki, M. (2013a). Recurring Slope Lineae (RSL) in Equatorial Mars. *EPSC Abstracts Vol. 8, EPSC2013-846, 2013 European Planetary Science Congress 201*.

McEwen, A. S., Eliason, E. M., Bergstrom, J. W., Bridges, N. T., Hansen, C. J., Delamere, W. A., Grant, J. A., Gulick, V. C., Herkenhoff, K. E., Keszthelyi, L., Kirk, R. L., Mellon, M. T., Squyres, S. W., Thomas, N., and Weitz, C. M. (2007). Mars Reconnaissance Orbiter's High Resolution Imaging Science Experiment (HiRISE). *Journal of Geophysical Research*, 112:E05S02–.

McEwen, A. S., Ojha, L., Dundas, C. M., Mattson, S. S., Byrne, S., Wray, J. J., Cull, S. C., Murchie, S. L., Thomas, N., and Gulick, V. C. (2011). Seasonal flows on warm Martian slopes. *Science*, 333(6043):740–743.

McEwen, Alfred S.and Dundas, C. M., Mattson, S. S., Toigo, A. D., Ojha, L., Wray, James J.and Chojnacki, M., Byrne, S., and Murchie, Scott L.and Thomas, N. (2013b). Recurring slope lineae in equatorial regions of Mars. *Nature Geoscience*, 7.

Mellon, M. T., Jakosky, B. M., and Postawko, S. E. (1997). The persistence of equatorial ground ice on Mars. *Journal of Geophysical Research*, 102:19357–19370.

Murchie, S., Arvidson, R., Bedini, P., Beisser, K., Bibring, J.-P., Bishop, J., Boldt, J., Cavender, P., Choo, T., Clancy, R. T., Darlington, E. H., Des Marais, D., Espiritu, R., Fort, D., Green, R., Guinness, E., Hayes, J., Hash, C., Heffernan, K., Hemmler, J., Heyler, G., Humm, D., Hutcheson, J., Izenberg, N., Lee, R., Lees, J., Lohr, D., Malaret, E., Martin, T., McGovern, J. A., McGuire, P., Morris, R., Mustard, J., Pelkey, S., Rhodes, E., Robinson, M., Roush, T., Schaefer, E., Seagrave, G., Seelos, F., Silverglate, P., Slavney, S., Smith, M., Shyong, W.-J., Strohbehn, K., Taylor, H., Thompson, P., Tossman, B., Wirzburger, M., and Wolff, M. (2007). Compact Reconnaissance Imaging Spectrometer for Mars (CRISM) on Mars Reconnaissance Orbiter (MRO). *Journal of Geophysical Research: Planets*, 112(E5).

Neumann, G. A., Zuber, M. T., Wieczorek, M. A., McGovern, P. J., Lemoine, F. G., and Smith, D. E. (2004). Crustal structure of Mars from gravity and topography. *Journal of Geophysical Research (Planets)*, 109:E08002.

Ojha, L., McEwen, A., Dundas, C., Byrne, S., Mattson, S., Wray, J., Massé, M., and Schaefer, E. (2014). HiRISE observations of Recurring Slope Lineae (RSL) during southern summer on Mars. *Icarus*, 231.

Ojha, L., Wilhelm, M. B., Murchie, S. L., McEwen, A. S., Wray, James J.and Hanley, J., Massé, M., and Chojnacki, M. (2015). Spectral evidence for hydrated salts in recurring slope lineae on Mars. *Nature Geoscience*, 8:829–832.

Orosei, R., Lauro, S. E., Pettinelli, E., Cicchetti, A., Coradini, M., Cosciotti, B., Di Paolo, F., Flamini, E., Mattei, E., Pajola, M., Soldovieri, F., Cartacci, M., Cassenti, F., Frigeri, A., Giuppi, S., Martufi, R., Masdea, A., Mitri, G., Nenna, C., Noschese, R., Restano, M., and Seu, R. (2018). Radar evidence of subglacial liquid water on Mars. *Science*, 361:490–493.

Pollack, J. B., Kasting, J. F., Richardson, S. M., and Poliakoff, K. (1987). The case for a wet, warm climate on early Mars. *Icarus*, 71:203–224.

Putzig, N. and Mellon, M. T. (2007). Apparent thermal inertia and the surface heterogeneity of Mars. *Icarus*, 191:68–94.

Renno, N., Bos, B., Catling, D., Clark, B., Drube, L., Fisher, D., Goetz, W., Hviid, S. F., Keller, H. U., Kok, J. F., Kounaves, S. P., Leer, K., Lemmon, M., Madsen, M. B., Markiewicz, W. J., Marshall, J., McKay, C., Mehta, M., Smith, M., Zorzano, M. P., Smith, P. H., Stoker, C., and Young, S. M. M. (2009). Possible physical and thermodynamical evidence for liquid water at the Phoenix landing site. *Journal of Geophysical Research (Planets)*, 114:E00E03.

Rivoldini, A., Van Hoolst, T., Verhoeven, O., Mocquet, A., and Dehant, V. (2011). Geodesy constraints on the interior structure and composition of Mars. *Icarus*, 213:451–472.

Ruff, S. and Christensen, P. (2002). Bright and dark regions on Mars: Particle size and mineralogical characteristics based on Thermal Emission Spectrometer data. *Journal of Geophysical Research (Planets)*, 107:5127.

Schmidt, F., Andrieu, F., Costard, F., Kocifaj, M., and Meresescu, A. G. (2017). Formation of recurring slope lineae on Mars by rarefied gas-triggered granular flows. *Nature Geoscience*, 10:270–273.

Smith, D., Zuber, M., Frey, H., Garvin, J., Head, J., Muhleman, D., Pettengill, G., Phillips, R., Solomon, S., Zwally, H., Banerdt, W., Duxbury, T., Golombek, M., Lemoine, F., Neumann, G., Rowlands, D., Aharonson, O., Ford, P., Ivanov, A., Johnson, C., McGovern, P., Abshire, J., Afzal, R., and Sun, X. (2001). Mars Orbiter Laser Altimeter: Experiment summary after the first year of global mapping of Mars. *Journal of Geophysical Research*, 106:23689–23722.

Stillman, D. E. and Grimm, R. E. (2018). Two pulses of seasonal activity in martian southern mid-latitude recurring slope lineae (RSL). *Icarus*, 302:126–133.

Stillman, D. E., Michaels, T. I., and Grimm, R. E. (2017). Characteristics of the numerous and widespread recurring slope lineae (RSL) in Valles Marineris, Mars. *Icarus*, 285:195–210.

Stillman, D. E., Michaels, T. I., Grimm, R. E., and Hanley, J. (2016). Observations and modeling of northern mid-latitude recurring slope lineae (RSL) suggest recharge by a present-day martian briny aquifer. *Icarus*, 265.

Stillman, D. E., Michaels, T. I., Grimm, R. E., and Harrison, K. P. (2014). New observations of martian southern mid-latitude recurring slope lineae (RSL) imply formation by freshwater subsurface flows. *Icarus*, 233:328–341.

Thomas, N., Cremonese, G., Ziethe, R., Gerber, M., Brändli, M., Bruno, G., Erismann, M., Gambicorti, L., Gerber, T., Ghose, K., Gruber, M., Gubler, P., Mischler, H., Jost, J., Piazza, D., Pommerol, A., Rieder, M., Roloff, V., Servonet, A., Trottmann, W., Uthaicharoenpong, T., Zimmermann, C., Vernani, D., Johnson, M., Pelò, E., Weigel, T., Viertl, J., De Roux, N., Lochmatter, P., Sutter, G., Casciello, A., Hausner, T., Ficai Veltroni, I., Da Deppo, V., Orleanski, P., Nowosielski, W., Zawistowski, T., Szalai, S., Sodor, B., Tulyakov, S., Troznai, G., Banaskiewicz, M., Bridges, J. C., Byrne, S., Debei, S., El-Maarry, M. R., Hauber, E., Hansen, C. J., Ivanov, A., Keszthelyi, L., Kirk, R., Kuzmin, R., Mangold, N., Marinangeli, L., Markiewicz, W. J., Massironi, M., McEwen, A. S., Okubo, C., Tornabene, L. L., Wajer, P., and Wray, J. J. (2017). The Colour and Stereo Surface Imaging System (CaSSIS) for the ExoMars Trace Gas Orbiter. *Space Science Reviews*, 212:1897–1944.

Tornabene, L. L., Seelos, F. P., Pommerol, A., Thomas, N., Caudill, C. M., Becerra, P., Bridges, J. C., Byrne, S., Cardinale, M., Chojnacki, M., Conway, S. J., Cremonese, G., Dundas, C. M., El-Maarry, M. R., Fernando, J., Hansen, C. J., Hansen, K., Harrison,

T. N., Henson, R., Marinangeli, L., McEwen, A. S., Pajola, M., Sutton, S. S., and Wray, J. J. (2018). Image Simulation and Assessment of the Colour and Spatial Capabilities of the Colour and Stereo Surface Imaging System (CaSSIS) on the ExoMars Trace Gas Orbiter. *Space Science Reviews*, 214:18.

Treiman, A. (2005). The nakhlite meteorites: Augite-rich igneous rocks from Mars. *Chemie der Erde / Geochemistry*, 65:203–270.

Watkins, J., Ojha, L., Chojnacki, M., Reith, R., and Yin, A. (2014). Structurally Controlled Subsurface Fluid Flow as a Mechanism for the Formation of Recurring Slope Lineae. In *Lunar and Planetary Science Conference*, volume 45 of *Lunar and Planetary Inst. Technical Report*, page 2911.

Wieczorek, M. A. and Zuber, M. T. (2004). Thickness of the Martian crust: Improved constraints from geoid-to-topography ratios. *Journal of Geophysical Research (Planets)*, 109:E01009.

Wilson, J. T., Eke, V. R., Massey, R. J., Elphic, R. C., Feldman, W. C., Maurice, S., and Teodoro, L. F. A. (2018). Equatorial locations of water on Mars: Improved resolution maps based on Mars Odyssey Neutron Spectrometer data. *Icarus*, 299:148–160.

Wurm, G., Teiser, J., and Reiss, D. (2008). Greenhouse and thermophoretic effects in dust layers: The missing link for lifting of dust on Mars. *Geophysical Research Letters*, 35:L10201.